Solid-state interactions of materials: Applications-based solid-state NMR spectroscopy

Megan Matthews

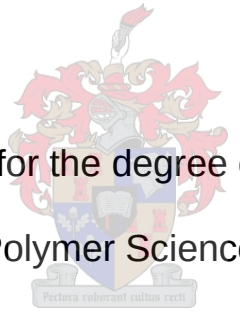

Dissertation presented for the degree of Doctor of Philosophy

(Polymer Science)

Stellenbosch University

Supervisor: Prof. A. J. van Reenen

April 2022

Declaration

By submitting this dissertation, I declare that the entirety of the work contained herein is my own, original work, that I am the owner of the copyright thereof (unless to the extent explicitly otherwise stated) and that I have not previously in its entirety or in part submitted it for obtaining any qualification.

Date: April 2022

Abstract

The solid-state interactions of various polymeric materials were investigated in this study to determine how these interactions affect the macroscopic properties of the solid.

The work presented in this dissertation was classified into three commercial problems which were solved using solid-state NMR and a variety of other solid-state techniques. First, vis-breaking was performed *in-situ* on heterophasic ethylene-propylene copolymers (HEPCs) to determine the effect on HEPCs of increasing ethylene contents. Solution ^{13}C NMR and solid-state NMR was used to determine the effect of the peroxide on the structure and morphology of the HEPCs. The extent of vis-breaking was found to be dependent on the homogeneity of chain sequences. In all cases vis-breaking increased the mobility of the crystalline domains forming a disordered crystal phase within the polypropylene α-structure.

Second, the possibility of using impact copolymers as the polymer component of hot-melt adhesives (HMAs) was investigated. A high ethylene-content impact copolymer was blended with three types of waxes and characterised by various solid-state techniques. It was found that the ethylene-rich regions of the impact copolymer displayed strong interactions with the waxes and the extent of the interaction was dependent on the composition of the wax. The bond strength results of the HMAs were found to be comparable to that of an industry standard HMA and the failure mechanism was dependent on the wax type and concentration. Finally, the mechanism of oil entrapment by Fischer-Tropsch (FT) waxes was explored to determine whether wideline NMR is an appropriate method for determination of oil content of waxes. Benchtop solid-state NMR instruments apply wideline methods to determine oil contents commercially in cases where vast differences in mobility exist between phases. Blends of a standard oil and waxes of various melting temperatures were prepared and characterised by various techniques. The higher melting FT waxes were found to trap oil in small pools and limit the mobility of the oil making it difficult to detect by solid-state NMR. Linear correlations could only be obtained by using variable temperature methods and by simplifying the oil composition, however, the accuracy of the correlations was not high.

The focus of this study was, therefore, not on the properties of a specific material but on the development of solid-state NMR methods with unique applications to solve industrial problems.

Opsomming

In die huidige studie is die soliedefase interaksies van verskillende polimeer materiale ondersoek om te bepaal watter uitwerking hierdie interaksies op die makroskopiese eienskappe van die vastestof het.

Die resultate wat in hierdie tesis aangebied word, is volgens drie kommersiële probleme geklassifiseer wat deur die gebruik van soliedefase kernmagnetieseresonansie (KMR) en ’n verskeidenheid ander soliedefase tegnieke opgelos is. Eerstens, is vis-breking *in-situ* op heterofase polipropileen-etileen-kopropileen kopolimere (HEPCs) uitgevoer om die effek van verhoodge etileeninhoud op HEPCs te bepaal. Vloeistof ^{13}C NMR en soliedefase KMR is gebruik om die effek van die peroksied op die struktuur en morfologie van die HEPCs te bepaal. Daar is bevind dat die omvang van vis-breking van die homogeniteit van kettingvolgordes afhanklik is. In al die bestudeerde gevalle is die mobiliteit van die kristalvormige domeine deur vis-breking verhoog wat tot die vorming van ’n versteurde kristalfase binne die polipropileen α-struktuur lei.

Tweedens, is die moontlikheid om van impak kopolimere as die polimeer komponent van hoë -smeltpunt kleefmiddels (HMAs) gebruik te maak, ondersoek. ’n Hoë etileeninhoud impak kopolimeer is met drie wassoorte gemeng en deur verskillende soliedefase tegnieke gekarakteriseer. Die etileenryke gebiede van die impak kopolimeer is bevind om sterk interaksies met die wasse te vertoon. Die omvang van hierdie interaksie is afhanklik van die samestelling van die was. Die bindingssterkte resultate van die HMAs is vergelykbaar gevind met dié van ’n industrie standaard HMA en die mislukkingsmeganisme is van die wassoort en -konsentrasie afhanklik. Ten laaste, is die meganisme van olie-vaslegging in Fischer-Tropsch (FT)-wasse ondersoek om te bepaal of breëlyn KMR ’n gepaste metode is om die olie-inhoud van wasse te bepaal. ‘Benchtop’-soliedefase KMR-instrumente pas breëlyn-metodes toe om olie-inhoud kommersieel te bepaal, in gevalle waar oneindig groot mobiliteitsverskille tussen fases bestaan. Samestellings van ’n standaard olie en drie wasse, met verskillende smelttemperature, is voorberei en deur middel van verskillende tegnieke gekarakteriseer. Daar is bevind dat die hoër smeltende FT-wasse olie in klein poele vasvang en die mobiliteit van die olie beperk wat dit moeilik maak om deur middel van soliedefase KMR op te spoor. Lineêre korrelasies kon slegs verkry word deur veranderlike temperatuurmetodes te gebruik en deur die olie-samestelling te simplifiseer, maar die bevinding dui aan dat die akkuraatheid van die korrelasies nie hoog is nie.

Die fokus van die huidige studie was dus nie gemik op die eienskappe van ’n spesifieke materiaal nie maar op die ontwikkeling van soliedefase KMR-metodes met unieke toepassings om industriële probleme op te los.

For Roslyn

Acknowledgments

I would like to thank the following people for their contributions towards my PhD journey and the completion of this dissertation:

First, my supervisor Prof van Reenen for all his guidance and patience during this process.

Second, to my mentor Heidi Duveskog for the endless advice on solid-state NMR and on life.

To Dr Divann Robertson for sharing his experience on HMAs and his fume hood. To the Olefins research group, thank you for the support and for being a soundboard when it felt like nothing was making sense.

A heartfelt thanks to Mrs Erinda Cooper, Ms Mienie Jones, Mr Calvin Maart and the other administrative, technical and support staff of the Chemistry and Polymer Science Department without which the engine of our department would not be able to function.

A special thank you to Mrs Lize Engelbrecht, Mrs Elsa Malherbe and Dr Jaco Brand at Central Analytical Facility (CAF) at Stellenbosch University for the use of CLSM and NMR facilities as well as Dr A. Tredoux for the HT-GC analyses. The National Research Foundation of South Africa (NRF) is also acknowledged for funding this project.

Lastly, I would also like to thank my mother, friends and family for their encouragement and prayers and for always checking up on me during the difficult times.

Table of Contents

List of Figures

List of Tables

List of Abbreviations

APP	Atactic polypropylene
CLSM	Confocal Laser Scanning Microscopy
CP	Cross-Polarisation
DSC	Differential Scanning Calorimetry
EVA	Ethylene vinyl-acetate
FT	Fischer-Tropsch
HEPC	Heterophasic ethylene-propylene copolymer
HMA	Hot-melt adhesive
ICP	Impact copolymer
ID	Interrupted Decoupling
MAS	Magic Angle Spinning
MEK	Methyl ether ketone
SS NMR	Solid-state Nuclear Magnetic Resonance
TPPM	Two-Pulse Phase-Modulated
VCT	Variable Contact Time
WAT	Wax appearance temperature
XRD	X-ray diffraction

Chapter 1: Introduction

The solid state of materials is of academic and commercial importance as many substances are interacted with in their solid phase. Studies of matter in the liquid and gaseous phases have yielded essential fundamental information regarding these substances, however, the key aspect which defines solids, the inter- and intramolecular interactions which bind atoms in definite arrangements, is absent in both liquid and gaseous phases. These interactions and their resultant arrangements and structural hierarchies play a vital role in the ultimate physical properties of the solid material.[1]

This is especially true for polymeric materials, where the presence of multiple structural distributions lead to complex levels of organisation. When structural regularity exists and crystallinity is possible, the relative arrangements of the crystalline and amorphous domains depend on both the microstructure and external conditions during the process of solidification.[2] The process of attaining a specific relative arrangement of these domains upon solidification is referred to as morphology development and determines the thermal and mechanical properties of the solid polymer. Therefore, as more intricate polymer systems are developed with targeted properties, the corresponding use of robust analytical techniques is required. X-ray scattering methods have been highly popular for such applications, however, X-ray techniques cannot provide details on non-crystalline materials.[3]

Nuclear Magnetic Resonance (NMR) spectroscopy is a powerful analytical tool in chemistry and materials science. Solution state NMR methods are well-known for structure elucidation and characterisation of motional dynamics of dissolved substances.[4] The ability of solution NMR spectroscopy to yield these results is due to the rapid molecular motions occurring in solution i.e. when individual chains are isolated from one another by solvent molecules. While the importance of solution NMR cannot be disputed, most materials are interacted with in their solid state as mentioned above. Therefore, techniques need to be able to characterise solid state structures in addition to the molecular interactions present which are minimised due to solvation and cannot be detected by solution methods.

The aim of this thesis is to apply a variety of solid-state NMR methods in conjunction with additional techniques to solve problems related to specific applications of different polymeric materials. It is important to note that while solid-state NMR is a powerful technique, it cannot be used in isolation. Other details about the system, such as molecular weight distribution and chemical structure, should be known in order to facilitate accurate interpretation of NMR spectra. A general overview of the solid state of polymers and relevant concepts in solid state NMR is given in chapter two.

Chapter three details the method development and findings of an *in-situ* vis-breaking study of heterophasic ethylene-propylene copolymers (HEPCs). Vis-breaking or rheology control is a process of combining a polymer (conventionally polypropylene) with an organic peroxide to decrease the average molecular weight by chain scission.[5] This is known to enhance the flow properties of the polymer. The mechanism of vis-breaking was investigated and compared to known degradation mechanisms of polypropylene and polyethylene homopolymers. The focus of chapter four is also on HEPCs, but in this case the use of high ethylene-content HEPC as the polymer component in hot-melt adhesives (HMAs). The interaction between the HEPC and the wax component is studied in detail to explain the mechanical properties of the resultant adhesive. In chapter five the mechanism of the binding of oil in different types of waxes is described. Static wideline and relaxation experiments were conducted to compare to industrial quality control methods and investigate the applicability of solid-state NMR methods for quantification of oil in waxes.

These diverse polymer systems showcase the wide range of capabilities of solid-state NMR methods yet only scratch the surface of possible novel applications.

References

[1] R.B. Seymour, C.E.J. Carraher, Structure-Property Relationships in Polymers, Plenum Press, 1985.

[2] E.H. Andrews, Structure-Property Relationships in a Polymer, Int. J. Polym. Mater. Polym. Biomater. 2 (1973) 337–359. https://doi.org/10.1080/00914037308072367.

[3] I. Ando, T. Asakura, Introduction, in: I. Ando, T. Asakura (Eds.), Solid State NMR Polym. Stud. Phys. Theor. Chem., Elsevier Science, 1998: pp. 1–634.

[4] A. Steigel, H.W. Spiess, Dynamic NMR Spectroscopy, in: P. Diehl, E. Fluck, R. Kosfeld (Eds.), NMR Basic Princ. Prog., Springer-Verlag, 1982: pp. 1–219. https://doi.org/10.1007/978-3-642-66961-3.

[5] M. Swart, A.J. Van Reenen, The effect of controlled degradation on the molecular characteristics of heterophasic ethylene-propylene copolymers, J. Appl. Polym. Sci. 132 (2015) 1–10. https://doi.org/10.1002/app.41783.

Chapter 2: Theoretical Background

2.1 The solid state of polymers

The discussion of the nature and properties of the solid state of polymers (alternatively referred to as the bulk or condensed state) is indispensable as most polymers are used in their solid form. Chemical reactions in the gaseous phase and the liquid phase provide fundamental insight into materials, however, the solid-state chemistry defines the majority of society's interactions with matter. For this reason, the discussion of the properties, morphology and applications of polymers in the solid state is a key aspect of academic and industrial research.

The solid state of polymers is essentially defined by two states; the amorphous and semi-crystalline states.[1] Polymers which possess amorphous or semi-crystalline states have significantly different thermal, optical and mechanical properties. The amorphous state is defined by disordered polymer chains. Amorphous polymers display vastly different properties depending on the ambient temperature. Below a specific, structure-dependent temperature amorphous polymers are rigid and brittle while above this temperature the polymer becomes more pliable due to the onset of long-range molecular motion.[2] This temperature is known as the glass transition temperature (T_g) and indicates the glass-to-rubber transition in polymers.[2] The crystalline state is defined by the presence of the first-order thermal transition called melting.[2] Polymers in the solid state cannot fully crystallise due to their long chains and the resultant chain entanglements. Thus polymers which contain crystalline structures are referred to as semi-crystalline. The ability to crystallise is dependent on structural regularity. The organisation of polymer chains in the solid state and the characterisation of the resultant structural hierarchies is discussed in the following sections.

2.1.1 Structure-property relationships

Polymers contain various structural hierarchies at different measurement scales. Molecular structure is the most basic level and while it does not necessarily define the properties of the bulk material, the successive levels of structure are dependent on the molecular characteristics. The molecular structure level consists of three key aspects; the chemical structure of the monomer, the molecular weight of the polymer chain and the chain microstructure.[3]

The dimensions of a polymer molecule are determined by the chain length. Chain conformations also depend on the extent of free rotation about individual bonds. This free rotation results in the constant segmental motion of polymer chains above the glass transition

temperature. Therefore, the shapes or conformations that polymer chains adopt have a temperature dependency. In addition to the above-mentioned factors influencing chain conformations, polymer chains also tend to assume lower energy conformations.[4]

The intrinsic kinetic energy of amorphous polymers implies that the chains are in a constant state of motion. The degree of this motion decreases with temperature until a threshold temperature is reached, called the glass transition temperature. Below this temperature the polymer exhibits brittle, glass-like properties while above the T_g the material is rubber-like with decreasing stiffness and modulus. The T_g is dependent on chain stiffness imparted by the chemical structure and geometry. Strong intermolecular forces also restrict segmental motion and increase the value of the T_g.[4] Where crystallisation is possible, the dominant process between glass transition and crystallisation depends on the polymer's inherent crystallisation ability as well as the relative crystallisation kinetics. This is controlled by both microstructural and thermal factors.

The interplay of the monomer structure, microstructure and molecular weight leads to the molecular interactions which control the glass transition temperature, the crystal structure as well as the maximum degree of crystallinity obtainable. The combination of these three aspects defines the polymer morphology, which ultimately determines the material's solid-state properties. This complex interplay of various factors and structural hierarchy is the reason why mechanical and thermal properties of a material cannot be simply correlated to its molecular structure.

2.1.2 Morphology

The morphology of a polymer describes the nano – and microscale structural order in the solid state. The type of morphologies achievable depend on the constituents of the polymer. A semi-crystalline homopolymer will have different possible morphologies compared to a polymer blend or copolymer. In semi-crystalline polymers crystalline domains take the form of lamellae when chains arrange parallel to one another. Due to the length of the chains a single chain can exist in multiple lamellae or can fold in on itself to propagate a single lamellar structure.[2] The continued growth of these lamellae form ribbon-like structures called spherulites, which have often been observed in polyolefins.[5] When the molecular weight is decreased, however, as is the case when comparing linear polyethylenes to linear waxes, the chain folding does not occur and spherulitic structures are not observed. This also means that the amount of non-crystallisable material is much less for these waxes than polyethylenes since chain folded regions cannot be incorporated within crystalline domains. As a result, linear waxes and linear polyethylenes both have high hardness, but the wax is more brittle than the polymeric material. Blends of polymers also display a range of morphologies depending on the miscibility of the

two components. Most polymer blends are immiscible and yield materials with multiple phases.[5] The morphology of such blends depends on the relative concentration of the components. Either discrete domains of the lower concentration component are dispersed in a matrix of the majority component, or two co-continuous phases exist simultaneously.[6] Blends of two semi-crystalline materials generally form separate crystalline domains depending on the rate of crystallisation and the molecular weight distribution.[7] Co-crystallisation can also occur due to similar crystallisation rates of different components which are thermodynamically miscible and often arises in blends of different types of polyethylenes, for example.[8] Despite co-crystallisation being a kinetic process, melt miscibility is a requirement for this process to occur.[9]

Various morphologies can be induced by strategic blending ratios, temperature control or thermal, chemical or mechanical stresses. In semi-crystalline polymers quench cooling reduces the degree of crystallinity and produces smaller crystalline domains while the converse is true for slow cooling. Mechanical drawing of semi-crystalline polymers also forces orientation of chains in the direction of drawing, inducing further crystallisation or changing the crystal structures of existing crystals.[10], [11]

2.2 Solid-state NMR spectroscopy as a tool for understanding solid polymers

2.2.1 Basic principles

Understanding the complex relationship between the factors mentioned above requires characterisation of both structural and dynamic aspects of solid polymers. Historically, methods used to probe molecular characteristics were indirectly extrapolated from bulk mechanical properties such as tensile strength, creep or stress relaxation.[12], [13] The solid state of semi-crystalline polymers has also been well-characterised by scattering techniques such as X-ray diffraction from identification of crystal structures[14],[15] to changes in properties after external stresses[10] and correlation of processing times with morphology development[16]. Despite these widespread applications, however, X-ray diffraction provides little to no information regarding amorphous polymers and the amorphous regions of semi-crystalline polymers, limiting its application to a small variety of polymer systems.

The advancement of solid-state NMR spectroscopic technologies has provided a method to directly explore the molecular characteristics of solid polymer systems without the limitations of crystallinity as in the case of X-ray diffraction. Additionally, solid-state NMR spectroscopic methods can also provide insight into the dynamics of the polymer system by using a variety

of pulse sequences and techniques designed to take advantage of the interactions present in the solid state.

Solution NMR spectroscopic methods are well-known in the fields of chemical and material science research. The most common application is structural elucidation by the characterisation of nuclei in specific environments by their unique chemical shift values. Intermolecular interactions result in J-coupling through bonds and facilitate accurate assignments of nuclei. Three-dimensional structural elucidation is achieved via through-space interactions which can be detected through the nuclear Overhauser effect or NOE.

The key difference between solution state and solid-state NMR spectra is the linewidth of the resonances. The broadened linewidth of solid-state resonances is a direct result of the dipolar interactions which bind a solid together.[17] The sharp resonances observed in solution NMR spectra occur due to the averaging of anisotropic interactions as a result of the rapid motion of molecules in the liquid state. In the solid state, this averaging does not occur and the interactions which hold the solid together influence the spectrum. The inability of solid-state NMR spectroscopy to resolve signals hindered the development of the technique until Andrew and Lowe suggested the introduction of artificial motions within the solid by rotation of the sample about and axis oriented at 54.74° which could suppress the dipolar interactions.[18] The angle 54.74° then became known as the “magic angle” and the method was named magic-angle spinning or MAS. The efficiency of the MAS method is dependent on the spinning of the sample occurring at frequencies equal to or greater than the dipolar linewidth, which can span many kilohertz. In cases where the spinning rate is not high enough to overcome the differences in chemical shift arising from various orientations within the sample (known as chemical shift anisotropy) a phenomenon known as spinning side bands (SSBs) occurs on the spectrum. SSBs are peaks arising from the splitting of a signal with frequency differences equal to the rate of MAS.[17] At faster MAS rates the distance between the split peaks increases and the intensity decreases. The second method for the removal of undesirable spin interactions is the application of RF fields. While MAS is achieved through rotations in space, the RF decoupling is based on the rotation of spins. Two types of decoupling sequences exist; these are multi-pulse sequences and continuous irradiation sequences. Decoupling is typically used in conjunction with MAS to effectively remove all anisotropic interactions. Continuous irradiation or continuous wave (CW) decoupling is the most basic of the decoupling methods during which the proton nucleus is continuously irradiated while the X nucleus (e.g. ^{13}C) is being detected.[19] For CW decoupling the efficiency of the decoupling is dependent on the decoupling frequency and the amplitude or power of the irradiation. Since this method is only dependent on these two parameters, CW decoupling requires little optimisation and typically better results can be achieved with higher amplitudes, however, the maximum amplitude is

limited by the power of the amplifying equipment. Even better results can be achieved through multi-pulse decoupling with further alternation of phases. The most well-known methods are the two-pulse phase modulation (TPPM) method and the SPINAL-64 method. The TPPM method separates the continuous irradiation into discrete sections and the phase is alternated between angles ϕ and $\phi + \Delta\phi$ as shown in Figure 2.1. The effect of the phase alternation is to cause additional averaging of the heteronuclear coupling enhancing the decoupling efficiency which leads to narrower linewidths compared to CW decoupling. The SPINAL-64 sequence is based upon the TPPM method but involves a more complex phase pattern over 64 discrete blocks of irradiation. This means that in both cases (TPPM and SPINAL) the pulse width and the phase are additional parameters to be optimised. While SPINAL typically yields better decoupling efficiency than TPPM, the sensitivity of SPINAL to the optimisation is greater. In the case of SPINAL the decoupling would need to be optimised for every sample or risk achieving even worse decoupling than the CW method. For this reason the TPPM method is most universally used. Further developments focused on the observation of nuclei of low relative abundance, such as ^{13}C, the solution to which was the cross-polarisation method. Cross-polarisation involves the transfer of polarisation of abundant nuclei, such as ^{1}H, to rare nuclei like ^{13}C to the enhance signal to noise ratio of spectra of nuclei of low relative abundance. The combination of cross-polarisation and MAS techniques has formed the basis of most solid-state NMR spectroscopic analysis.

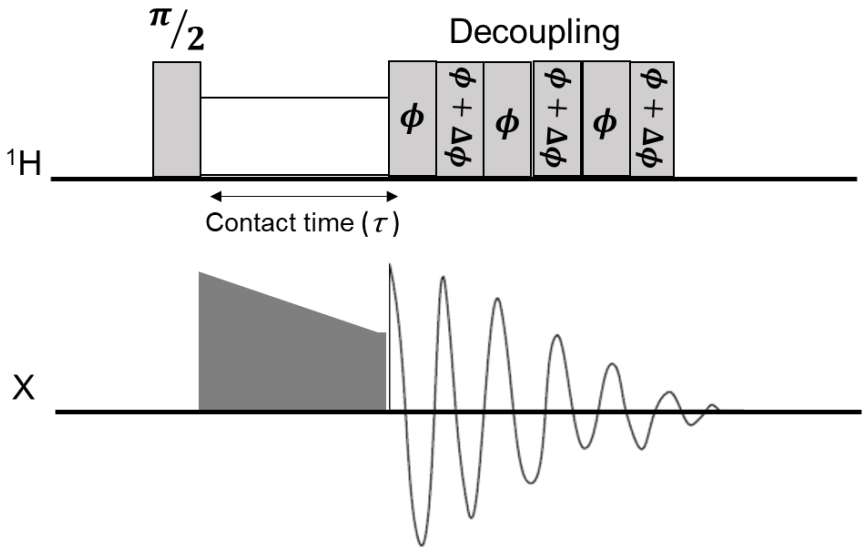

Figure 2. 1 TPPM decoupling method

Due to the intricacy of the relationship between polymer properties and molecular structure, powerful analytical techniques are required to successfully describe this relationship. Solid-

state NMR spectroscopy is one of the techniques especially suited to this purpose. The long-chain nature of polymers in addition to the existence of possibly multiple property distributions results in dynamic processes occurring at extremely different timescales. As is often the case in solid polymer NMR analysis, molecular realignments of specific amplitudes on certain timescales leads to potential loss in signal intensity and inefficient detection as a result of low values for one of the different types of relaxation times or inefficient polarization transfer during cross-polarisation. Therefore, any sample with structural and dynamic inhomogeneity, such as in polymers, requires that the NMR method yields information which is representative of the whole sample.[20]

Important spectral parameters used for polymer characterisation are the chemical shift, signal intensity and linewidth, coupling constants and rates of relaxation.[21] Solid state NMR spectroscopy is able to differentiate between various chain configurations, conformations as well as larger scale morphological differences since the frequencies (and therefore the chemical shifts) of the atoms in the backbone and side-chains are highly sensitive to local magnetic surroundings. Exploitation of these various spectral parameters through specific pulse sequences for the applications relevant to this study will be explained in the following sections.

2.2.2 The Proton Wideline Experiment

The term “Wideline NMR spectroscopy” has been applied to cases where nuclei generate broad resonances due to the effects of dipolar interactions, quadrupolar interactions or where chemical shift anisotropy is great.[22] The experiment involves a simple single pulse excitation sequence in the proton channel under static conditions. Despite the obvious advantages of high-resolution solid-state NMR spectroscopy and the years of research devoted to spectra which mimic the resolution obtained by solution NMR spectroscopy, static wideline spectra are still often employed. A Wideline spectrum is dominated by dipolar coupling resulting in a single resonance which can span kilohertz in breadth. While distinct chemical environments cannot be identified by Wideline NMR spectroscopy, the spectrum does provide a wealth of information regarding molecular mobility. The broader the linewidth of the resonance the higher the rigidity of the sample being analysed due to the strength of the dipolar interactions present. These broad signals are often mathematically processed into constituent components where the sample is known to contain multiple domains of varying mobilities. This concept can be applied to semi-crystalline polymers in order to distinguish between the amorphous and crystalline domains as well as the interfaces between them. In such cases the broad base of the resonance constitutes the rigid crystalline domain while the amorphous domains can often be fitted to a Lorentzian distribution due to their high mobility as in Figure 2. 2. Wideline

experiments can be performed easily over wide temperature ranges and have therefore been applied to a variety of applications[17], from proteins to lignin.[23]

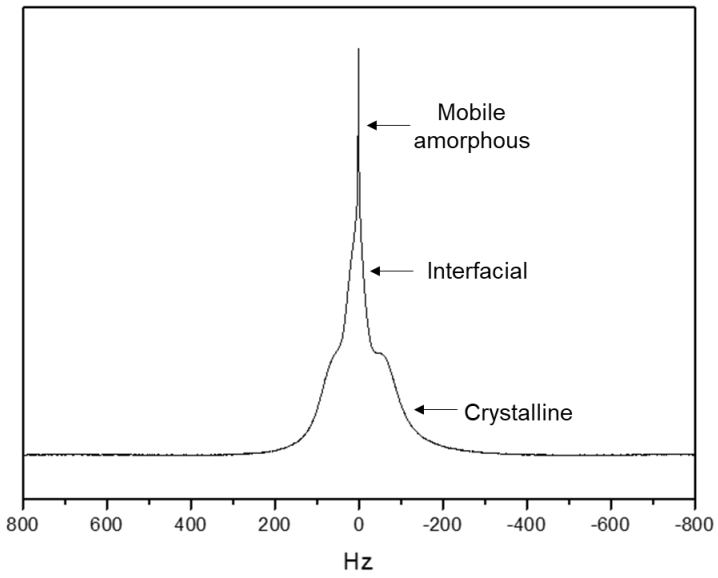

Figure 2. 2: Example of wideline spectrum of semi-crystalline sample

2.2.3 The CP/MAS Experiment

The method of cross-polarisation (CP) was introduced as a solution to the low signal intensity of nuclei of low relative abundance. The CP method involves generating the magnetisation on a nucleus of high natural abundance, such as ^{1}H, followed by the transfer of this accumulated magnetisation to the nuclei of low abundance.[19] Figure 2. 3 displays the pulse sequence for a typical CP experiment. An initial 90° radio-frequency (RF) pulse is applied in the proton channel and is followed by a contact pulse which generates the spin-locking field.[19] Effective magnetisation transfer can only occur when the energy levels of the rotating frames of the highly abundant nucleus and the low abundance nucleus are equal.[24] This condition is called the Hartmann-Hahn match, shown in Equation 2.1. The Hartmann-Hahn match is the reason for the shortening of relaxation times during the CP experiment. Nuclei of low natural abundance tend to have long relaxation times, resulting in excessively long experiment durations since nuclei should be fully relaxed before successive RF pulses. Since the polarisation transfer occurs from the abundant nucleus to the low abundance nucleus, the relaxation time of the abundant nucleus dictates the relaxation delay.

$$\gamma_H B_{1H} = \gamma_X B_{1X} \qquad \text{(Eq. 2.1)}$$

This matching condition is not always easily achieved. For short values of the contact time the polarisation transfer occurs between the closest ^{1}H and X nucleus exclusively, however, increasing durations of contact time a redistribution of magnetisation occurs across protons

resulting in an extended transfer process.[19] CP is also reduced during the spin-locking time due to relaxation of the ^{1}H magnetisation at a sample specific rate of $T_{1\rho}$. While this parameter requires optimisation for the maximum CP and spectral intensity, variable contact time experiments can also be exploited to probe cross-polarisation dynamics which can yield insight into polymer mobility. Any factors affecting the dipolar coupling between nuclei influence the polarisation transfer, this includes MAS which results in averaging of interactions as previously described. CP under MAS is enhanced by the altering the contact pulse to include variable amplitudes to mitigate the effects of MAS.[19] This is one of the limitations of the CP method, the intensities of the signals are not absolute and display a dependency on the contact time, the Hartmann-Hahn match, the strength of the interaction between the abundant and dilute nuclei as well as the rate of relaxation. In addition, in cases where coupling is weak, CP is reduced such as samples of high mobility. It also follows that those quaternary carbons cannot be detected by CP since no protons are present to transfer polarisation from.

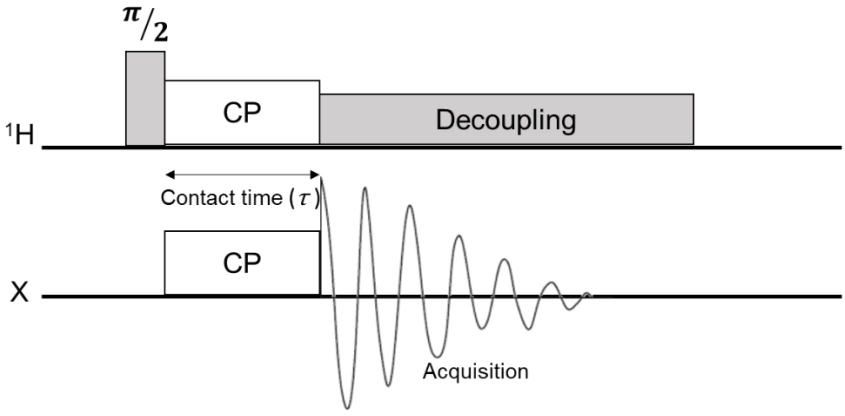

Figure 2. 3: Pulse sequence diagram for a typical cross-polarisation experiment

2.2.4 The Interrupted Decoupling experiment

Interrupted decoupling (also called dipolar dephasing) combined with CP is a spectral editing experiment which suppresses resonances due to protonated X nuclei. Carbon magnetisation is generated through CP after which the RF pulse is stopped for time τ resulting in the rapid dephasing of all carbon magnetisation which have strong coupling to protons. Restarting the RF pulse in the proton channel then reveals only the carbon signals which are weakly coupled to protons.[25] Methyl signals are also visible in a dipolar dephased spectrum as they display a variety of dipolar coupling due to the varying extent of freedom of motion.[26] Figure 2.4 illustrates a typical interrupted decoupling (IDREF) pulse sequence involving a break in the decoupling on the proton channel during which the dephasing of strongly proton-coupled carbons dephase.

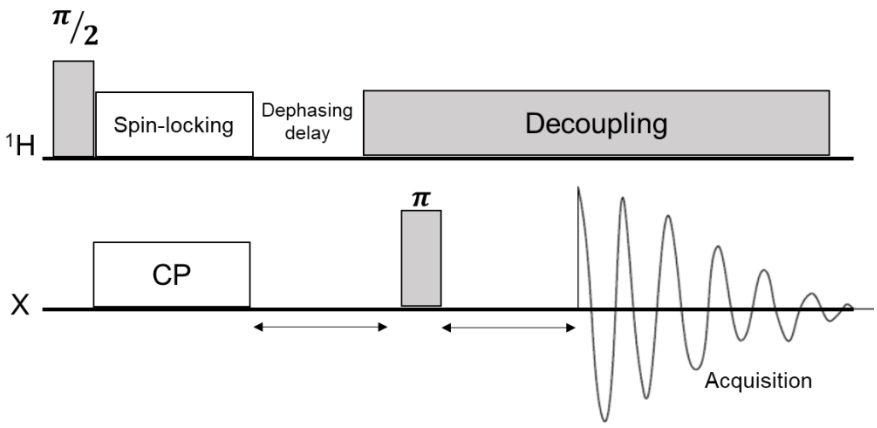

Figure 2. 4 Pulse sequence diagram for a typical IDREF experiment

2.2.5 Spin Relaxation

Spin relaxation is one of the most important processes in NMR spectroscopy and has found several applications. The relaxation rate is termed such as it describes the rate at which a spin system relaxes or returns to its original equilibrium state. This relaxation occurs due to a time dependent dissipation of the dipolar interactions between nuclei. Two main types of relaxation are known; spin-lattice (T_1) relaxation describes the return of the spin populations to Boltzmann distributions following an RF pulse and spin-spin (T_2) relaxation describing the loss of phase coherence of the total magnetisation.[24] Relaxation processes in the rotating frame ($T_{1\rho}$) have also been distinguished and comprise spin-lattice relaxation in the rotating frame.

Nuclear relaxation studies in solids are used to understand the dynamics of molecules. As described above, these relaxation processes occur due to variations in the interactions between nuclear spins which arise as a result of molecular motions. The various relaxation processes display sensitivity to different frequencies of motion. T_1 relaxation processes are sensitive to motions on the order of the Larmor frequency (in the range of 10 – 100+ MHz) while T_2 relaxation processes are sensitive to low frequencies of motion.[19] Consequently, relaxation methods can be used to characterise a full range of molecular motion within a solid. Relaxation spectra are often analysed as decay functions and modelled according to the appropriate correlation function. These functions are used to generate the values of the relaxation times. The accuracy of these calculations depends on various experimental optimisations and, most importantly, the nature of the sample itself. The mobilities of the various domains are required to be separated by an order of magnitude at minimum in order to be properly resolved and unambiguously interpreted.

Spin-lattice (T_1) relaxation times in the solid state can be used to infer the rigidity of a solid by the length of the relaxation time. T_1's are generally determined to guide quantitative analysis

by other pulse sequences. Fully quantitative spectra can only be achieved provided all the carbons are fully relaxed between consecutive RF pulses.[27] For solids, the accepted standard delay between pulses is 5 times the longest T_1 in the system. This method has often been applied to determine the appropriate relaxation delay for quantitative CP/MAS experiments to determine degree of branching in polyethylenes.[28], [29], [30] In pharmaceutical research spin-lattice relaxation has also been used to study molecular mobility of specific functional groups in amorphous solid dispersions to improve dissolution of drugs of poor solubility.[31]

Spin-lattice relaxation in the rotating frame ($T_{1\rho}$) finds regular application in the determination of molecular reorientation in solids at intermediate timescales. The timescale of $T_{1\rho}$ relaxation is particularly suited to characterisation of domains in phase-separated systems. The limit of phase segregation in graft-copolymers,[32] the internal protein dynamics of biological solids[33] as well as the miscibility of blends[34] have all been investigated via $T_{1\rho}$. In cases where no protons are bonded to a carbon of interest, the chemical shift anisotropy (CSA) tensor can be used to probe dynamics, as was quantitatively proven by Quinn et al.[35]

An important aspect to note at this point is the difference between both T_1 and $T_{1\rho}$ for rare and abundant nuclei. For rare nuclei, the T_1 and $T_{1\rho}$ relaxation times are not affected by spin diffusion and can be quantified through the well-known pulse sequences which yield different dynamic information for nuclei which are not chemically equivalent. In contrast, for abundant nuclei such as protons both T_1 and $T_{1\rho}$ are greatly influenced by spin diffusion causing large variations between the experimental relaxation times and the actual values.[31]

The T_2 relaxation time is determined by the spin-echo pulse sequence (Figure 2. 5). The initial pulse sequence is similar to that of the single pulse excitation experiment, however, after the 90° RF pulse a period of τ is included during which the system loses phase coherence. A 180° RF pulse is then applied to invert and refocus the spins. During the experiment, the values of τ are varied and an exponential decay of the magnetisation is observed as a function of τ. Spin-spin relaxation has also been used to study phase separations and various domains within solids. In polyolefins, the reorientation of chain segments and chain diffusion within non-crystalline domains specifically causes partial averaging of dipolar interactions and thus increases the values of T_2.[36] The relationship between the value of T_2 and the extent of the averaging is dependent on the morphology and dynamics, thus the interfacial region between crystalline and amorphous domains can be identified by its unique rate of relaxation compared to that of the amorphous regions.[37], [38]

T_2 relaxation is often determined under static conditions as the spin-spin relaxation is proportional to the motional frequencies and the linewidth of the static spectrum. Domains

within the solid which exhibit different dynamic behaviour can therefore be quantified and phase changes can be observed when time or temperature is varied.

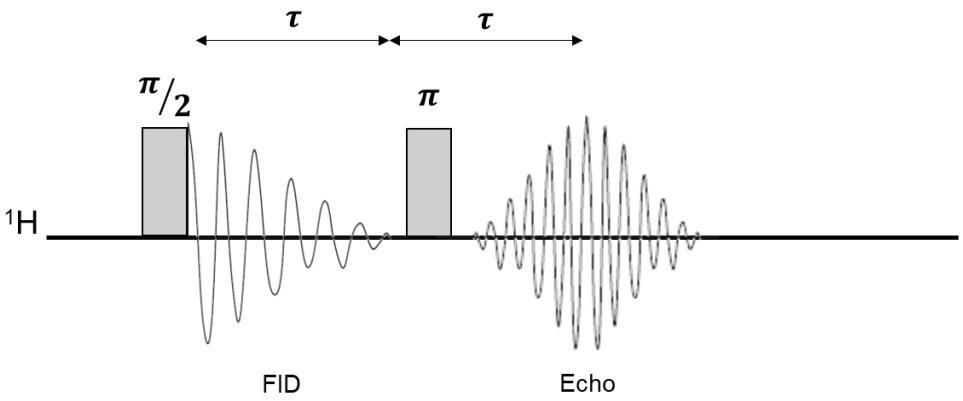

Figure 2. 5: Spin-echo pulse sequence

Many more solid-state NMR experiments exist and have been applied to polymer analysis. The experiments explained above represent a summary of the theory relevant to the applications described in successive chapters in this dissertation. Detailed theory of experimental design and relevant concepts for interpretation are presented per chapter.

2.3 Additional techniques for solid-state characterisation

2.3.1 Differential Scanning Calorimetry (DSC)

DSC is a popular thermal analysis technique which measures changes in the heat capacity of a material with temperature or time. The heat flow through a sample is measured relative to a reference sample under a controlled temperature environment. The reference sample is typically an empty cell, or one filled with an inert material. Changes in heat flow can be characteristic of specific thermal events such as melting, crystallisation or glass transition.[39]

Of interest in this study are the first order thermal transitions such as melting and crystallisation since the properties of the material change dramatically beyond these points. Given that polymers form distributions of crystallites, the melting and crystallisation events will occur as broad peaks depending on the heterogeneity of the distribution. These peaks are often integrated to determine the degree of crystallinity (ΔH_f) from a calibrated DSC instrument using the variation of the heat capacity as a function of temperature according to Equation 2.2 where H_f is the enthalpy of fusion of the analysed sample and H_{fc} is the enthalpy of fusion of a fully crystalline sample of the same polymer.[40]

$$\Delta H_f = {H_f}/{H_{fc}} \qquad \text{(Eq. 2.2)}$$

2.3.2 X-ray diffraction (XRD)

The primary technique for determination of crystalline structures of materials is x-ray diffraction. The technique is based on the principle that x-rays are scattered from objects in the nanometre range, resulting in an interference pattern. Constructive interference is only obtained when the conditions of Bragg's Law (Equation 2.3) are met. Bragg's Law expresses the relationship between the wavelength of the incident light (λ) and the lattice spacing (d) in a three-dimensional crystalline arrangement.[41]

$$n\lambda = 2d\ sin\theta \qquad \text{(Eq. 2.3)}$$

The XRD analysis of polymers is more complex due to the inability to obtain single crystals as well as the presence of the amorphous regions which cause diffuse scattering along the baseline of the diffractogram known as the 'amorphous halo'. Polymers rarely produce perfect crystals and the presence of defects results in broadening of the diffraction peaks when compared to small molecule diffractograms. [40]

Additionally, the lattice parameters of polymer crystals exhibit a dependency on external factors such as temperature or strain. Since polymers possess a distribution of crystal sizes the diffractograms of polymers are snapshots of the crystalline distribution at a specific time or under specific conditions. Should external conditions favour recrystallisation into smaller crystallites these crystallites then become of appropriate size to scatter X-rays and may be detected in the diffractogram where they had not been detectable before.

The low intensities resulting from weak bonding in specific directions of crystal axes[40] as well as the secondary intensity contributions of the arrangement of pendant groups in the crystal lattice leads to the difficulty of accurately determining polymer crystal structures. These problems are often solved by obtaining diffraction patterns of model structures as reference.

2.3.3 Infrared Spectroscopy (FTIR)

FTIR spectroscopy is an essential analytical technique due to the quick, and decisive results which can be obtained. The basis of the technique is that upon the radiation of a sample with an infrared beam some of the radiation is absorbed while the rest is transmitted. The infrared region of light can be described by three categories; near IR (10 – 400 cm^{-1}), mid-IR (400 – 4000 cm^{-1}) and far IR (4000 – 14 000 cm^{-1}).[42] These photons have sufficient energy to cause vibrations within groups of atoms or functional groups relative to the bonds between them. The distinct energies required for these vibrational transitions correlate to specific vibrational modes of chemical bonds.[42]

The spectrum of infrared radiation which is absorbed or transmitted is characteristic of the molecular structure of the specific material and can be used as a ‘fingerprint’ of the sample. In addition, the peak intensity directly correlates to the quantity of material present allowing FTIR to be used for qualitative and quantitative analysis.

References

[1] S. Koltzenburg, M. Maskos, O. Nuyken, Polymers in Solid State, in: Polym. Chem., Springer Berlin Heidelberg, Berlin, Heidelberg, 2017: pp. 93–103. https://doi.org/10.1007/978-3-662-49279-6_4.

[2] L.H. Sperling, Introduction to Physical Polymer Science, 4th ed., John Wiley & Sons, 2006.

[3] E.H. Andrews, Structure-Property Relationships in a Polymer, Int. J. Polym. Mater. Polym. Biomater. 2 (1973) 337–359. https://doi.org/10.1080/00914037308072367.

[4] R.B. Seymour, C.E.J. Carraher, Structure-Property Relationships in Polymers, Plenum Press, 1985.

[5] Q. Guo, ed., Polymer Morphology, Wiley, Hoboken, NJ, USA, 2016.

[6] C. Harrats, S. Thomas, G. Groeninckx, Micro- and nanostructured multiphase polymer blend systems: Phase morphology and interfaces, Taylor & Francis, 2005. https://doi.org/10.1002/macp.200600584.

[7] S. Hu, T. Kyu, R.S. Stein, Characterization of properties of polyethylene blends I. Linear low-density polyethylene with high-density polyethylene, J. Polym. Sci. Part B Polym. Phys. 25 (1987) 71–87. https://doi.org/10.1002/polb.1987.090250509.

[8] J. Xu, X. Xu, L. Chen, L. Feng, W. Chen, Effect of composition distribution on miscibility and co-crystallization phenomena in the blends of low density polyethylene with conventional and metallocene-based ethylene-butene copolymers, Polymer (Guildf). 42 (2001) 3867–3874. https://doi.org/10.1016/S0032-3861(00)00756-4.

[9] R.L. Morgan, M.J. Hill, P.J. Barham, Morphology, melting behaviour and co-crystallization in polyethylene blends: the effect of cooling rate on two homogeneously mixed blends, Polymer (Guildf). 40 (1999) 337–348. https://doi.org/10.1016/S0032-3861(98)00193-1.

[10] M.S. Sevegney, G. Parthasarthy, R.M. Kannan, D.W. Thurman, L. Fernandez-Ballester, Deformation-induced morphology changes and orientation behavior in syndiotactic polypropylene, Macromolecules. 36 (2003) 6472–6483. https://doi.org/10.1021/ma025774+.

[11] C.R. López-Barrón, Y. Zeng, J.J. Schaefer, A.P.R. Eberle, T.P. Lodge, F.S. Bates, Molecular alignment in polyethylene during cold drawing using in-situ SANS and Raman spectroscopy, Macromolecules. 50 (2017) 3627–3636. https://doi.org/10.1021/acs.macromol.7b00504.

[12] J.M. Lagarón, G. Capaccio, L.J. Rose, B.J. Kip, Craze morphology and molecular orientation in the slow crack growth failure of polyethylene, J. Appl. Polym. Sci. 77 (2000) 283–296.

[13] R.H. Ericksen, Creep of aromatic polyamide fibres, Polymer (Guildf). 26 (1985) 733–746. https://doi.org/10.1016/0032-3861(85)90111-9.

[14] K. Mezghani, P.J. Phillips, The γ-phase of high molecular weight isotactic polypropylene. II: The morphology of the γ-form crystallized at 200 MPa, Polymer (Guildf). 38 (1997) 5725–5733. https://doi.org/10.1016/S0032-3861(97)00131-6.

[15] D. Mileva, R. Androsch, D. Cavallo, G.C. Alfonso, Structure formation of random isotactic

copolymers of propylene and 1-hexene or 1-octene at rapid cooling, Eur. Polym. J. 48 (2012) 1082–1092. https://doi.org/10.1016/j.eurpolymj.2012.03.009.

[16] A. Elmoumni, H.H. Winter, A.J. Waddon, H. Fruitwala, Correlation of material and processing time scales with structure development in isotactic polypropylene crystallization, Macromolecules. 36 (2003) 6453–6461. https://doi.org/10.1021/ma025948n.

[17] V.I. Bakhmutov, Solid-State NMR in Materials Science, CRC Press, 2012. https://doi.org/10.1201/b11301.

[18] E.R. Andrew, Magic Angle Spinning in Solid State NMR Spectroscopy, Philos. Trans. R. Soc. London. 299 (1981) 505–520.

[19] M.J. Duer, ed., Solid-State NMR Spectroscopy Principles and Applications, Blackwell Science Ltd, Oxford, UK, 2001. https://doi.org/10.1002/9780470999394.

[20] K. Saalwächter, Applications of NMR in Polymer Characterization – An Introduction, in: NMR Methods Charact. Synth. Nat. Polym., 2019: pp. 3–22.

[21] B.J. Hunt, M.I. James, eds., Polymer characterisation, 1993. https://doi.org/10.1007/978-94-011-2160-6.

[22] A.W. MacGregor, L.A. O'Dell, R.W. Schurko, New methods for the acquisition of ultra-wideline solid-state NMR spectra of spin-1/2 nuclides, J. Magn. Reson. 208 (2011) 103–113. https://doi.org/10.1016/j.jmr.2010.10.011.

[23] G. Gilardi, L. Abis, A.E.G. Cass, Wide-line solid-state NMR of wood: Proton relaxation time measurements on cell walls biodegraded by white-rot and brown-rot fungi, Enzyme Microb. Technol. 16 (1994) 676–682. https://doi.org/10.1016/0141-0229(94)90089-2.

[24] F.A. Bovey, P.A. Mirau, Fundamentals of Nuclear Magnetic Resonance, in: NMR Polym., Academic Press, 1996: pp. 1–115. https://doi.org/https://doi.org/10.1016/B978-012119765-0/50001-9.

[25] M.S. Solum, D.M. Grant, R.J. Pugmire, 13C Solid-State NMR of Argonne premium coals, Energy and Fuels. 3 (1989) 187–193. https://doi.org/10.1021/ef00014a012.

[26] L.B. Alemany, D.M. Grant, T.D. Alger, R.J. Pugmire, Cross polarization and Magic Angle Sample Spinning NMR spectra of model organic compounds. 3. Effect of the 13C-1H dipolar interaction on cross polarization and carbon-proton dephasing, J. Am. Chem. Soc. 105 (1983) 6697–6704. https://doi.org/10.1021/ja00360a025.

[27] H.J. Assumption, J.P. Vermeulen, W.L. Jarrett, L.J. Mathias, A.J. Van Reenen, High resolution solution and solid state NMR characterization of ethylene/1-butene and ethylene/1-hexene copolymers fractionated by preparative temperature rising elution fractionation, Polymer (Guildf). 47 (2006) 67–74. https://doi.org/10.1016/j.polymer.2005.11.020.

[28] M. Pollard, K. Klimke, R. Graf, H.W. Spiess, M. Wilhelm, O. Sperber, C. Piel, W. Kaminsky, Observation of chain branching in polyethylene in the solid state and melt via 13 C NMR spectroscopy and melt NMR relaxation time measurements, Macromolecules. 37 (2004) 813–825. https://doi.org/10.1021/ma0349130.

[29] G.B. Galland, R.F. de Souza, R.S. Mauler, F.F. Nunes, 13 C NMR determination of the composition of linear low-density polyethylene obtained with [η 3 -methallyl-nickel-diimine]PF 6 complex, Macromolecules. 32 (1999) 1620–1625. https://doi.org/10.1021/ma981669h.

[30] A.L. Cholli, W.M. Ritchey, J.L. Koenig, V.S. Veeman, Separation of components in crystalline and amorphous regions of polyethylene by solid state carbon-13 NMR spectroscopy, Spectrosc. Lett. 21 (1988) 519–531. https://doi.org/10.1080/00387018808082327.

[31] A. Paudel, M. Geppi, G. Van Den Mooter, Structural and dynamic properties of amorphous solid dispersions: The role of solid-state nuclear magnetic resonance spectroscopy and relaxometry, J. Pharm. Sci. 103 (2014) 2635–2662. https://doi.org/10.1002/jps.23966.

[32] W. Elhrari, H. Assumption, P.E. Mallon, Correlation between positron annihilation lifetime

parameters and T1ρ relaxation times determined from solid state NMR at the compositional phase segregation point of graft copolymers, Polymer (Guildf). 77 (2015) 95–101. https://doi.org/10.1016/j.polymer.2015.09.006.

[33] A. Krushelnitsky, D. Reichert, K. Saalwächter, Solid-state NMR approaches to internal dynamics of proteins: From picoseconds to microseconds and seconds, Acc. Chem. Res. 46 (2013) 2028–2036. https://doi.org/10.1021/ar300292p.

[34] Y. Koseki, K. Aimi, S. Ando, Crystalline structure and molecular mobility of PVDF chains in PVDF/PMMA blend films analyzed by solid-state 19F MAS NMR spectroscopy, Polym. J. 44 (2012) 757–763. https://doi.org/10.1038/pj.2012.76.

[35] C.M. Quinn, A.E. Mcdermott, Quantifying conformational dynamics using solid-state R1ρ experiments, J. Magn. Reson. 222 (2012) 1–7. https://doi.org/10.1016/j.jmr.2012.05.014.Quantifying.

[36] M. Wang, G.M. Bernard, R.E. Wasylishen, P. Choi, A solid-state 13C NMR investigation of the morphology of single-site and Ziegler-Natta linear low-density polyethylenes with varying branch contents, Macromolecules. 40 (2007) 6594–6599. https://doi.org/10.1021/ma071119w.

[37] K. Kuwabara, H. Kaji, F. Horii, D.C. Bassett, R.H. Olley, Solid-state 13C NMR analyses of the crystalline−noncrystalline structure for metallocene-catalyzed linear low-density polyethylene, Macromolecules. 30 (1997) 7516–7521. https://doi.org/10.1021/ma970581l.

[38] R. Kitamaru, F. Horii, K. Murayama, Phase structure of lamellar crystalline polyethylene by solid-state high-resolution 13C NMR: Detection of the crystalline-amorphous interphase, Macromolecules. 19 (1986) 636–643. https://doi.org/10.1021/ma00157a026.

[39] C. Schick, Differential scanning calorimetry (DSC) of semicrystalline polymers, (n.d.). https://doi.org/10.1007/s00216-009-3169-y.

[40] D. Campbell, R.A. Pethrick, J.R. White, Polymer Characterization - Physical tecniques, 2nd editio, Taylor & Francis, 2000.

[41] M. Woolfson, An Introduction to X-ray Crystallography, 2nd editio, Cambridge University Press, 2003.

[42] A. Dutta, Fourier Transform Infrared Spectroscopy, in: Spectrosc. Methods Nanomater. Charact., Elsevier Inc., 2017: pp. 73–93. https://doi.org/10.1016/B978-0-323-46140-5.00004-2.

Chapter 3
NMR characterisation of vis-broken heterophasic ethylene-propylene copolymers

This work has been published in *Macromolecular Reaction Engineering,* DOI: 10.1002/mren.202000039

3.1 Introduction

Heterophasic ethylene-propylene copolymers (HEPCs), also referred to as impact copolymers, are of great commercial importance due to their superior impact resistance compared to that of isotactic polypropylene.[1] HEPCs consist of a rubbery ethylene-propylene copolymer phase dispersed in an isotactic polypropylene matrix. This complex chemical composition and microstructure occur as a result of a combination of effects of the catalyst system and production process.[2][1][3] These copolymers are produced commercially using Ziegler-Natta catalysis yielding polymers with broad molecular weight distributions.[4] In conventional polypropylene produced by heterogeneous transition metal catalysts, a high average molecular weight and a broad molecular weight distribution is also characteristic.[5] In order to enhance processability and allow for injection moulding applications[6] a post-polymerisation step involving peroxide treatment in an extruder is included to decrease the average chain length, forming what is known as a controlled rheology grade polypropylene.[7] Controlled rheology polypropylene possesses a narrower molecular weight distribution by effectively removing the high molecular weight tail of the distribution. This results in a more Newtonian shear viscosity behaviour permitting the use of lower processing temperatures and higher spinning speeds when processing into fibres or thin films.[8] In the case of HEPCs a similar vis-breaking treatment can be applied for the same reasons. The necessity of this step is due to the inability of the catalyst system to produce low molecular weight material. While this step is necessary, its effect on the mechanical properties of the resultant impact copolymer is undesirable.[9][10] The effect of the vis-breaking process on impact copolymers is not well understood as the chemical structure of these copolymers is highly complex. HEPCs contain varying distributions of ethylene- and propylene-rich regions. This presents challenges in predicting the manner in which the copolymers will be affected by vis-breaking. In contrast, the process and mechanism of vis-breaking for conventional polypropylene is well documented.[8],[11],[12], [13],[14]

Controlled rheology (also referred to as vis-breaking) is based on chain scission induced by free radicals, exploiting the mechanism of oxidative degradation of polypropylene. As polyolefins in general are susceptible to oxidative and photochemical degradation, polymer modifications which make use of these radical reactions need precise decomposition rates depending on the processing conditions. Therefore, radical sources with specific thermal

decomposition temperatures and thus controlled radical initiation are ideal. The radical source is most often an organic peroxide such as dicumylperoxide[14],[15],[16],2,5-dimethyl-2,5-di-tert-butylperoxyhexane (DHBP)[7],[17],[18] or cyclic peroxides such as 3,6,9-Triethyl-3,6,9-trimethyl-1,4,7-triperoxonane (Trigonox® 301)[9] which forms primary radicals following thermal decomposition. The cyclic peroxides have the advantage of not releasing volatile gases as in the case of the acyclic organic peroxides.[7],[19] Since the radicals attack substrates in a random fashion the statistical probability that a monomer in a longer chain reacts with a radical is greater since the distribution of chain sizes generally implies that monomers are more likely to occur in longer chains than shorter chains. This leads to break down of the longer chains and decrease of the overall molecular weight distribution. The use of inorganic peroxides has been reported in literature[8] but has not been implemented industrially due to the high reactivity of these peroxides which requires low reaction temperatures. This limits the applicability to semi-crystalline polymers which require high temperature reactive modifications.

The extent and type of oxidative degradation of polymers is dependent on the structure of the chains. Radicals formed on a polymer chain can cause branching, crosslinking and chain scission, with the latter being the dominant mechanism of degradation in polypropylene.[16] The presence of the methyl group in polypropylene leads to a positive inductive effect which decreases the strength of the C – H bond on the same carbon.[8] The generally accepted mechanism of organic radical-induced chain scission of polypropylene is shown in Figure 3. 1. The primary radical abstracts a proton from the tertiary carbon atom forming a tertiary radical on the backbone. This alkyl radical undergoes β scission and results in the formation of an unsaturated chain end as well as a propagating radical on a polypropylene chain.[5] While polyethylenes do not readily undergo β scission due to the unfavourable formation of primary radicals, the structure of the polypropylene chain results in the formation of secondary radicals which are energetically preferred.[8] The resultant double bond is not likely to undergo addition with the macro radicals formed by β scission due to the high electron density of the double bond and the nucleophilic nature of the radical. Instead the rate of reaction of the formed radical with oxidative species or molecular oxygen is much higher, ensuring the propagation of the oxidative degradation.[8] For polyethylenes, the tendency to crosslink in the presence of organic peroxides is much greater.[20] Upon degradation polyethylenes form macro radicals which can either undergo hydrogen abstraction or disproportionation.[21] The hydrogen abstraction route leads to long chain branching while the disproportionation pathway forms unsaturated chain ends.[22] Since HEPCs contain both propylene and ethylene sequences, it is unpredictable whether chain scission or crosslinking will be favoured. It is also uncertain whether crosslinking will occur at all due to the low quantity and low molecular weight of the

ethylene sequences. Statistically, the greater presence of CH_2 groups in ethylene rich sequences suggests that the radical would preferentially interact with a methylene group in these sequences. Degradation in ethylene rich sequences would therefore proceed as described for polyethylenes. In propylene rich sequences the $CH\text{-}CH_3$ group is the dominant group, and the radical would then be more likely to interact with the CH group. The resultant effect would depend on the relative ratios of ethylene- and propylene-rich environments.

While the mechanism of action of organic peroxides on polypropylene is understood, the same cannot be said of HEPCs. Considering the significant commercial value of HEPCs, developing an understanding of the vis-breaking process has great consequence. For understanding changes in chemical composition nuclear magnetic resonance (NMR) spectroscopy is an unrivalled tool. Specifically in the solid state, the state in which most polymers find their application, morphological changes induced by the effects of organic peroxides can be traced during the vis-breaking process. While HEPCs and injection moulding grade impact polypropylenes are commercially available these materials undergo a variety of thermal steps and contain a number of additives. This makes analysis of the effect of vis-breaking on morphology ambiguous. Therefore, in this study, the process of vis-breaking in polypropylene impact copolymers degraded during the solid-state NMR spectroscopic analysis is investigated and characterised in terms of chemical composition and morphology using both solution and solid-state NMR spectroscopy. For the first time, we report the use of solid state NMR spectroscopy to monitor vis-breaking *in-situ* and directly identify the affected components and morphological changes as a result thereof.

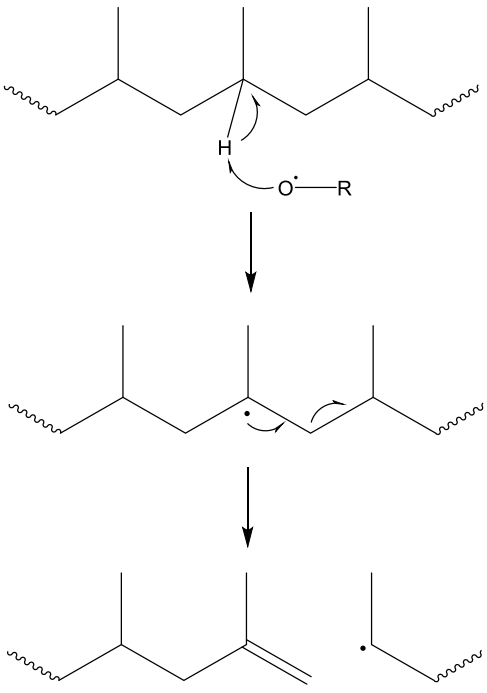

Figure 3. 1: Mechanism of vis-breaking of polypropylene

Table 3. 1: Molecular weight parameters of HEPC samples before vis-breaking

Sample	Time* (min)	Mn (kDa)	Mw (kDa)	Đ
T0	0	46	250	5.41
T180	180	65	295	4.54
T300	300	53	312	5.90

* Time elapsed after ethylene introduction into second reactor stage

3.2 Materials and Methods

3.2.1 Materials

Heterophasic ethylene-propylene copolymers were obtained from Sasol Polymers. Samples were acquired from a two-series reactor of a continuous gas phase polymerisation process. Sampling was performed at various ethylene polymerisation times after the introduction of isotactic polypropylene from the first of the two-series reactors. Sample T0 was obtained 0 minutes after introduction of the isotactic polypropylene and therefore contains little to no ethylene. Samples T180 and T300 were obtained after 180 and 300 minutes of ethylene polymerisation respectively and therefore contains increasing quantities of ethylene. Samples were vis-broken by treating 10 g of sample with 0.5 wt% Trigonox® 301 at 190 °C in a Wirsam Scientific melt flow indexer (MFI). Each sample was allowed a residence time of 30 minutes in the barrel of the MFI. After 30 minutes the sample was pushed out of the MFI using a 2.16 kg weight and rapidly cooled on the metal collecting plate.

3.2.2 Solution state NMR spectroscopy

Untreated and vis-broken HEPCs were analysed on a Varian^{Unity} Inova 600 MHz NMR spectrometer using a 5mm broadband probe. A 90° pulse of 7.4 µs duration was used with a 1.8 s acquisition time and relaxation delay of 15 s to obtain quantitative ^{13}C spectra with an average of 4000 scans. All spectra were proton decoupled using inverse gated decoupling. Samples (40-50 mg) were dissolved in deuterated tetrachloroethane (0.75 mL) (d-TCE, Sigma-Aldrich, South Africa). Analysis was performed at 120 °C with no stabiliser added to prevent any ambiguity between stabiliser signals and low intensity signals of EP sequences. ^{13}C spectra of copolymers were referenced to the tertiary carbon bb peak for the PPP sequence at 28.7 ppm. This reference compensates for the absence of the EEE peak at 30 ppm in some samples.

3.2.3 Solid- and melt-state NMR spectroscopy

All solid-state NMR spectra were obtained using a Varian VNMRS 500 MHz NMR spectrometer. A 4 mm ChemagneticsTM HX T3 MAS probe was used with 4 mm zirconia rotors. Magic angle spinning (MAS) was carried out at 5 kHz using adamantane as an external chemical shift standard with the downfield peak referenced to 38.3 ppm. ^{13}C cross-polarisation (CP) spectra were performed on untreated samples both with and without 0.5 wt% organic peroxide. CP spectra were recorded at 30 °C before heating to 190 °C (T_M + 25 °C). Single pulse spectra were acquired at 190 °C after 0, 10 and 30 minutes. Another CP spectrum was obtained at 30 °C after cooling down from 190 °C. Nitrogen gas was used for variable temperature pneumatics. All ^{13}C CP spectra were proton decoupled using the two-pulse phase modulated (TPPM) decoupling sequence with a 3.5 µs 90° pulse with a recycle delay of 5 seconds. CP contact time was 1 ms and acquisition time was 30 ms with 64 scans. Single pulse spectra were acquired using a 90° pulse of 2.25 ms with recycle delay of 5s, acquisition time of 30 ms and 64 scans.

Peak deconvolutions and integrations were performed using OriginPro® 8.5 software. Lorentzian or Gaussian fitting functions were applied to all calculations.

3.2.4 Differential Scanning Calorimetry

DSC thermograms were acquired using a Netzsch DSC Polyma 214 calorimeter. Samples were heated to 190 °C and maintained isothermally for 30 minutes. Subsequently the samples were cooled to 0 °C and heated and cooled again. The heating and cooling rates were kept constant at 10 K/min. Melting points and enthalpies were determined from the second heating thermogram. All sample masses were between 5 – 6 mg. Temperature calibration was performed with indium standards.

3.2.5 X-ray Diffraction

X-ray diffraction (XRD) was performed on a Bruker D2 Phaser at room temperature. Diffraction patterns were obtained for values of 2θ from 10 – 50°. The values of $K\alpha_1$ and $K\alpha_2$ were 1.5406 and 1.54439 respectively. Samples for XRD were prepared in the DSC by heating to 190 °C, annealing for 30 minutes at this temperature and subsequently cooling to room temperature to mimic the solid-state NMR experiment.

3.3 Results and Discussion

3.3.1 Chemical structure by solution NMR spectroscopy

Peak assignments for methylene carbons followed the nomenclature introduced by Carman and Wilkes.[23] The symbol δ+ refers to a methylene group more than four carbons away from a tertiary carbon. The assignment of tertiary carbons is denoted by CH_{xx}, where x represents the Greek notation used for methylene carbons. Methyl carbons are denoted CH_{3xx} and will have the same Greek notation of the tertiary carbon it is attached to. A summary of the notation used is given in Figure 3. 2.

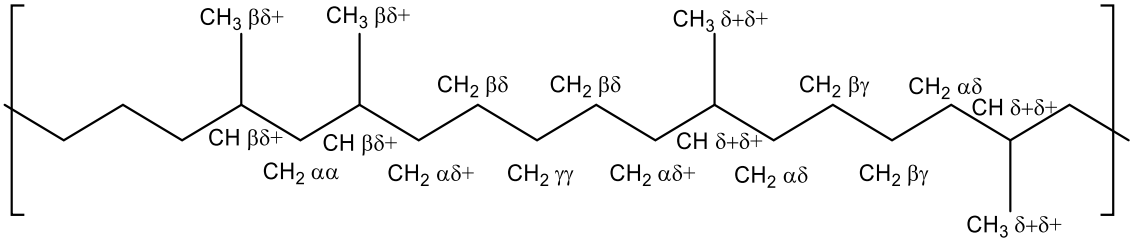

Figure 3. 2: Summary of nomenclature used to describe resonances from tertiary, secondary and primary carbons

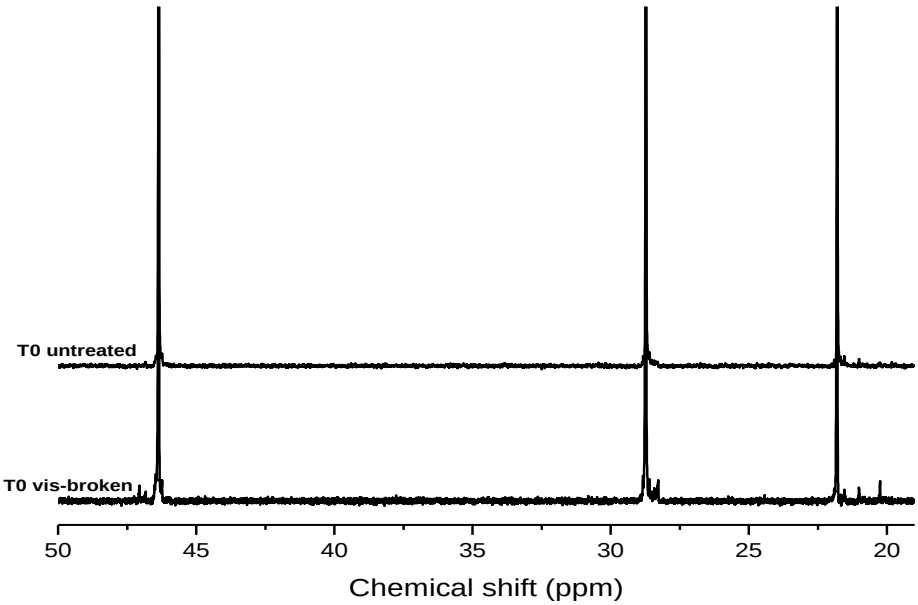

Figure 3. 3: ^{13}C solution NMR spectrum of T0

The primary effect of the vis-breaking process is to decrease chain length and narrow the chain length distribution. The molar mass distributions in Figure 3. 4 prove that the vis-breaking performed in this study was successful in these aspects.

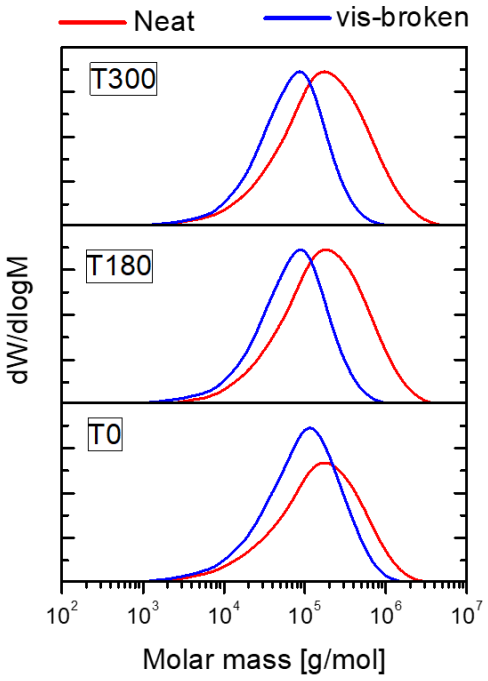

Figure 3. 4: Size exclusion chromatograms of polypropylene T0, T180 and T300 samples before and after vis-breaking by MFI

The ^{13}C NMR spectrum of the isotactic polypropylene (T0) sample in Figure 3. 3 is dominated by the three main polypropylene peaks at 46.3, 28.7 and 21.8 ppm for methylene, methine and methyl respectively both before and after vis-breaking. Therefore, the T0 sample displayed minimal structural changes after peroxide treatment. Most polypropylenes produced with heterogeneous Ziegler catalysts achieve approximately 98 % isotacticity. This means that even highly isotactic material contains low quantities of defects, which arise either due to stereo errors in the relative position of the methyl group or due to mis insertions. After vis-breaking, a relative increase in the concentration of the smaller peaks possibly due to stereo- and regio-defects occurs. This effect was as result of the decrease in chain length after vis-breaking leading to an apparent increase in defects per chain. Alternatively, depending on the position where chain scission occurred, the vis-breaking process could also cause the formation of groups which resemble regio-defects. Specifically, the increase in the peak at 20.2 ppm was quite significant. Busico and co-workers have performed extensive research on the assignments of polypropylenes containing various defects.[24][25] Following the results of their analysis the 20.2 ppm peak corresponds to the syndiotactic arrangement of methyl groups. The peak at 21.0 ppm also displayed an increase in intensity and corresponds to stereo errors which resulted in a change in tacticity sequence such as the *mmrm* sequence.[24]

In comparison, the ^{13}C NMR spectra of the copolymers in Figure 3. 5a and b showed several changes in the ethylene-propylene sequences after vis-breaking. The T180 sample displayed slight changes in the relative quantities of the isolated and random insertions while the majority of the changes in the T300 sample occurred within long ethylene or long propylene sequences. These changes could be more easily seen in the normalised pentad sequences shown in Table 3. 2. In the table, ethylene and propylene content are normalised to a total of 100 %, meaning that while degradation occurred in a propylene region the ratio would automatically increase total ethylene. It is, however, the apparent ethylene content and not the total ethylene content which increases. It should also be noted that the chains in the copolymers contain a distribution of ethylene sequences and that the T300 sample contained a certain amount of ethylene homopolymer.[26] The T300 sample displayed a decrease in the long-chain ethylene sequences as well as in the PEP centred pentads while few other significant changes occurred. It should be noted that while the T300 sample contained approximately double the ethylene content of the T180 sample, the most notable difference in ethylene-propylene sequences arose in the long-chain ethylene sequences. This suggested that the increased effect of the peroxide treatment visible in the T180 sample, when compared to both the T0 and T300 samples, was most likely due to the presence of very short ethylene sequences within longer propylene sequences. These “junction points” or points of sequence transition appeared to act as weaknesses in the chain for the action of the organic peroxide. This could be due to the structural changes which occur after the insertion of an ethylene unit during the polymerisation. The short ethylene sequences disrupt the crystallisation of the isotactic propylene segments implying that wherever these junction points exist they cannot be incorporated into a crystal lattice and benefit from the protection of the lattice. In addition, polypropylenes crystallise in a helical configuration, meaning that the ability of the helices to fit into one another is disrupted by the structural defects.[27] [28]

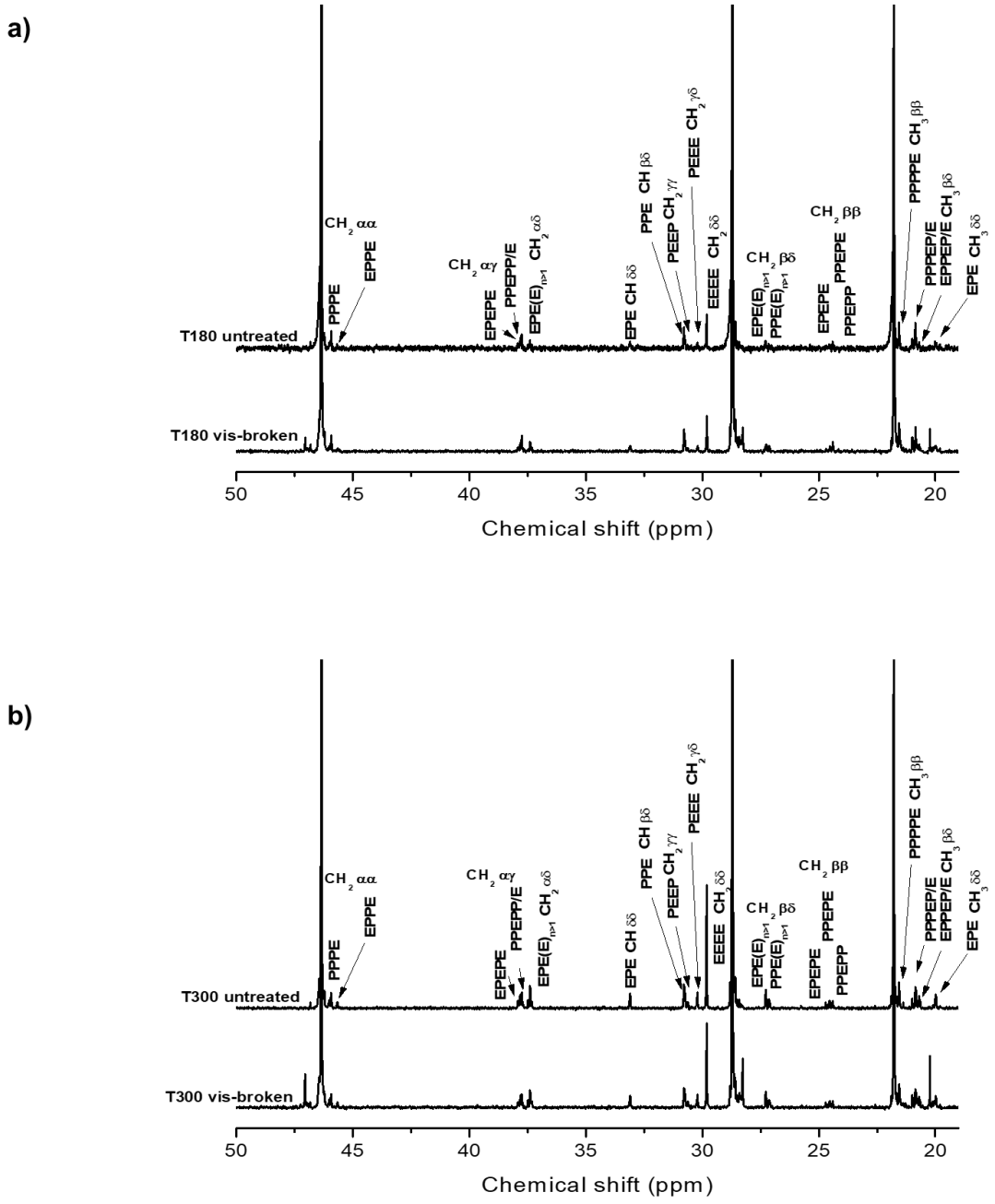

Figure 3. 5: ^{13}C solution NMR spectra of untreated and vis-broken samples of a) T180 and b) T300

Table 3. 2: ^{13}C solution NMR normalised pentad sequence distributions for neat and peroxide treated copolymers

Sample	mol % P	mol % E	EEEEE	EPEPE	PPEPP/E	PPEPE	PPEPP	PPPPP
T180	95.9	4.1	2.7	0.5	2.1	0.4	0.5	93.8
T180 vis-broken	95.7	4.3	2.7	0.7	2.3	0.5	0.8	93.0
T300	88.4	11.6	9.0	1.2	3.8	0.9	0.8	84.3
T300 vis-broken	90.6	9.4	7.3	1.2	2.7	0.9	0.8	87.2

3.3.2 In-situ vis-breaking by solid state NMR spectroscopy

The three signals characteristic of polypropylene could be observed in all NMR spectra. These signals were due to methylene, methine and methyl carbon atoms appearing at 45.1, 27.8 and 21.8 ppm respectively. Table 3. 2 shows the chemical composition of the samples which vary from polypropylene homopolymer (T0) to high ethylene content copolymer (T300) with an ethylene content of 11 mol%. Since the maximum ethylene content is 11 mol%, the majority of the sample remains polypropylene homopolymer and therefore the major peaks observed in the NMR spectra are polypropylene peaks. At this low concentration peaks due to ethylene sequences could not be observed by solid state NMR spectroscopy. Solid state NMR spectroscopy was used mainly to monitor peroxide effects on chain packing within the polypropylene domains of the homopolymer and copolymers. This was done using the chemical shift differences which arise between crystalline and amorphous domains. These differences in chemical shift are known to be due to the γ-gauche effect in which the gauche chain conformation results in an enhanced shielding effect in the amorphous regions.[29] The γ-gauche effect does not occur in crystalline regions as the chains are arranged in all-trans zig-zag conformation with less shielding. Figures 3.6 – 3.8 display the single pulse spectra of samples T0, T180 and T300 respectively.

The in-situ vis-breaking method allows one to gain insight into the process of vis-breaking while the polymer is in the molten state. While solid-state NMR spectroscopy has benefits over solution-state NMR spectroscopy in terms of solubility issues and increased quantities of sample and therefore greater sensitivity, solution NMR spectroscopy still has the upper-hand in terms of resolution. The compromise between these two techniques is analysis of the sample in its molten state (melt-state

NMR spectroscopy). By using melt-state NMR spectroscopy, the rapid motion in the melt results in averaging of the linewidths of carbon signals which occur much broader below melting temperature due to dipolar coupling of carbon and proton signals and chemical shift anisotropy.[30][31][32] The motional averaging above melting temperature combined with MAS techniques enables acquisition of near high-resolution ^{13}C spectra at high field strengths and larger probe dimensions. Melt-state NMR spectroscopy also has its disadvantages, namely the long relaxation delays required between scans as well as the spinning instabilities which occur as a result of the molten sample spinning at high speeds.[32] The single pulse sequence was used to acquire spectra in the melt state since cross-polarisation displays no signals when the sample is in the molten state due to high molecular mobility. The loss of efficient CP was used as an indication that the sample was fully mobile before single pulse acquisition.

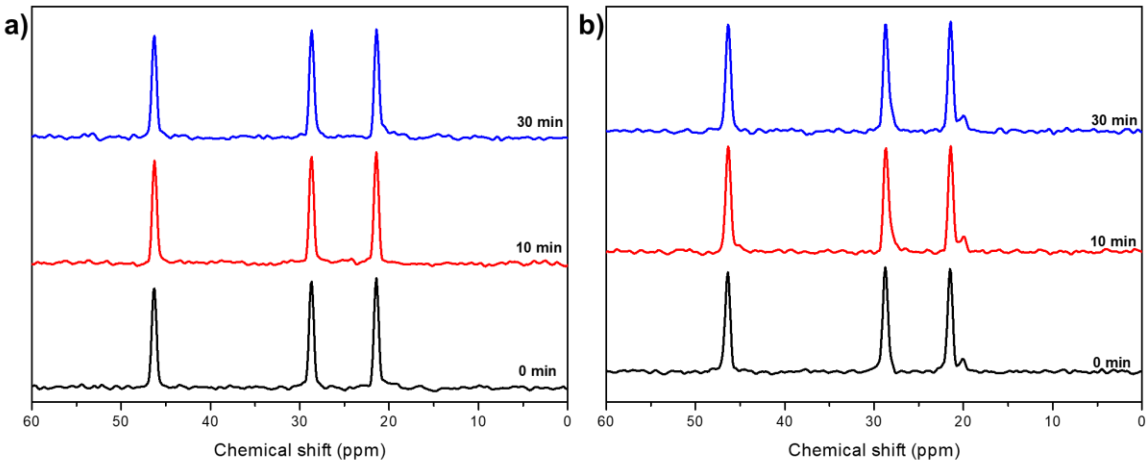

Figure 3. 6: ^{13}C melt-state NMR single pulse spectrum of sample T0 at 190 °C a) without peroxide and b) with peroxide

A comparison of Figure 3. 6a and b show that the T0 sample was affected by the presence of the peroxide. A shoulder developed on the methyl signal at approximately 20 ppm, which indicated the presence of another non-equivalent environment within the melt state. The structures formed as a result of chain scission occurring during thermal degradation in the presence of low quantities of oxygen form additional chemical environments.[33] This results in the appearance of new peaks due to the change in orientation of the methyl groups. In addition, the effect extends to the methine and methylene carbons resulting in a broadening of the main signals.

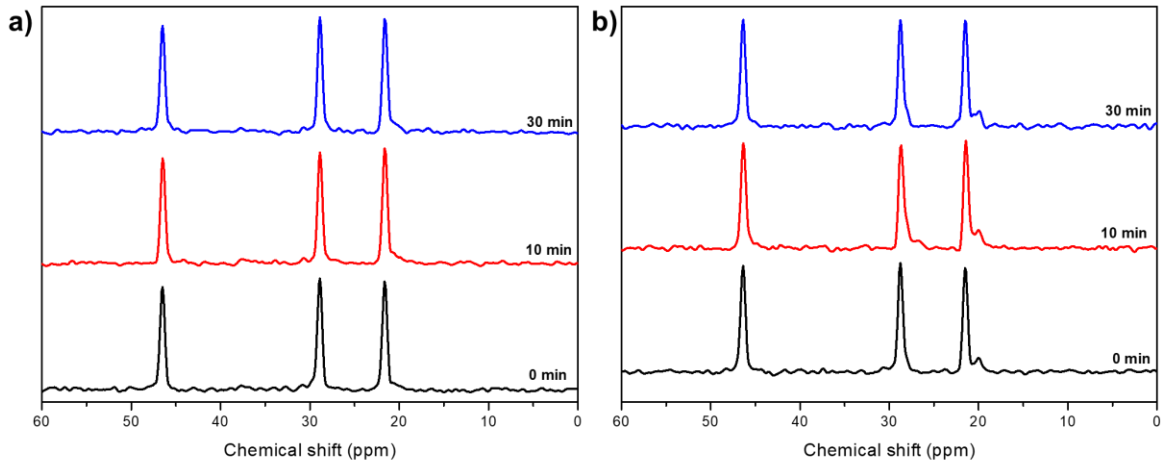

Figure 3. 7: ^{13}C melt-state NMR single pulse spectrum of sample T180 at 190 °C a) without peroxide and b) with peroxide

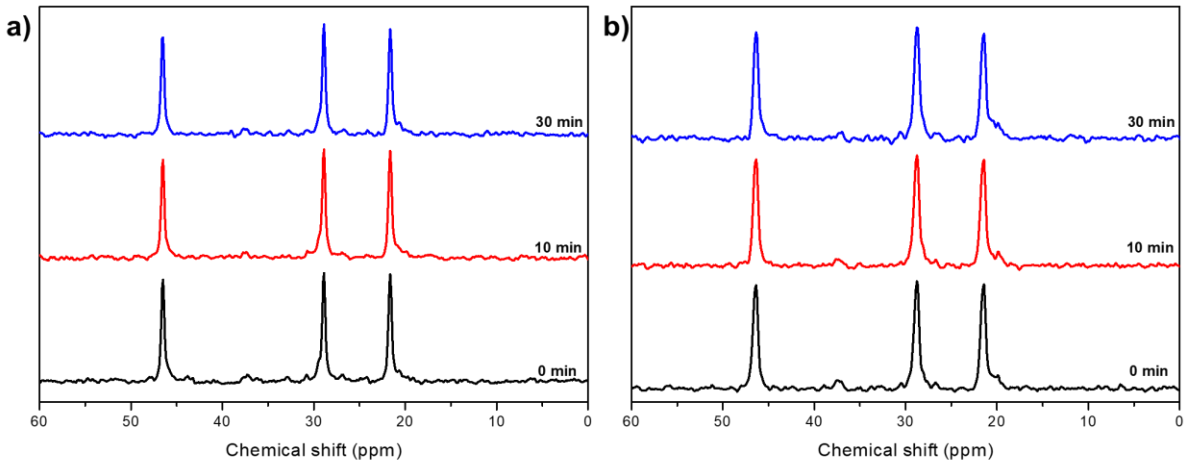

Figure 3. 8: ^{13}C melt-state NMR single pulse spectrum of sample T300 at 190 °C a) without peroxide and b) with peroxide

The shoulder on the methyl peak in the single pulse spectrum of the T180 sample in Figure 3. 7b appeared to be better defined than that of the T300 sample in Figure 3. 8b. This suggested that the T300 sample was less affected by the presence of the peroxide than the T180 sample. A comparison of the single pulse spectra of the T300 sample with and without peroxide in Figure 3. 8a and b showed that the T300 sample showed a greater susceptibility to thermal degradation. The effect of the peroxide on the development of the amorphous shoulder could be quantified by deconvoluting the methyl peak from the amorphous shoulder. Figure 3. 9 depicts the evolution of the relative area of the amorphous shoulder with time in the presence of peroxide for all three samples. The amorphous contribution was seen to be greatest in the T180 sample. The T0 sample displayed a gradual increase in relative

amorphous area while the amorphous contribution of the T300 sample remained essentially constant. The asterisk in Figure 3. 9 denotes peaks which could only be fitted using three components, as demonstrated in the expansion in Figure 3. 10. The formation of three domains in the solid state NMR spectrum has been reported previously [34] and can be linked to the formation of new chemical environments after vis-breaking as mentioned previously. The three domains observed in the single pulse spectrum therefore correlate to the varying degrees of defects within the chemical structure as a result of the gradient of chemical sequences which can be found within HEPCs.[9],[35]

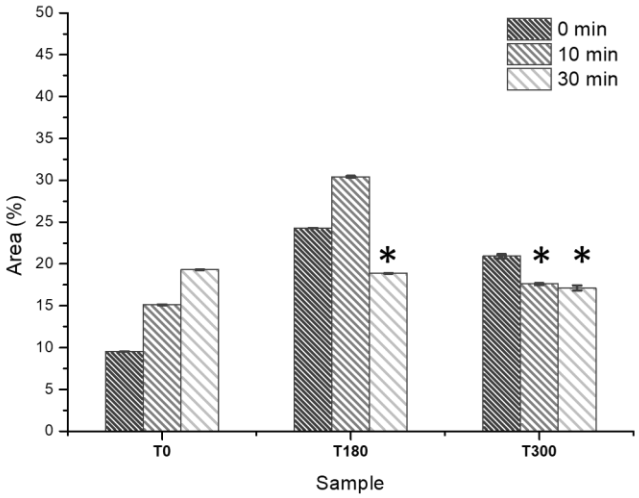

Figure 3. 9: Evolution of relative area of amorphous shoulder with time at 190 °C from ^{13}C melt-state NMR single pulse spectra

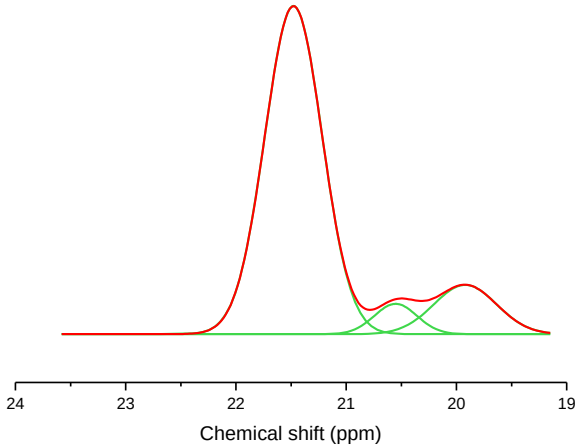

Figure 3. 10: Expanded plot of 3 regions in methyl peak in ^{13}C melt-state NMR single pulse spectrum of T180 after 30 minutes in the presence of peroxide. The red curve indicates the total signal while the green curves indicate the deconvoluted components of the signal

The changes in the chemical structure as a result of the chain scission reactions inevitably lead to faults in the polypropylene helices and thus disruption of the crystallisability of the bulk polymer once crystallised from the molten state.[36] The CP/MAS spectrum of the T0, T180 and T300 samples after vis-breaking in Figure 3. 11, Figure 3. 13 and Figure 3. 14 proved the differences in the response of each sample to the vis-breaking process. Figure 3. 12 displays the array used to determine the appropriate recycle delay for CP/MAS experiments. Optimal peak intensities for all peaks were observed after 5 seconds and no further improvement was observed thereafter.

The CP/MAS of the T0 sample displayed a decrease in intensity of the methine and methyl peaks while the T180 sample showed a shift in the peaks towards lower chemical shifts. In contrast, the CP/MAS of the T300 sample displayed splitting of the resonances. The splitting of the peaks into doublets as demonstrated by the T300 sample was evidence of the formation of the disordered crystal phase within the α structure. It is possible that the length of the chain and therefore the extension of crystalline domains along the length of the chains allowed the accommodation of certain defects in the structure within the crystalline regions or alternatively, aggregation of these defects at the interface separating the crystalline regions from the disordered regions[37]. The area where this flaw in the crystal structure occurs results in increased mobility within the crystalline domain in addition to the separate phase which is the amorphous domain. Based on the changes in chemical shift within the T180 sample the disordered phase became more significant resulting in enhanced crystal mobility[38] for the entire distribution of crystal domains. The T300 sample appeared to exclude the disordered phase and form separate domains of ideal crystals and disordered crystals. While both

polyolefins are vulnerable to oxidative degradation, polyethylene is less likely to undergo β scission than polypropylene due to the instability of the primary radical formed when cleaving linear hydrocarbons.[8] This could explain the persistence of some ideal crystal domains within the T300 sample. Work by Agarwal et al. also found that for HEPCs with high ethylene content the phase separation between propylene rich and ethylene rich regions resulted in a lesser formation of rubber-amorphous phase[39], supporting the theory that T300 formed separate domains.

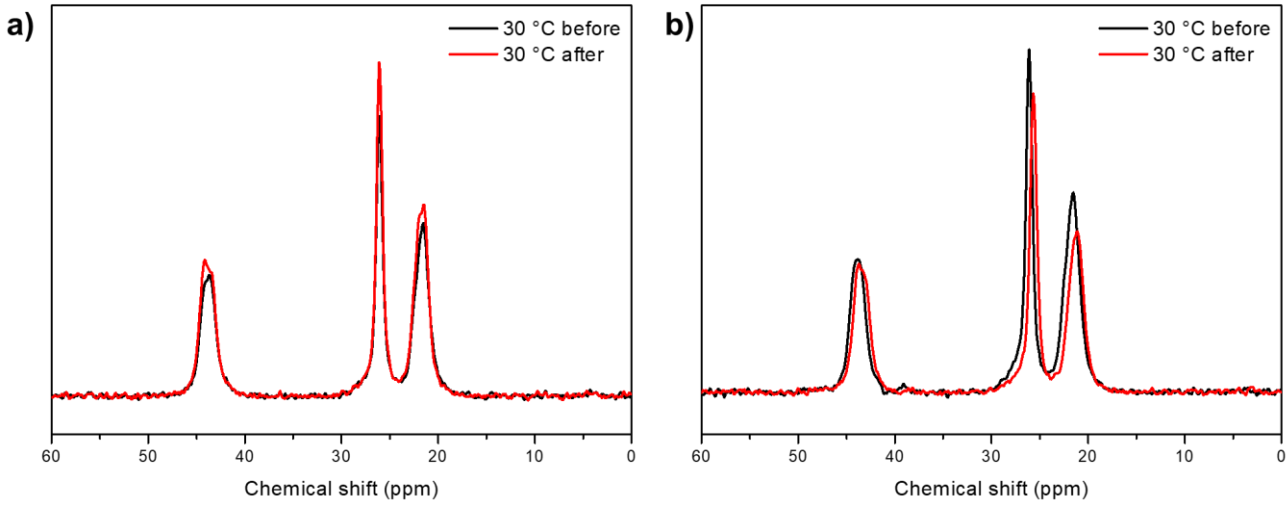

Figure 3. 11: ^{13}C solid state NMR CP/MAS spectrum of sample T0 at 30 °C before and after 30 minutes at 190 °C a) without peroxide b) with peroxide

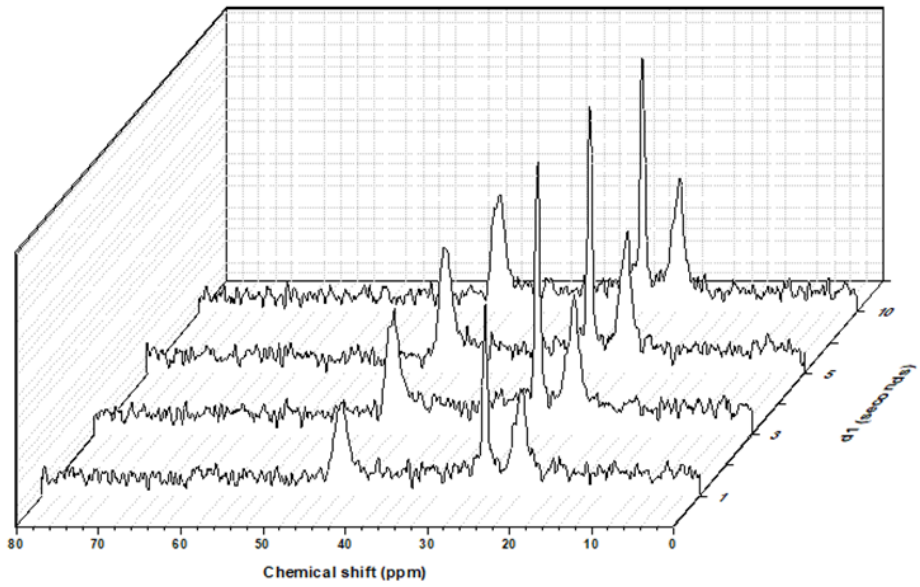

Figure 3. 12: Testing optimal recycle delay for CPMAS spectra

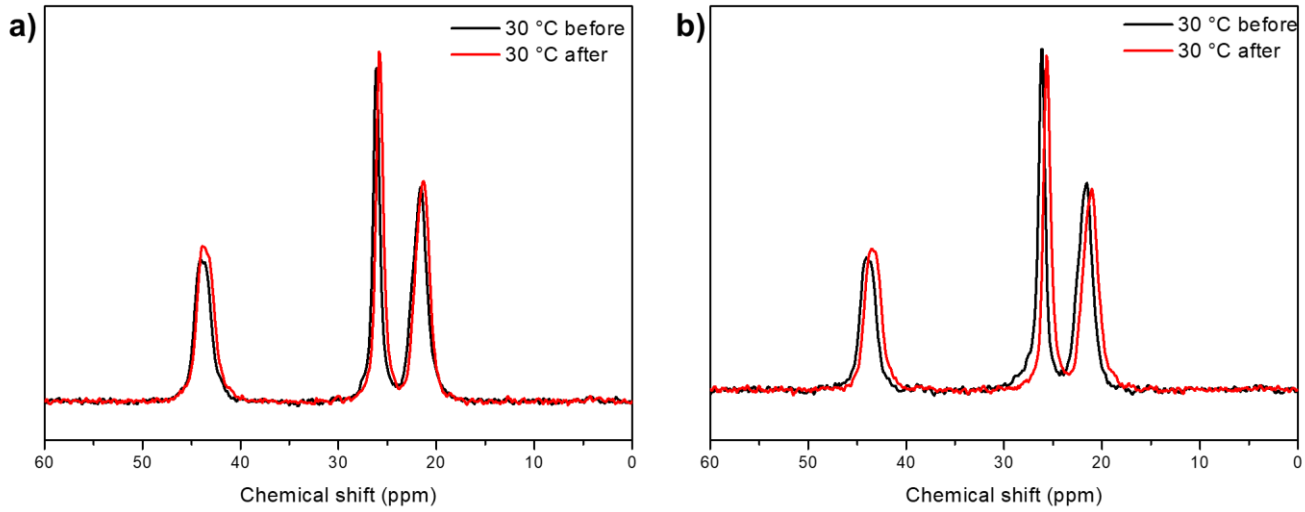

Figure 3. 13: ^{13}C solid state NMR CP/MAS spectrum of sample T180 at 30 °C before and after 30 minutes at 190°C a) without peroxide b) with peroxide

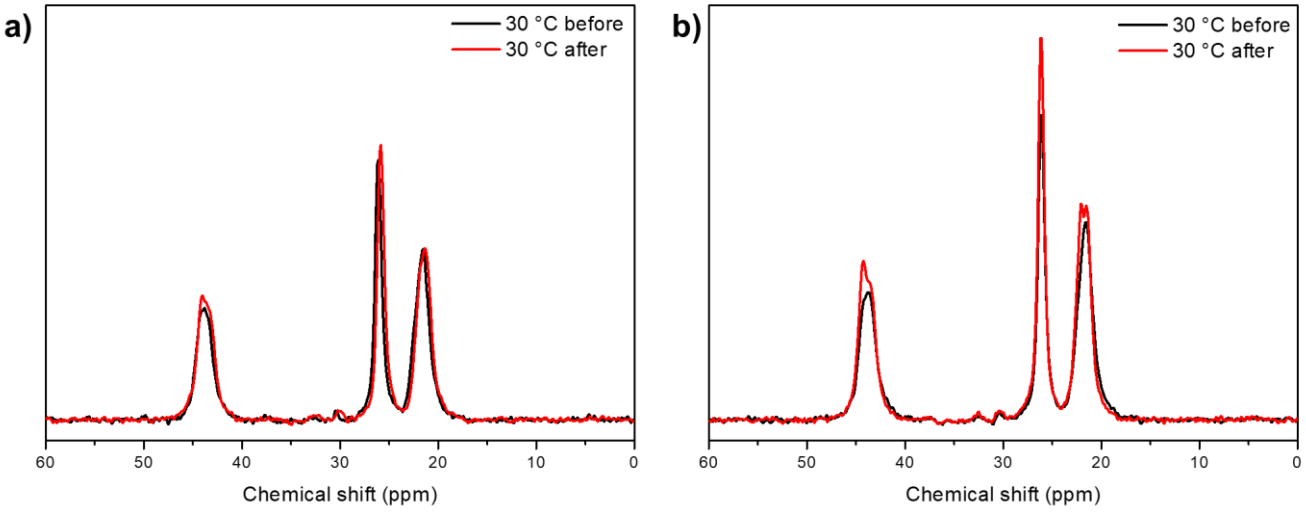

Figure 3. 14: ^{13}C solid state NMR CP/MAS spectrum of sample T300 at 30 °C before and after 30 minutes at 190 °C a) without peroxide b) with peroxide

The change in peak area of the methylene and methyl peaks before and after vis-breaking is depicted in the graph in Figure 3. 15a and b. Generally the peak intensities in a cross-polarisation experiment are not quantitative, however, since these spectra were all acquired under similar conditions some deductions can be made about the strength of the dipolar interactions or the molecular mobility.[40] In all cases the total area of the methylene peak increased while the area of the methyl peak decreased. This corresponded to an increase in intensity and a narrowing of the peak width, as can be seen in the CP/MAS spectra, which signified an increase in the average mobility of the entire system.

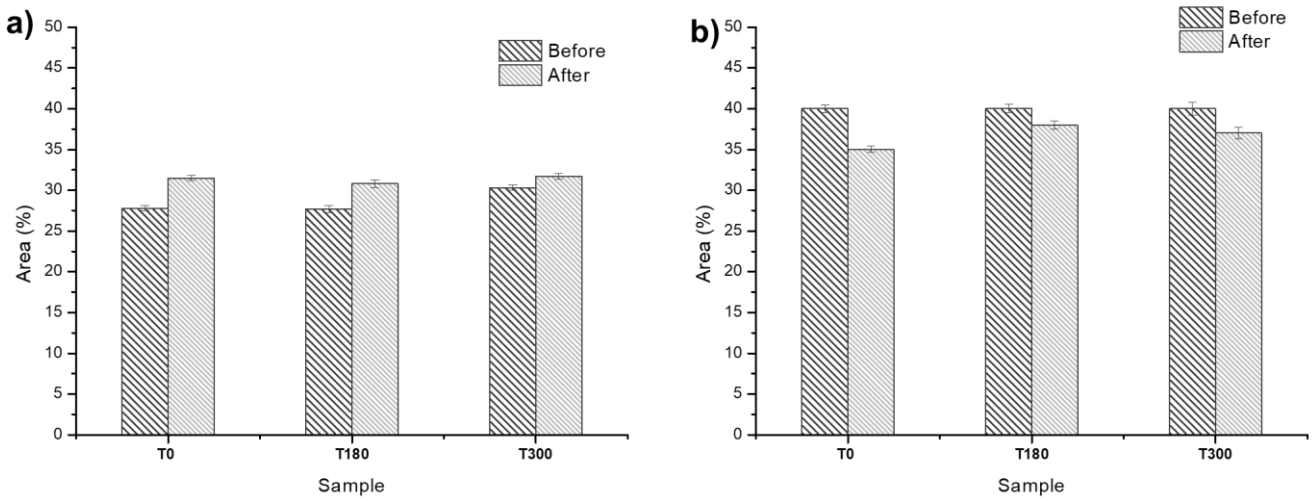

Figure 3. 15: Relative area of a) methylene peak and b) methyl peak at 30 °C before and after *in-situ* vis-breaking

3.3.3 Thermal behaviour and crystallinity

The DSC thermograms in Figure 3. 16 revealed broad melting events for all samples in the absence of peroxide and bimodal melting peaks after vis-breaking. This suggested the formation of two main crystal size distributions. The peak temperature of the higher melting peak in Figure 3. 16b corresponds well with the peak temperature of the untreated polypropylene and copolymers in Figure 3. 16a. The bimodality intimated a phase separation between the highly regular isotactic polypropylene helices and the defective helices formed after vis-breaking. As discussed, the shorter chains have the effect of exacerbating the defects resulting in multiple distributions with differing crystal sizes and thus varying mobilities within the crystalline domains.[41] The disruption in the crystal structure as a result of the insertion of short ethylene sequences would lead to the formation of more small crystals with higher inherent mobility.[42] In the presence of peroxide and heat the diffusion of the peroxide is enhanced within the smaller crystal domains. This implies that the larger crystals (such as those formed in T0 and T300) provide a greater degree of defence against the action of the peroxide. Considering that the effect was also observed for the T0 sample, it was necessary to investigate any changes within the crystalline structure after vis-breaking. The X-ray diffraction patterns of the samples before and after vis-breaking are shown in Figure 3. 17.

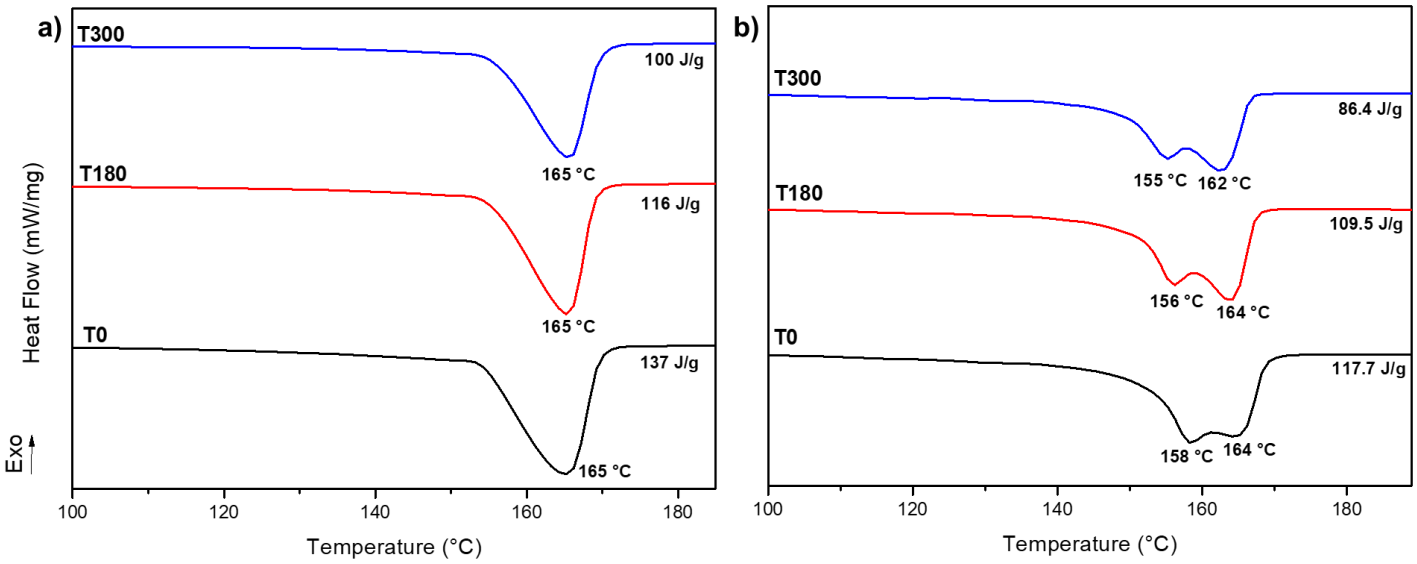

Figure 3. 16: DSC melting thermograms of a) untreated and b) peroxide treated samples after 30 minutes at 190 °C

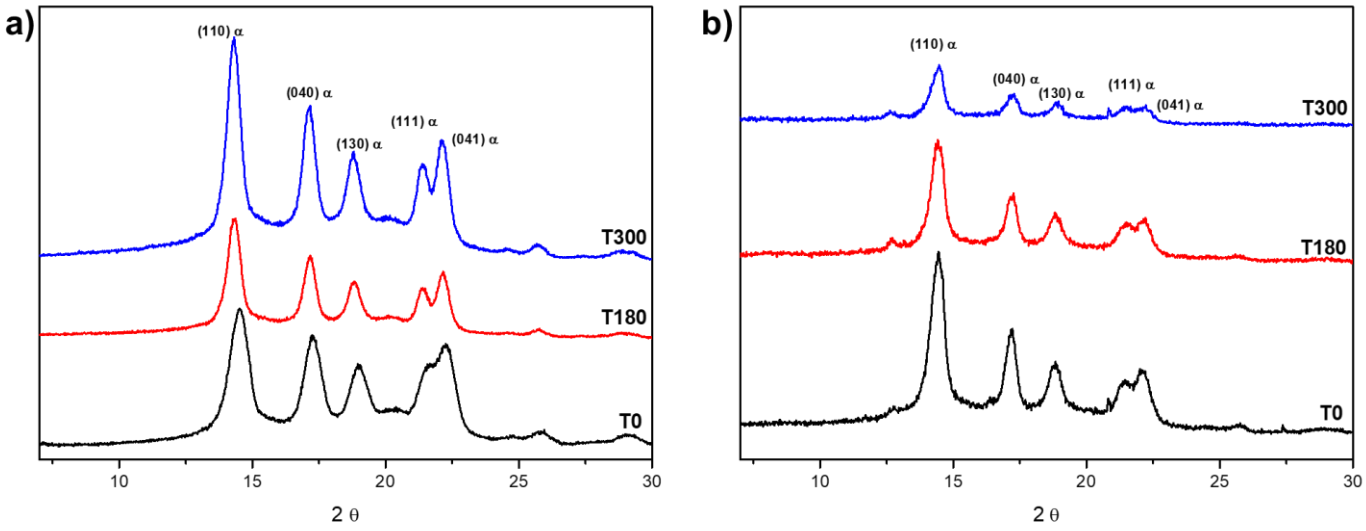

Figure 3. 17: X-ray diffraction patterns for copolymers a) before vis-breaking and b) after *in-situ* vis-breaking

Polypropylene crystals generally have two main crystallographic structures; the α form and the γ form.[37] The α form is the most prevalent crystal structure and can accommodate a certain level of defects in the structure leading to the formation of the disordered phase described above. The X-ray diffraction patterns shown in Figure 3. 17a and b displayed all the peaks characteristic of the α-allomorph.[43] The absence of the peaks at 2θ = 20° which forms

as a result of a combination of α and γ forms[34],[44] was indicative that no γ phase had formed. A comparison of the diffraction patterns before and after *in-situ* vis-breaking showed an overall decrease in crystallinity, specifically in the patterns of the copolymers. The crystallinity of the T300 sample was the most affected as demonstrated in Figure 3. 17b by a significant decrease in intensity as well as a broadening of the peaks. This was evidence of the peroxide causing disorder within the crystalline structure for all of the samples with the increase in disorder being most considerable with increasing ethylene content. It was likely that the chain scission induced by the action of the peroxide resulted in defects which prevent the formation of long-range order within the copolymer matrix.

3.4 Conclusions

The effect of vis-breaking on the chemical structure and morphology of heterophasic ethylene-propylene copolymers with varying ethylene contents was investigated. The vis-breaking of HEPCs was found to be influenced by the homogeneity of the chain sequences. Solution NMR spectroscopy revealed changes in the long chain ethylene sequences for the T300 sample and variations in the sequences containing random ethylene insertions for the T180 sample.

For the first time the use of *in-situ* vis-breaking in solid state NMR spectroscopy could describe the process of vis-breaking in terms of molecular structure and mobility during the molten stage. Each sample experienced changes in the chemical structure due to the vis-breaking reactions, however, the different ethylene contents caused manifestation of these changes in differing fashions. The changes in chemical shifts as well as the splitting of the resonances observed for T180 and T300 respectively both indicated an increase in mobility within crystalline domains to different extents.

The thermal behaviour and crystal structure confirmed the conclusions derived from solid state NMR spectroscopy, that the process of vis-breaking enhances the formation of the disordered phase within isotactic polypropylene as well as impact copolymers. A split in the melting peak of all samples indicated a phase separation of highly ordered crystalline domains and mobile crystal domains incorporating structural defects. The sample with the shortest ethylene sequences (T180) displayed a greater susceptibility to degradation than the sample containing longer ethylene sequences (T300). In all cases the defects incorporated into the structure after vis-breaking disrupted crystallinity.

References

[1] L. Botha, A.J. Van Reenen, The effect of in-process ethylene incorporation on the evolution of particle morphology and molecular characteristics of commercial heterophasic ethylene propylene copolymers (HEPCs), Eur. Polym. J. 49 (2013) 2202–2213. https://doi.org/10.1016/j.eurpolymj.2013.04.020.

[2] M. Gahleitner, C. Tranninger, P. Doshev, Heterophasic copolymers of polypropylene: Development, design principles, and future challenges, J. Appl. Polym. Sci. 130 (2013) 3028–3037. https://doi.org/10.1002/app.39626.

[3] T. Vestberg, M. Parkinson, I. Fonseca, C.-E. Wilén, Poly(propylene-co-ethylene) produced with a conventional and a self-supported Ziegler-Natta catalyst: Effect of ethylene and hydrogen concentration on activity and polymer structure, J. Appl. Polym. Sci. 124 (2011) n/a-n/a. https://doi.org/10.1002/app.35586.

[4] L. Botha, P. Sinha, H. Duveskog, A.J. Van Reenen, The use of solid-state NMR to investigate the development of segmental mobility in commercial heterophasic ethylene propylene copolymers (HEPCs), Macromol. React. Eng. 9 (2015) 313–324. https://doi.org/10.1002/mren.201400043.

[5] J.L. White, Principles of polymer engineering rheology, Wiley, 1990. https://www.wiley.com/en-za/Principles+of+Polymer+Engineering+Rheology-p-9780471853626 (accessed July 30, 2019).

[6] M. Tolinski, Additives for polyolefins : getting the most out of polypropylene, polyethylene and TPO, William Andrew Pub, 2009.

[7] G. Moad, I.J. Dagley, J. Habsuda, C.J. Garvey, G. Li, L. Nichols, G.P. Simon, M.R. Nobile, Aqueous hydrogen peroxide-induced degradation of polyolefins: A greener process for controlled-rheology polypropylene, Polym. Degrad. Stab. 117 (2015) 97–108. https://doi.org/10.1016/j.polymdegradstab.2015.04.001.

[8] A.H. Hogt, J. Meijer, J. Jelenič, Modification of polypropylene by organic peroxides, React. Modif. Polym. (1997) 84–132. https://doi.org/10.1007/978-94-009-1449-0_2.

[9] M. Swart, A.J. Van Reenen, The effect of controlled degradation on the molecular characteristics of heterophasic ethylene-propylene copolymers, J. Appl. Polym. Sci. 132 (2015) 1–10. https://doi.org/10.1002/app.41783.

[10] M.P. Bulsari, C. Tzoganakis, A. Penlidis, Hydrosilylation of impact polypropylene co-polymer in a twin-screw extruder, J. Elastomers Plast. 40 (2008) 365–380. https://doi.org/10.1177/0095244308092422.

[11] J. Kang, B. Wang, H. Peng, J. Chen, Y. Cao, H. Li, F. Yang, M. Xiang, Investigation on the structure and crystallization behavior of controlled-rheology polypropylene with different stereo-defect distribution, Polym. Bull. 71 (2014) 563–579. https://doi.org/10.1007/s00289-013-1077-y.

[12] P.D. Iedema, K. Remerie, M. van der Ham, E. Biemond, J. Tacx, Controlled peroxide-induced degradation of polypropylene in a twin-screw extruder: Change of molecular weight distribution under conditions controlled by micromixing, Chem. Eng. Sci. 66 (2011) 5474–5486. https://doi.org/10.1016/j.ces.2011.06.071.

[13] N.M. Tollefson, Influence of the controlled rheology process (vis-breaking) on additive effectiveness in polypropylene, J. Appl. Polym. Sci. 52 (1994) 905–915. https://doi.org/10.1002/app.1994.070520709.

[14] D. Bertin, M. Leblanc, S.R.A. Marque, D. Siri, Polypropylene degradation: Theoretical and experimental investigations, Polym. Degrad. Stab. 95 (2010) 782–791. https://doi.org/10.1016/j.polymdegradstab.2010.02.006.

[15] H. Azizi, I. Ghasemi, Reactive extrusion of polypropylene : production of controlled-rheology polypropylene (CRPP) by peroxide- promoted degradation, Polym. Test. 23 (2004) 137–143.

https://doi.org/10.1016/S0142-9418(03)00072-2.

[16] W. Zhou, S. Zhu, ESR study on peroxide modification of polypropylene, Ind. Eng. Chem. Res. 36 (1997) 1130–1135. https://doi.org/10.1021/ie960410p.

[17] F. Berzin, B. Vergnes, L. Delamare, Rheological behavior of controlled-rheology polypropylenes obtained by peroxide-promoted degradation during extrusion : Comparison between homopolymer and copolymer, J. Appl. Polym. Sci. 80 (2001) 1243–1252.

[18] F.M.B. Coutinho, T.H.S. Costa, Controlled degradation of polypropylene in solution by organic peroxides, Polym. Test. 13 (1994) 363–366. https://doi.org/10.1016/0142-9418(94)90006-X.

[19] R. Cordova, R.T. Kamierczak, L. Kasehagen, T.N. Myers, Polypropylene modification using organic peroxide, EP1223178A1, 2002. https://patents.google.com/patent/EP1223178A1/en (accessed September 30, 2019).

[20] I. Krupa, A.S. Luyt, Cross-linking of LDPE/wax blends in the presence of dicumyl peroxide, South African J. Chem. 55 (2002) 34–42.

[21] E. Borsig, A. Fiedlerová, M. Lazár, Efficiency of chemical cross-linking of polypropylene, J. Macromol. Sci. Part A - Chem. 16 (1981) 513–528. https://doi.org/10.1080/00222338108058488.

[22] G.R. Rideal, J.C. Padget, The thermal-mechanical degradation of high density polyethylene, J. Polym. Sci. Polym. Symp. 57 (2007) 1–15. https://doi.org/10.1002/polc.5070570103.

[23] C.J. Carman, C.E. Wilkes, Monomer sequence distribution in ethylene propylene elastomers. I. Measurement by carbon-13 Nuclear Magnetic Resonance spectroscopy, Rubber Chem. Technol. 44 (1971) 781–804. https://doi.org/10.5254/1.3544794.

[24] V. Busico, R. Cipullo, G. Monaco, M. Vacatello, A.L. Segre, Full assignment of the 13C NMR spectra of regioregular polypropylenes: methyl and methylene region, Macromolecules. 30 (1997) 6251–6263.

[25] V. Busico, R. Cipullo, G. Monaco, M. Vacatello, J. Bella, A.L. Segre, Full Assignment of the 13 C NMR Spectra of Regioregular Polypropylenes: Methine Region , Macromolecules. 31 (2002) 8713–8719. https://doi.org/10.1021/ma981040e.

[26] L. Botha, The effect of in-process ethylene incorporation on the evolution of particle morphology and molecular characteristics of commercial heterophasic ethylene propylene copolymers (HEPCs), Stellenbosch University, 2014.

[27] F.L. Binsbergen, B.G.M. de Lange, Morphology of polypropylene crystallized from the melt, Polymer (Guildf). 9 (1968) 23–40. https://doi.org/10.1016/0032-3861(68)90006-2.

[28] N.J. Terrill, P.A. Fairclough, E. Towns-Andrews, B.U. Komanschek, R.J. Young, A.J. Ryan, Density fluctuations: The nucleation event in isotactic polypropylene crystallization, Polymer (Guildf). 39 (1998) 2381–2385. https://doi.org/10.1016/S0032-3861(97)00547-8.

[29] A.E. Tonelli, M.A. Gomez, H. Tanaka, M.H. Cozine, Solid state 13C NMR studies of the structures, conformations, and dynamics of semi-crystalline polymers, in: Solid State NMR Polym., Springer US, Boston, MA, 1991: pp. 81–105. https://doi.org/10.1007/978-1-4899-2474-2_4.

[30] K. Klimke, M. Parkinson, C. Piel, W. Kaminsky, H.W. Spiess, M. Wilhelm, Optimisation and application of polyolefin branch quantification by melt-state 13C NMR spectroscopy, Macromol. Chem. Phys. 207 (2006) 382–395. https://doi.org/10.1002/macp.200500422.

[31] W. Hu, H. Hagihara, T. Miyoshi, Microstructural analysis of insoluble polyolefins by melt-state 13C NMR at very high temperatures, Macromolecules. 40 (2007) 3505–3509. https://doi.org/10.1021/ma070377q.

[32] K. Klimke, Optimised polyolefin branch quantification by 13C NMR spectroscopy, Johannes Gutenberg University Mainz, 2006.

[33] L. Reich, S.S. Stivala, Elements of Polymer Degradation, McGraw-Hill, 1971.

[34] L. Botha, P. Sinha, S. Joubert, H. Duveskog, A.J. Van Reenen, Solution and solid-state NMR characterization of heterophasic propylene-ethylene copolymers (HEPC) with increasing ethylene content, Eur. Polym. J. 59 (2014) 94–104. https://doi.org/10.1016/j.eurpolymj.2014.07.010.

[35] A. Fernández, M.T. Expósito, B. Peña, R. Berger, J. Shu, R. Graf, H.W. Spiess, R.A. García-Muñoz, Molecular structure and local dynamic in impact polypropylene copolymers studied by preparative TREF, solid state NMR spectroscopy, and SFM microscopy, Polymer (Guildf). 61 (2015) 87–98. https://doi.org/10.1016/j.polymer.2015.01.079.

[36] M.S. Sevegney, G. Parthasarthy, R.M. Kannan, D.W. Thurman, L. Fernandez-Ballester, Deformation-induced morphology changes and orientation behavior in syndiotactic polypropylene, Macromolecules. 36 (2003) 6472–6483. https://doi.org/10.1021/ma025774+.

[37] D.L. VanderHart, R.G. Alamo, M.R. Nyden, M.H. Kim, L. Mandelkern, Observation of resonances associated with stereo and regio defects in the crystalline regions of isotactic polypropylene: toward a determination of morphological partitioning, Macromolecules. 33 (2000) 6078–6093. https://doi.org/10.1021/ma992041p.

[38] O. Fričová, M. Uhrínová, V. Hronský, M. Koval'aková, D. Olčák, I. Chodák, J. Spěváček, High-resolution solid-state NMR study of isotactic polypropylenes, Express Polym. Lett. 6 (2012) 204–212. https://doi.org/10.3144/expresspolymlett.2012.23.

[39] V. Agarwal, T.B. Van Erp, L. Balzano, M. Gahleitner, M. Parkinson, L.E. Govaert, V. Litvinov, A.P.M. Kentgens, The chemical structure of the amorphous phase of propylene-ethylene random copolymers in relation to their stress-strain properties, Polymer (Guildf). 55 (2014) 896–905. https://doi.org/10.1016/j.polymer.2013.12.051.

[40] G. Metz, M. Ziliox, S.O. Smith, Towards quantitative CP-MAS NMR, Solid State Nucl. Magn. Reson. 7 (1996) 155–160. https://doi.org/10.1016/S0926-2040(96)01257-X.

[41] M. Cocca, R. Androsch, M.C. Righetti, M. Malinconico, M.L. Di Lorenzo, Conformationally disordered crystals and their influence on material properties: The cases of isotactic polypropylene, isotactic poly(1-butene), and poly(l-lactic acid), J. Mol. Struct. 1078 (2014) 114–132. https://doi.org/10.1016/j.molstruc.2014.02.038.

[42] D. Mileva, R. Androsch, D. Cavallo, G.C. Alfonso, Structure formation of random isotactic copolymers of propylene and 1-hexene or 1-octene at rapid cooling, Eur. Polym. J. 48 (2012) 1082–1092. https://doi.org/10.1016/j.eurpolymj.2012.03.009.

[43] C. De Rosa, F. Auriemma, O.R. De Ballesteros, L. Resconi, I. Camurati, Tailoring the physical properties of isotactic polypropylene through incorporation of comonomers and the precise control of stereo-and regioregularity by metallocene catalysts, Chem. Mater. 19 (2007) 5122–5130. https://doi.org/10.1021/cm071502f.

[44] C. De Rosa, F. Auriemma, O.R. De Ballesteros, L. Resconi, I. Camurati, Crystallization behavior of isotactic propylene-ethylene and propylene-butene copolymers: Effect of comonomers versus stereodefects on crystallization properties of isotactic polypropylene, Macromolecules. 40 (2007) 6600–6616. https://doi.org/10.1021/ma070409+.

Impact copolymers for polypropylene-based hot-melt adhesives

4.1 Introduction

An adhesive is any material which binds two surfaces in a way that resists separation.[1] Prior to the advent of commercial adhesive bonding, the most popular joining method was mechanical binding such as welding, sewing or the use of mechanical fasteners. Adhesive bonding has numerous advantages over mechanical bonding methods, the most important of which is the distribution of stress over wider areas.[2] In mechanical bonding the stress is limited to the area of the fastener or welded region. Thus, lighter fabrications with greater strength can be produced using adhesives. In addition, the use of adhesives allows for the joining of different types of materials and is generally faster and more affordable than mechanical bonding.[2]

Adhesives can be classified according to multiple categories such as the method of application, the chemical composition, suitability for different surfaces as well as the origin of the components. One of the most important classifications is the mode of application. In order to effectively facilitate binding between two surfaces the adhesive should be applied in the fluid state and both surfaces should be completely coated without voids. For this reason the viscosity of the adhesive should be low at the time of application. Subsequently, the development of cohesion between layers requires the adhesive to set yielding a liquid to solid transition which can be achieved by the following methods:

First, by the cooling of thermoplastic polymers which become fluid in the molten state and harden again once cooled. The adhesive can be applied in many forms such as hot-melts, extrudates, powders or in a solvent followed by drying. Hot-melts, extrudates and powders form cohesive bonds immediately after application, making them more popular than solvent based adhesives which require increased waiting times for solvent evaporation.

Second, the release of a solvent or carrier liquid can cause solidification of solutions and latexes. In cases where both the adhered surfaces are impermeable, the solvent or carrier needs to be evaporated before the two surfaces can be joined. This process is time-consuming and greatly reduces the popularity of these types of adhesives. Third, in-situ polymerisation of adhesive components to form cross-linked interlayers has gained attention due to vulcanisation processes of elastomers which increase cohesion in rubbers. Certain monomers such as methacrylates and cyanoacrylate esters[3] readily polymerise in-situ and can be easily applied using this method.[4] Compared to solvent-based methods, in-situ polymerisation is preferred as the cohesive strength is achieved after the joining of the surfaces leading to faster

production times. Finally, pressure-sensitive adhesives do not follow the same transitions as the previous three methods of application. Instead of a gradual increase in the viscosity, pressure-sensitive adhesives remain in a perpetually tacky state. This prevents efficient wetting of the surfaces intentionally so that the adhesive can be easily removed without tarnishing the adhered surfaces. Unfortunately, this also results in low cohesion within the adhesive.

Commercially, hot-melts have the widest applicability due to their rapid setting time and ease of automation.[2] Hot-melts can also accommodate a wide range of formulations, allowing them to be adjusted to the costs and performance requirements of the application. The strength of a hot-melt adhesive (HMA) is determined by two factors; polarity and molecular weight. For example, both paraffin waxes and polyethylenes are used in HMAs as hydrocarbon materials, but the higher molecular weight polyethylene has greater tear strength and thermal stability.

A typical HMA formulation is comprised of three components; a polymer (in the range of 30 – 40 %), a tackifying agent (usually in similar ratio to the polymer) and a wax (approximately 20 – 30 %).[5] Precise quantities and relative ratios of each component depend on the required properties of the adhesive. The core of the HMA is the polymer which imparts the toughness of the adhesive. As per its name, the tackifier increases the tackiness of the adhesive and aids in the wetting of the surface. This role is also played by the wax which achieves surface wetting by decreasing the viscosity of the melt and regulating the setting rate.[6] Of the polymers used in HMAs, ethylene-vinyl acetate copolymers (EVAs) were most favoured as they can be easily included in a variety of formulations and exhibits enhanced adhesion to multiple types of substrates. EVA based HMAs are commonly used for bookbinding and binding the edges of furniture parts. Polyamides and polyesters find applicability in the soling of shoes and the side-seams of cans as they typically have higher softening points and adhesive strength.[7],[8] Cardboard cartons and boxes with corrugated inners usually contain polyethylene based HMAs.[9] During the 1960s atactic polypropylene was a common by-product in the production of isotactic polypropylene making it an affordable component for adhesives. Atactic polypropylenes have inherent tack and do not require high quantities of tackifier or wax.[10],[11] The advent of more effective catalysts has, however, decreased the availability of atactic polypropylene unless intentionally produced, leading to a decrease in its use in HMAs. Nevertheless, polyolefins remain a desirable base of HMAs due to their high molecular weight and the ability to introduce comonomers which vary the properties of the polymer for specific applications.[2] The role of the tackifying resin is to enhance the adhesion between the polymer and the adherents. The tackifier reduces the viscosity of the HMA thereby facilitating sufficient wetting of the surface. Tackifiers are generally classified by their composition and are derived from three chemical classes; hydrocarbons, rosin esters and polyterpenes.[12] Waxes are

included in HMAs to decrease the melt viscosity and to reduce the cost of the formulation. The wax also affects the blocking ability, softening point and open time of the HMA.[6] Higher melting microcrystalline or synthetic waxes add high heat stability while paraffin waxes impart antiblocking and barrier properties.[2]

As mentioned, atactic polypropylenes (APPs) could essentially be used as a neat material for adhesion. While production of APPs has decreased, impact copolymers have increased in production since their introduction in the 1970s. These impact copolymers, technically termed heterophasic ethylene-propylene copolymers (HEPCs), combine an isotactic polypropylene matrix with ethylene-propylene rubber and polyethylene homopolymer embedded in the matrix in a gradient fashion.[13] In this study the efficacy of HEPCs as the polymer base for polypropylene-based hot-melt adhesives is investigated in terms of the melt-state and solid-state interactions between the polymer and various wax types.

4.2 Materials and Methods

4.2.1 Materials

Both the isotactic polypropylene (iPP) and the HEPC were obtained from Sasol Polymers. The iPP is characterised by an MFI of 12 g/10 min. The HEPC was sampled directly from the sequential gas-phase reactor process 360 minutes after ethylene introduction into the second reactor.

Three commercial waxes were used in this study from three different wax categories. These were a linear paraffin with a melting point of 64 °C and kinematic viscosity of 5.2 mm^2/s at 100 °C, a branched paraffin with a melting point of 71 °C and kinematic viscosity of 7.5 mm^2/s at 100 °C both from ExxonMobil. Additionally, a high-melting Fischer-Tropsch (FT) wax from Sasolwax was used with drop melting point 112 °C and viscosity of 8 cP at 135 °C.

4.2.2 Polymer/wax blend preparation

Solution blends of a high ethylene content impact copolymer with three types of waxes were prepared in *o*-dichlorobenzene. A total of 2 g of sample was dissolved in 30 mL solvent for one hour to ensure intimate mixing. Blends were then placed in glass petri dishes and dried in an oven at 40 °C for 48 hours. The waxes fall into the categories of linear Fischer-Tropsch (FT), linear paraffin and branched paraffin. Blends were prepared in 10 wt% and 30 wt% wax ratios. As a control sample for accurate NMR spectra interpretation, blends of the same ratios were also prepared for isotactic polypropylene as a zero-ethylene content reference.

4.2.3 HMA preparation

HMA formulations were prepared by combining the above polymer/wax blends with Eastotac™ H-130R tackifying agent (Eastman, United States). The mass of tackifier was equal to the mass of polymer added to maintain the ratio of 40:40:20 for 30 % wax blends and 45:45:5 for 10 % wax blends. Irganox 1010 (Sigma-Aldrich) heat stabiliser was added to 0.5 wt% of the total mass of the formulation. Glass vials containing the formulations were placed in an oil bath at 190 °C and an overhead mixer stirring at 150 rpm was used to ensure adequate mixing.

4.2.4 Solid-state NMR spectroscopy

Solid-state NMR spectra were acquired on a Varian VNMRS 500 MHz NMR spectrometer with 4 mm Chemagnetics™ HX T3 MAS probe and zirconia rotors. Magic angle spinning (MAS) was performed at 5 kHz using adamantane as external chemical shift standard referencing the downfield peak to 38.3 ppm. Single pulse spectra were acquired at 190 °C and 160 °C using a 90° pulse of 2.25 ms with recycle delay of 5s, acquisition time of 30 ms and 128 scans. ^{13}C cross-polarisation (CP) spectra were recorded at 190 °C, 160 °C, 130 °C, 100 °C, 60 °C and 30 °C. All ^{13}C CP spectra were proton decoupled by the two-pulse phase modulated (TPPM) decoupling sequence with a 2.25 µs 90° pulse with a recycle delay of 5 seconds. CP contact time was 1 ms and acquisition time was 30 ms with 100 scans. Variable contact time experiments were performed at 30 °C using the same CP method above with contact time arrayed in values of 0.5 ms, 1 ms, 3 ms and 5 ms. For interrupted decoupling experiments an 8 µs 180° pulse with a recycle delay of 5 seconds was used. The time constant for interrupted decoupling was set to 20 µs and 200 scans were acquired. Nitrogen gas was used for variable temperature pneumatics.

4.2.5 Differential Scanning Calorimetry (DSC)

DSC thermograms were acquired using a Netzsch DSC Polyma 214 calorimeter. All sample masses were between 5 – 6 mg. Temperature calibrations were performed using indium standards. For standard DSC curves samples were heated to 200 °C followed by a cooling cycle to 0 °C and subsequently re-heated to 200 °C. The heating rate was maintained at 10 °C/min. Melting points and enthalpies were determined from the second heating thermogram.

Non-isothermal kinetics were performed on the HMA samples weighing between 4 – 5 mg per sample. HMA samples were heated to 200 °C at a rate of 10 K/min, maintained isothermally for 5 minutes then cooled at 20 and 10 K/minute with a re-heating cycle between each cooling cycle. Baseline correction was performed on the crystallization exotherms followed by integration at various temperature steps using the Origin 8.5 Pro software. Integrated area as

a function of temperature was plotted to yield the crystallization rate plots for each cooling rate.

4.2.6 Confocal microscopy (CLSM)

CLSM micrographs were acquired using an LSM780 confocal microscope (Zeiss, Germany) with ZEN 2012 software. Images were obtained using the EC Plan-Neofluar 10x/ 0.3 M27 and LD Plan-Neofluar 40x/ 0.6 Corr M27 objectives. Excitation was performed with a 514 nm Argon multi-line laser and emission was detected in the range 539 – 753 nm. Laser power, gain and pinhole size were optimised for the most suitable signal intensity.

4.2.7 Tensile testing

Bond strength measurements were performed on an Instron 4444/ H1028 tensile tester. The clamp distance was set to 265 mm. Samples were prepared by dispensing HMAs onto cardboard bands measuring 19.8 cm x 3 cm. A constant adhesive mass of 250 mg was used for each sample. The area of overlap between cardboard substrates was maintained at 2.5 cm x 3 cm.

4.3 Results and Discussion

4.3.1 Characterisation of polymer/wax blends

In the DSC thermograms of the 10% wax blends in Figure 4. 1 and Figure 4. 3 small peaks were visible at lower temperatures due to the individual melting and crystallisation of the paraffin waxes. In contrast the melting and crystallisation of the FT wax were not clearly identifiable suggesting strong interactions with the polypropylene. The nature of this interaction is not yet clear. It appeared that the isotactic polypropylene peak crystallisation temperature was shifted to successively lower temperatures for FT, linear paraffin and branched paraffin wax blends respectively in Figure 4. 3. Correspondingly, from the enthalpy associated with the crystallisation of the polypropylene in the blends in Table 4. 1, the enthalpy of crystallisation decreased relative to neat iPP with the linear paraffin blend having the least impact and the FT blend having the greatest impact. In contrast, the paraffin waxes increased the crystallisation enthalpy of the HEPC component, with the linear paraffin blend showing the greatest increase while the FT wax decreased the crystallisation enthalpy relative to the neat HEPC. This suggested that the nature of the interaction between the polypropylene and the FT wax was an interference in crystallisation. The exact details of this interaction cannot be determined by DSC alone and solid-state NMR spectroscopy would be needed to clarify the type of interactions.

Figure 4. 2 and Figure 4. 4 display the DSC thermograms of the 30% wax blends. As expected, wax presence becomes more obvious at 30 wt% composition. Melting profiles of high-melting

FT waxes typically contain a double peak shape, however, even when the wax crystallises individually as in Figures 4.2 and 4.4 this profile was not observed. Combined with the shifting of the HEPC peak to overlap the crystallisation region of the FT wax, confirmed the suggestion of crystallisation interference which was found to be more dramatic by the increased wax concentration. For both the HEPC and iPP the presence of large quantities of wax shifted the peak crystallisation to lower temperatures. From Table 4. 1 the crystallisation enthalpies of the iPP followed the same trends as in the case of the 10% blends, however, the values are significantly lower. For the HEPC crystallisation enthalpy when blended with 30% paraffin wax returned to neat HEPC levels with similar values for both paraffin waxes. This suggested that at high paraffin contents the wax and HEPC behave independently of each other. A value could not be obtained for the isolated polypropylene crystallisation at 30% FT wax as the crystallisation events of the two components overlapped.

Both DSC thermograms of iPP and HEPC show similar trends irrespective of the absolute values of the crystallisation enthalpies. To summarise, the linear paraffin displayed the most favourable interactions, followed by the branched paraffin and the FT wax. Therefore, the observations are not unique to HEPC or due to the presence of the ethylene within the HEPC. This can be explained by the crystallisation rate of the different waxes. There appears to be an optimum rate for compatibility in these blends. The literature on EVA-based HMAs has reported that the nature of the wax is known to affect the compatibility of the HMA which in turn affects the adhesive properties. Previous studies have reported that FT waxes tend to reduce compatibility as a result of its rapid crystallisation at higher temperatures while paraffin waxes enhance compatibility due to the presence of a greater branching distribution which slows the rate of crystallisation.[14] It seems that the FT wax rate is too rapid while the branched paraffin rate may be too slow for compatibility with these specific polypropylenes.

Theoretically, co-crystallinity of polypropylene with wax is not possible due to the crystallisation of polypropylene into helical structures whereas the FT wax crystallises in a planar zig-zag conformation to form orthorhombic crystal structures.[15] Therefore the PP and wax are only homogeneous at a macroscopic level and the disappearance of the wax signal is more likely due to a decrease in overall crystallinity preventing both components from crystallising. For both HEPC and iPP the presence of the wax appears to narrow the width of the crystallisation peak indicating a more homogeneous crystalline distribution.

Table 4. 1: Crystallisation enthalpies of polypropylene peaks in DSC thermograms

	ΔH iPP (J/g)		ΔH HEPC (J/g)	
Wax Type	**10 %**	**30 %**	**10 %**	**30%**
-	117		60	
Linear Paraffin	109	83	90	58
Branched Paraffin	79	69	78	57
Fischer-Tropsch	73	68	30	-*

*polypropylene and wax signal merged

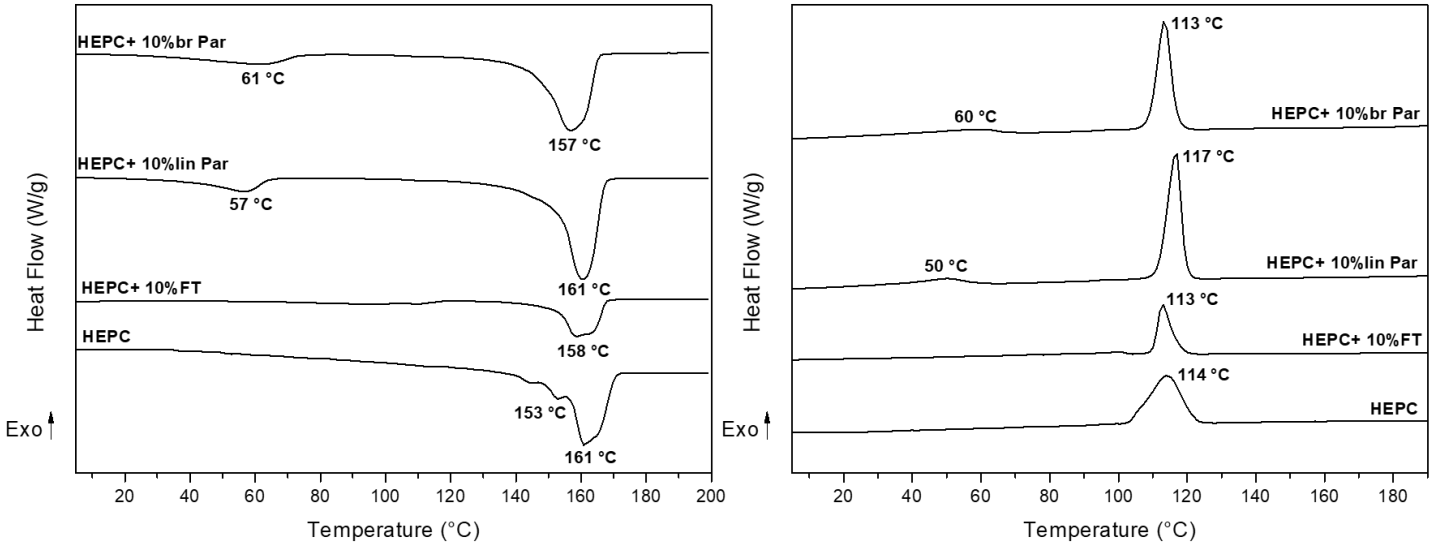

Figure 4. 1: DSC thermograms of HEPC 10% wax blends

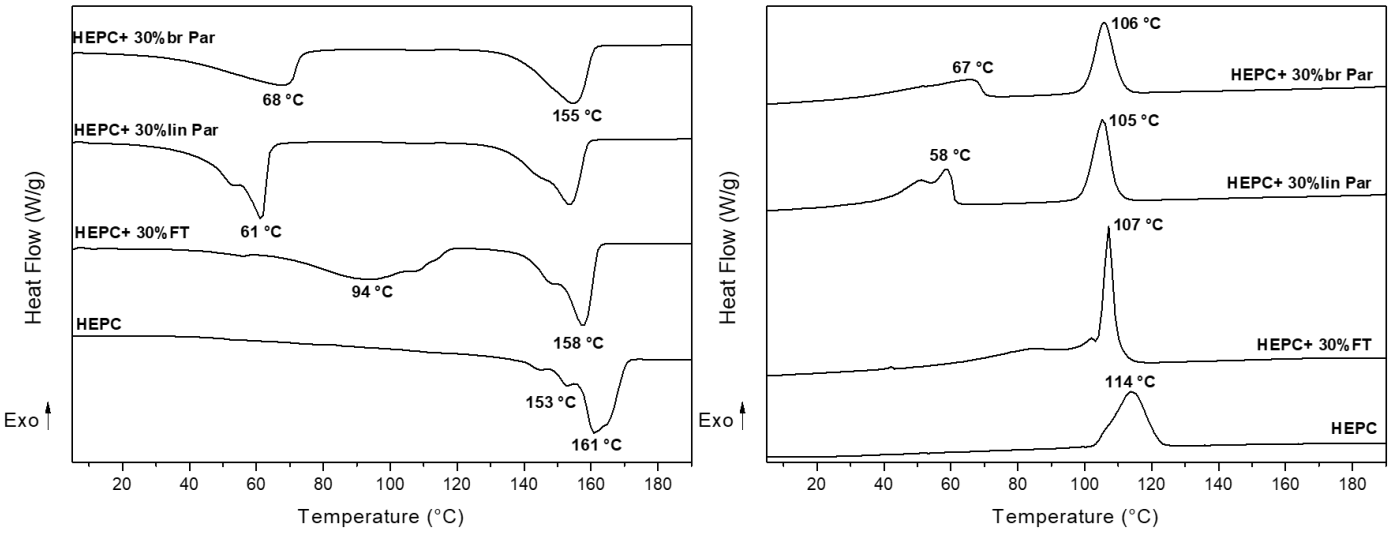

Figure 4. 2: DSC thermograms of HEPC 30% wax blends

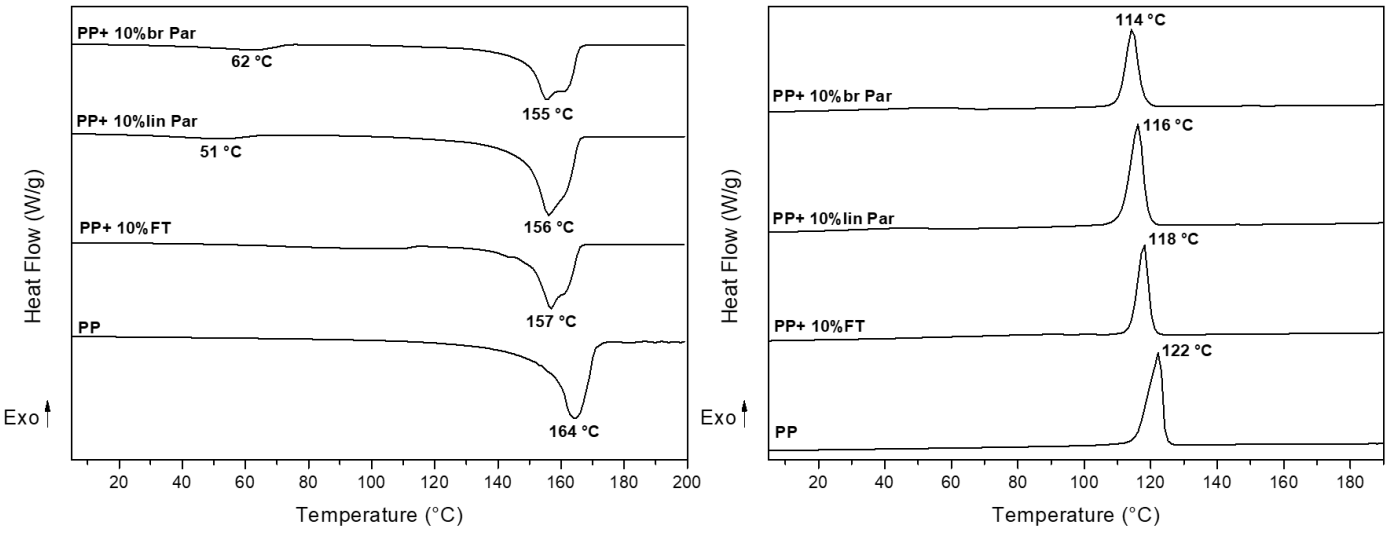

Figure 4. 3: DSC thermograms of isotactic polypropylene 10% wax blends

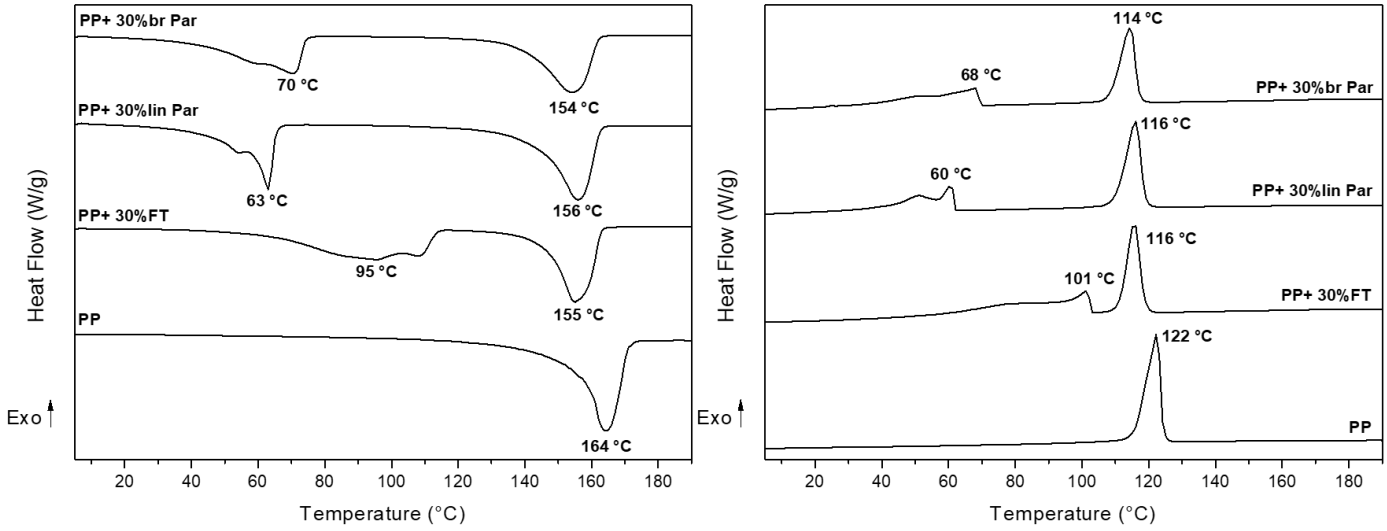

Figure 4. 4: DSC thermograms of isotactic polypropylene 30% wax blends

The X-ray diffractograms in Figure 4. 5 indicated that only the α-form of polypropylene was present in the iPP, however, the HEPC displayed a small peak at 2θ = 20° indicating a low contribution of γ-phase in the HEPC crystal structure.[16] The main peaks for the orthorhombic crystal structure of the wax were observed upon addition of wax. The crystal structure and ratio between the different reflections appeared constant for iPP. The only observable change is the addition of the large peak at 2θ=21.6 due to the orthorhombic crystalline domains of the wax. The HEPC, in contrast, displayed an increase in the intensity of the (130) reflection as well as the disappearance of the peak at 2θ = 20° which indicated that the wax promoted the crystallisation of the α-form in the HEPC. Since the α-form is favoured during rapid

crystallisation[17] even for high comonomer contents, the X-ray diffractograms prove that the wax increases the crystallisation rate of the HEPC.

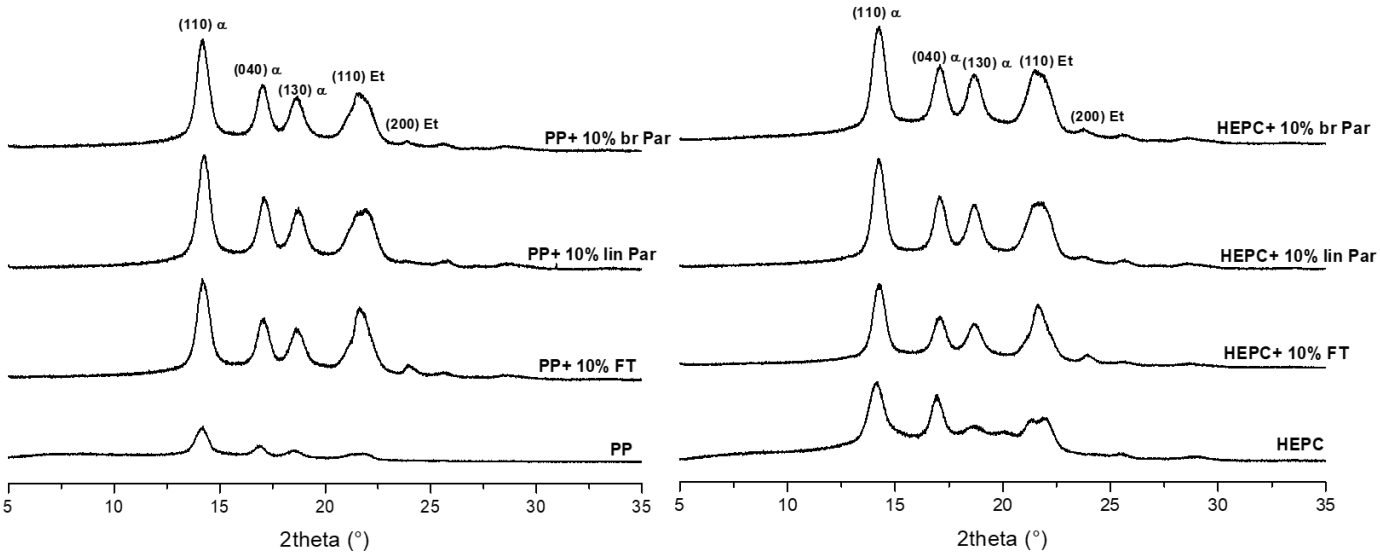

Figure 4. 5 X-ray diffractograms of iPP and HEPC 10% wax blends

The variable temperature (VT) ^{13}C CP/MAS spectra depicted in the following sections were obtained during cooling after maintaining the sample at 190 °C for 5 minutes. The spectra of the neat iPP and HEPC in Figure 4. 6 display the three characteristic peaks of polypropylene at 44 ppm, 26 ppm and 21 ppm for methylene, methine and methyl carbons respectively. The iPP and HEPC have similar CP/MAS spectra with the exception of small peaks in the 30 – 34 ppm region of the HEPC spectrum due to the presence of crystalline and amorphous ethylene regions in the copolymer. The isotactic polypropylene spectrum at 160 °C displays low intensity peaks indicating that some of the polypropylene is beginning to crystallise and become rigid allowing it to be visible in the CP/MAS spectrum. Since the DSC indicated that the isotactic PP's onset of crystallisation occurs before that of the HEPC this was expected. The shoulders observed in the methylene and methine peaks at above 100 °C is due to the increased amorphous polypropylene component in the molten state, resulting in small peaks to the left of the main methylene and methine peaks.[18] Below 100 °C a splitting of the methylene and methyl signals occurs due to the overlap of multiple resonances arising from the ordered and disordered crystal packing forms of the α crystal structure.

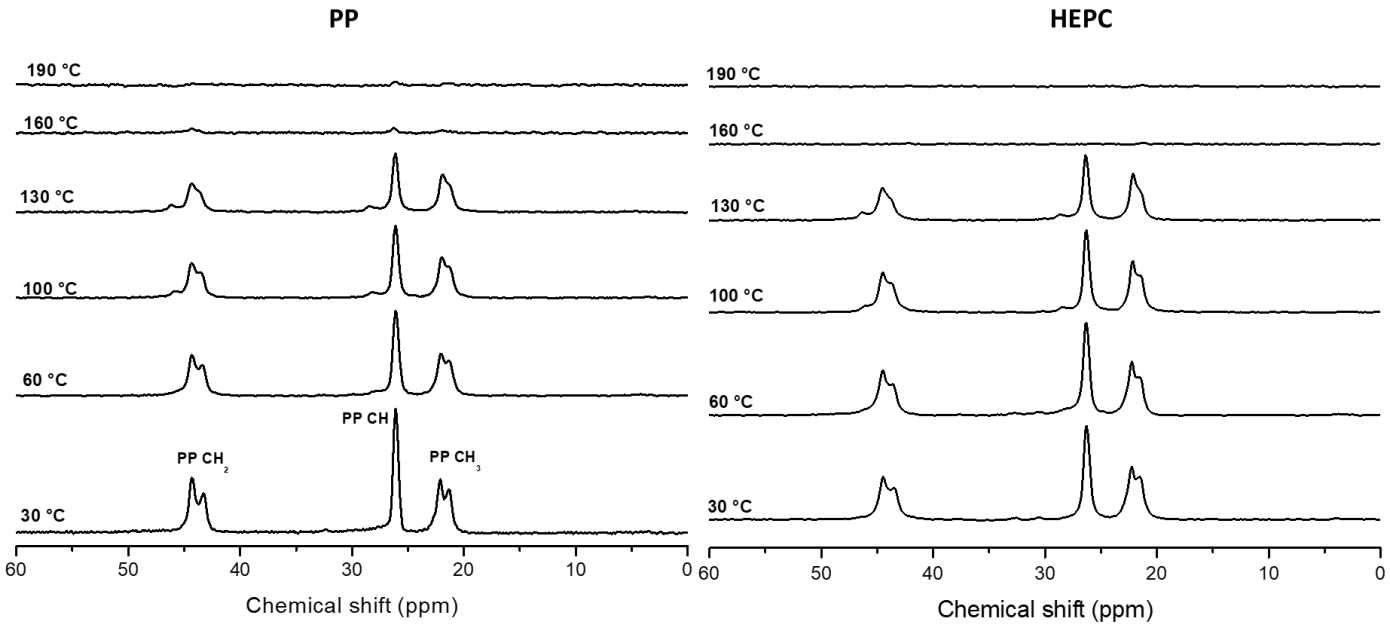

Figure 4. 6: VT CP/MAS spectra of isotactic polypropylene and impact copolymer

The VT ^{13}C CP/MAS spectra of the 10% wax blends in Figure 4. 7 and Figure 4. 8 show that, in all cases, the presence of the wax caused an earlier onset of crystallisation compared to the intensities observed in the neat polypropylene spectra at 160 °C (Figure 4. 6). This effect was most noticeable for the linear paraffin for the iPP, however, the HEPC experienced a greater extent of intensity enhancement at 160 °C with the linear paraffin and FT wax yielding similar effects. This suggests that while crystallisation is enhanced for both polypropylenes, the HEPC is more favourably affected by the presence of wax than the iPP. This is due to the presence of the ethylene sequences within the HEPC which can associate with the wax. The FT wax blend in Figure 4.8c possessed the most intense crystalline ethylene peak indicating that the FT wax either crystallised individually or promoted crystallisation of the ethylene component of the HEPC. Since the DSC results do not show independent crystallisation of FT wax it is likely that the FT wax promoted polyethylene domain crystallisation in the HEPC. This is not a new phenomenon as it has previously been reported that waxes can enhance crystallisation of various types of polyethylene[19] through co-crystallisation[20] and that full miscibility to partial miscibility can be achieved between polyethylene/ wax blends between 10 – 30% wax.[21]

As previously explained, the splitting observed in the methylene and methyl resonances is due to an overlap of three signals; an upper and lower peak resulting from the ordered α-form as well as a central peak arising from the disordered α-form.[18] [22] In the absence of the disordered phase, the splitting would occur in a 2:1 ratio, however, the presence of the disordered phase changes the line shape to appear as two merged signals of almost equal

ratio. From Figure 4. 6 the splitting is clearly defined for iPP but less so for the HEPC suggesting increased quantities of disordered phase in the HEPC. In the spectra in Figure 4. 7 the methyl resonance for the branched paraffin blend and the FT blend with iPP displays splitting in almost equal ratios, signifying an increase in the disordered phase within these blends. The methyl resonance in the spectrum in Figure 4. 8c also displayed a similar increase in the disordered phase for the HEPC/FT blend.

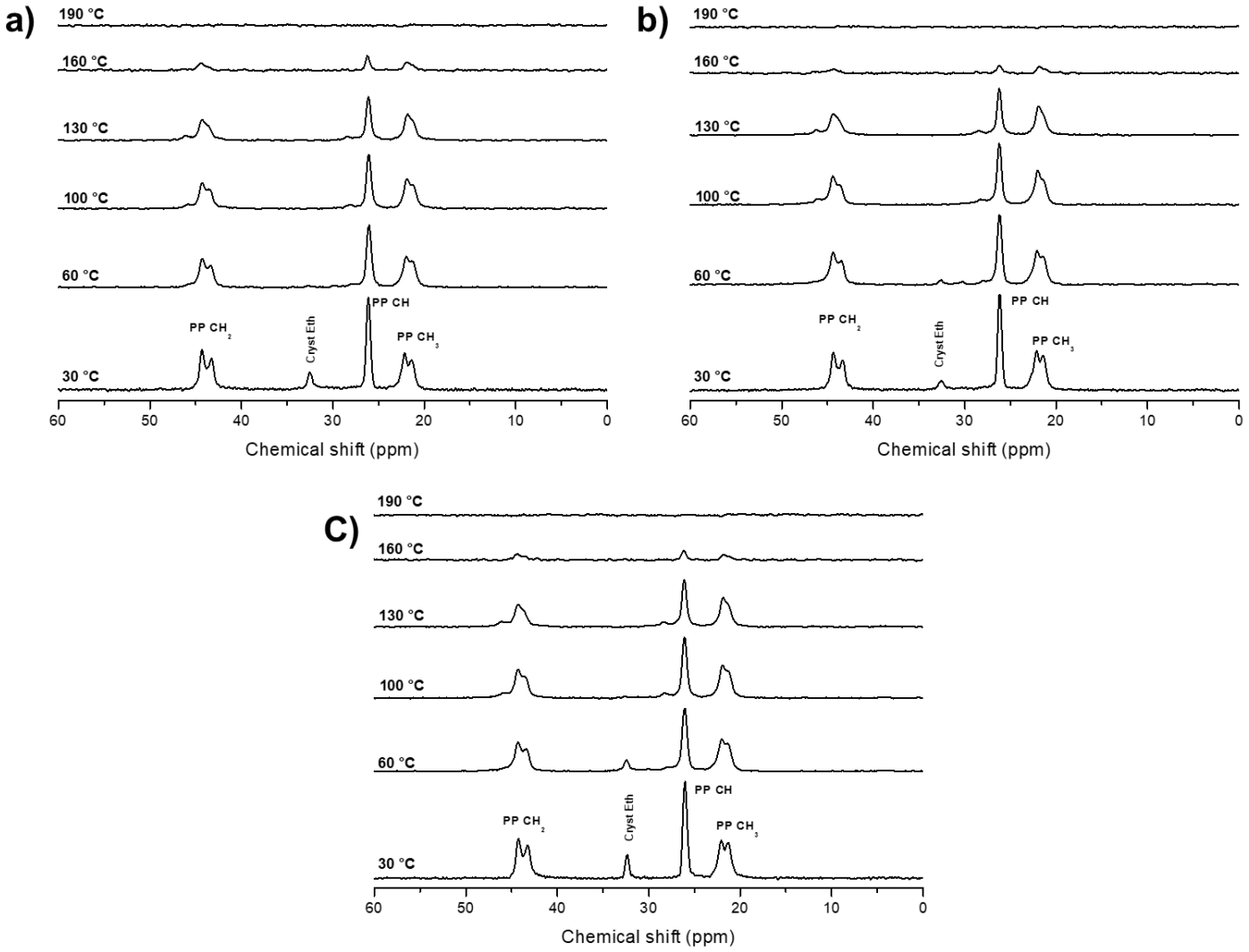

Figure 4. 7: VT CP/MAS spectra of a) PP + 10% linear paraffin b) PP + 10% branched paraffin and c) PP + 10% FT

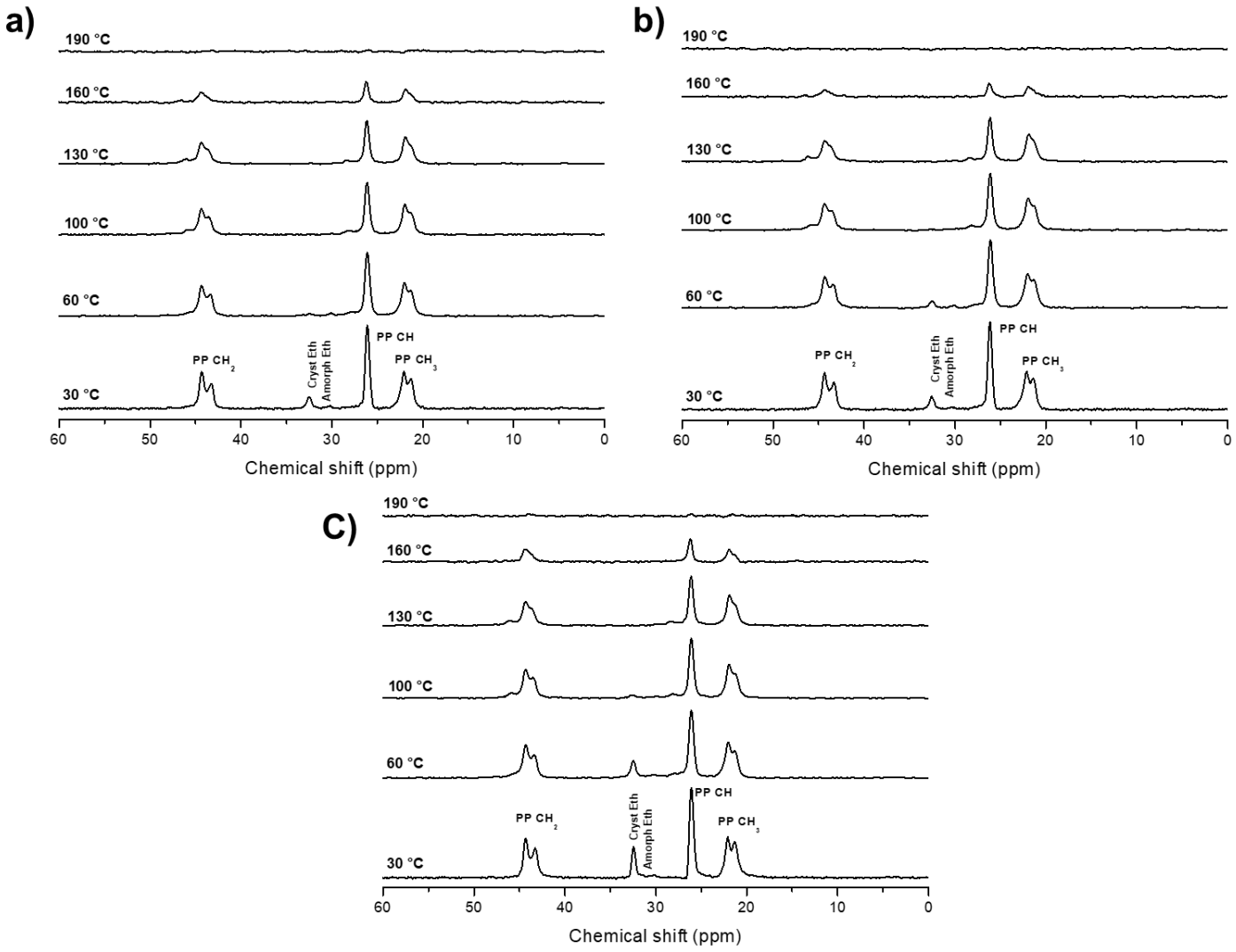

Figure 4. 8 VT CP/MAS spectra of a) HEPC + 10% linear paraffin b) HEPC + 10% branched paraffin and c) HEPC + 10% FT

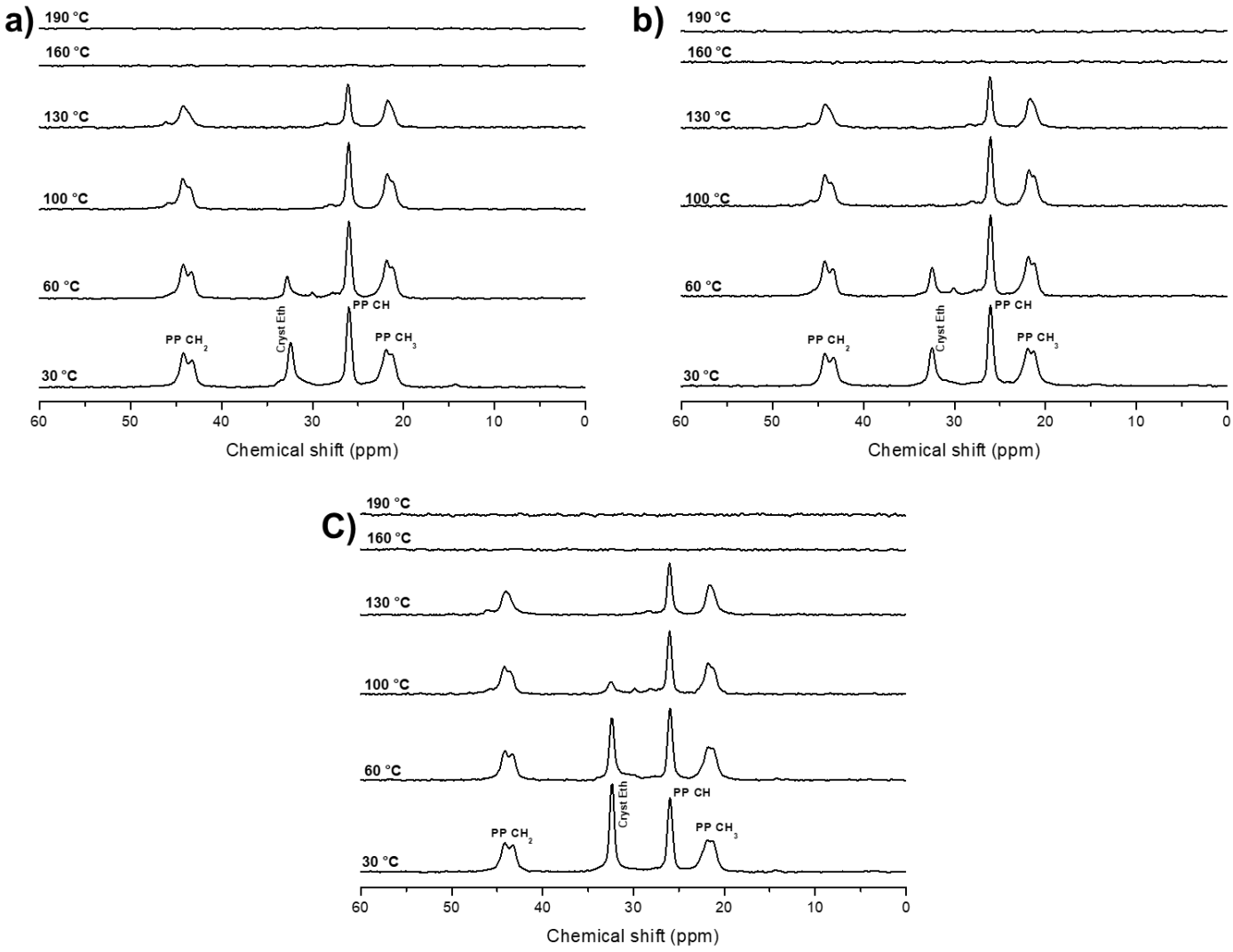

Figure 4. 9: VT CP/MAS spectra of a) PP + 30% linear paraffin b) PP + 30% branched paraffin and c) PP + 30% FT

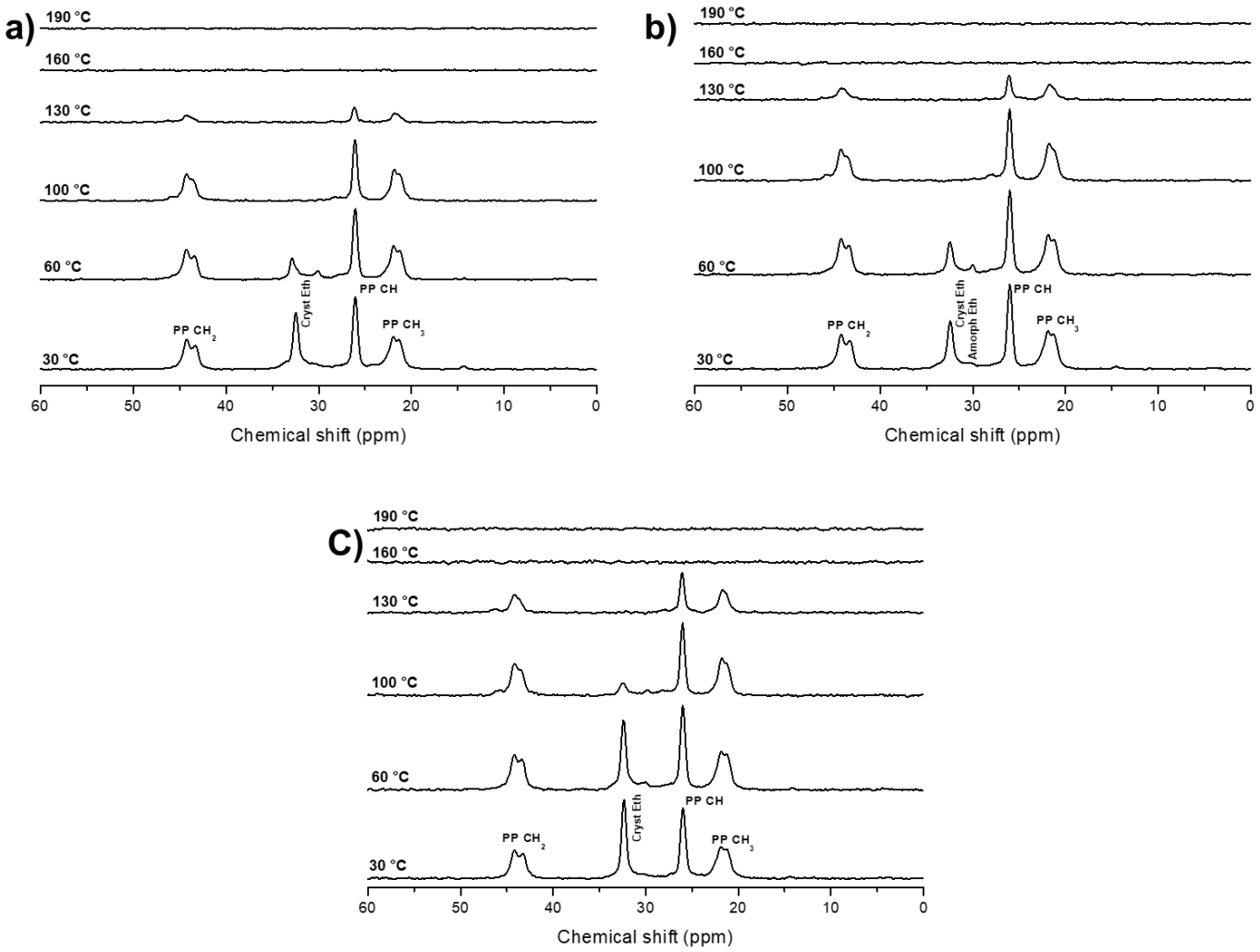

Figure 4. 10: VT CP/MAS spectra of a) HEPC + 30% linear paraffin b) HEPC + 30% branched paraffin and c) HEPC + 30% FT

During a CP experiment, the accumulation of magnetisation for a carbon depends on the extent to which it is coupled to the proton system. This magnetisation decays as function of the $T_{1\rho}$ of the protons and for sufficient polarisation to be transferred an optimal contact time exists for each sample. This knowledge can be manipulated to filter components of different relaxation rates from a spectrum and is known as a variable contact time (VCT) experiment. The VCT spectra in Figure 4. 11 and Figure 4. 12 were all obtained at 30 °C after the gradual cooling during which CP/MAS spectra were acquired. While contact time is a parameter optimised during calibration to yield the greatest intensity for each resonance in the CP/MAS spectrum, the array obtained during this calibration also yields information about relative mobility of the components. Typically, only the signals due to the more mobile components of a sample will remain visible in the spectrum at longer contact times. In the VCT spectra

the polypropylene signals display no change with contact time, most likely due to the fact that the specific contact time range employed here is not broad enough for the spectrum of polypropylene mobility. In contrast, the ethylene region does display changes with contact time, making this method ideal for probing the dynamics of the wax since only the wax will be affected in this timescale. For both the 10% and 30% blends the branched paraffin has the lowest remaining signal intensity at 5 ms while the FT blends have the greatest remaining signal intensity. It is proposed that the greater the extent of the interaction between the wax and the HEPC ethylene-rich regions the more the crystallinity of the wax is disrupted to form mobile crystalline domains which only become visible when the rigid crystalline domains are filtered out of the spectrum. Both FT and linear paraffin blends have the peak remaining at 5 ms at 32 ppm which is the chemical shift for crystalline ethylene. This suggested that the linear waxes interacted with the crystalline ethylene domains in the HEPC to form the above-mentioned mobile crystalline domains. In contrast, both crystalline and amorphous peaks remain at 5 ms for the branched paraffin implying a different interaction mechanism. It is likely that the branched paraffin experiences greater interaction with the ethylene-propylene rubber regions of the HEPC due to similarity with its own heterogeneous composition.

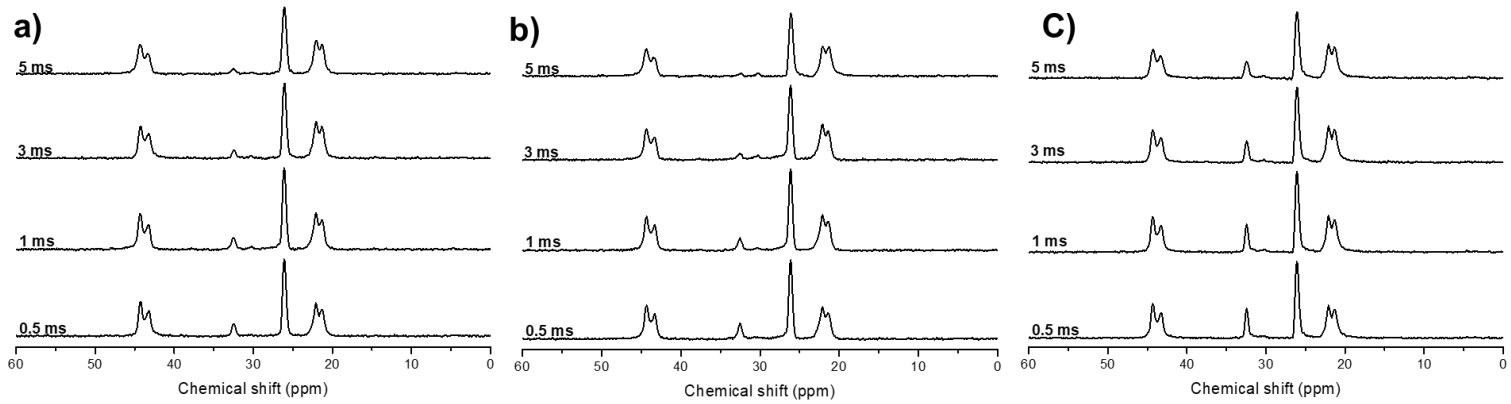

Figure 4. 11 CP/MAS VCT spectra of a) HEPC +10% linear paraffin b) HEPC +10% branched paraffin and c) HEPC +10% FT at 30 °C

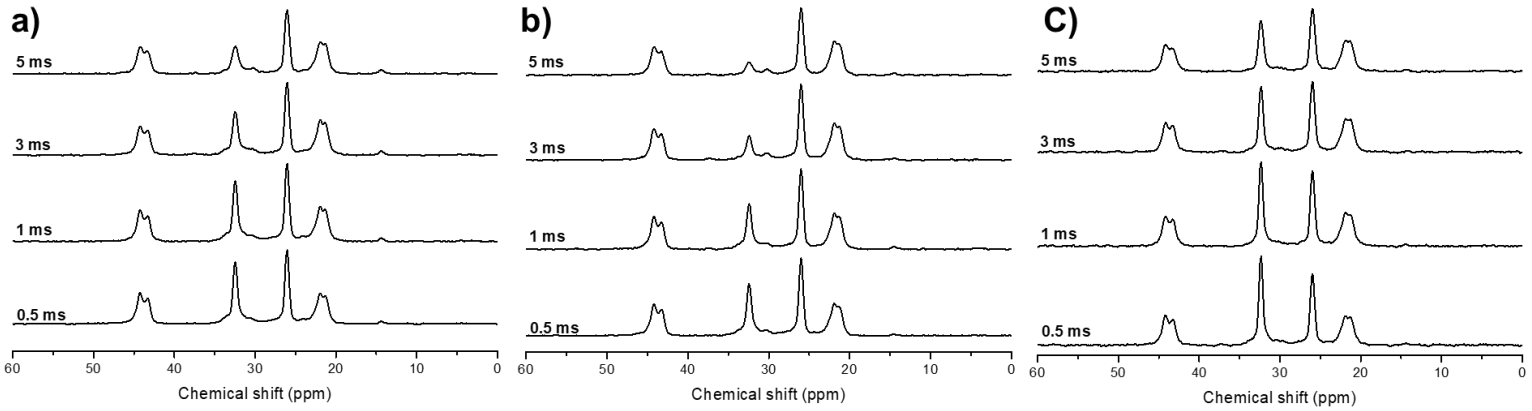

Figure 4. 12 CP/MAS VCT spectra of a) HEPC + 30% linear paraffin b) HEPC + 30% branched paraffin and c) HEPC + 30% FT at 30 °C

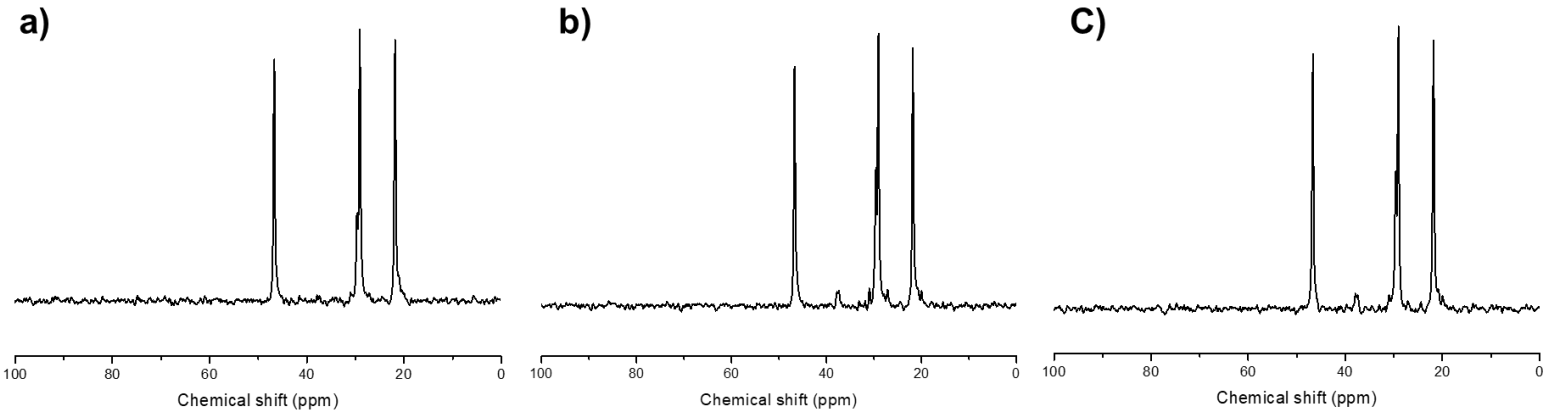

Figure 4. 13: SP spectra of a) HEPC + 10% linear paraffin b) HEPC + 10% branched paraffin and c) HEPC + 10% FT at 190 °C

Figure 4. 13 displays the single pulse excitation spectra of the HEPC 10% wax blends. Of interest is the peak at approximately 38 ppm which arises due to methylene resonances in the vicinity of ethylene defects within the polypropylene crystalline domain.[22] Typically, three peaks should be visible in this region for methyl, methine and methylene, however, the chemical shifts of these coincide with the methine and methyl major peaks and are possibly under the main peaks. The peak at 38 ppm is visible in the SP spectrum of the neat HEPC (Figure 4. 14a) but disappears from the SP spectra of the 10% linear paraffin blend (Figure 4. 13a) as well as the 30% FT blend (Figure 4. 14b). While the effect on the spectrum is the same, the cause is different in the case of the linear paraffin and the FT blends. According to the crystalline enthalpies, the 10% linear paraffin blends yielded the greatest crystallinity of the polypropylene domain of the HEPC while the 30% FT blend displayed the greatest disordered α-phase content according to CP/MAS results. In both these cases, a stronger interaction between the ethylene-rich domains of the HEPC with the wax may result in a lesser effect of these ethylene-rich domains on the polypropylene helix causing this particular peak to diminish. It may be suggested that since the peak at 38 ppm is associated with crystalline defects the differences between the spectra could be due to incomplete melting, however, all the blends as well as the neat HEPC achieve complete melting below 170 °C, roughly 20 °C below the acquisition temperature, making the previous explanation more likely.

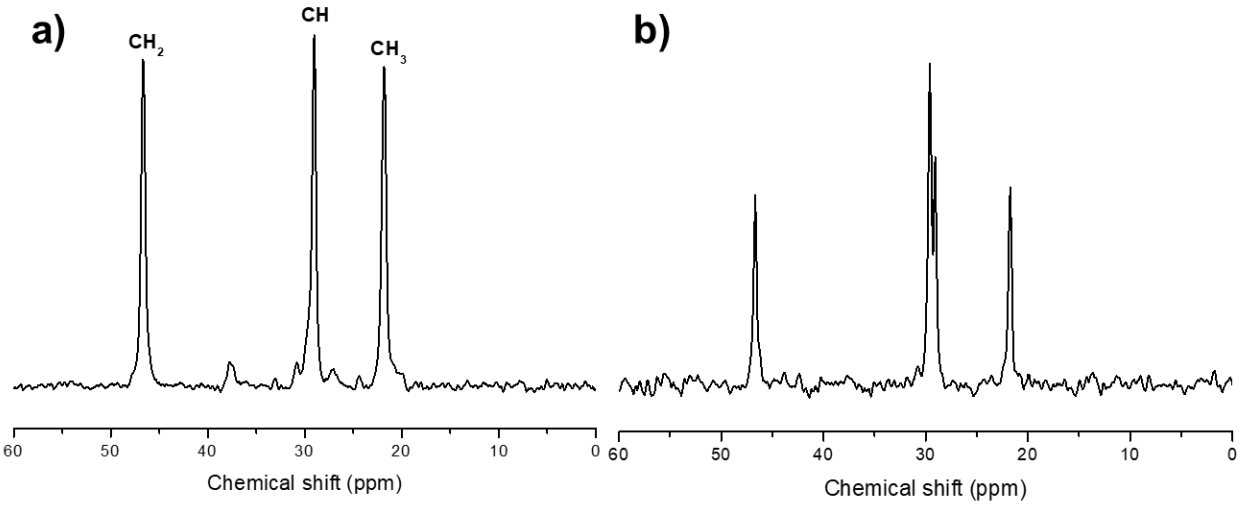

Figure 4. 14 SP spectra of a) neat HEPC and b) HEPC + 30% FT at 190 °C

4.3.2 Mechanical properties of HMAs

Technically the lack of polarity of polypropylenes results in low surface energy and poor adhesive properties, making them less suitable for adhesive applications. For this reason, additional components are added to form an adhesive formulation. The role of the additional component (the wax in this case) is to diffuse to the surface between the polypropylene and the substrate and enhance the adhesion of the polypropylene.[23] Figure 4.15 summarises the bond strength results of the HEPC/wax HMAs compared to an HMA formulation with no wax added. Overall, both 10% wax and 30% wax HMAs exhibit greater tensile moduli than the neat HEPC HMA. The crystallinity enhancement of the HEPC by the wax resulted in a more rigid HMA which required more strength to break the adhesive bond. The increased bond strength is a desirable characteristic but the higher melt viscosity of the 10% blends is not desirable due to difficulties which could arise during application. The 30% blends were more easily applied due to lower melt viscosity and melting temperature.

The tensile modulus of the HMAs were comparable to an industry standard but the standard was found to behave more consistently in strength and mechanism of failure. The test method approximates the standard industrial tear seal test in which a tear seal is characterised by the failure of the substrate and not the adhesive bond.[24] The neat HEPC HMA resulted in adhesive failure exclusively as shown in Figure 4.16, displaying the typical adhesion behaviour of highly crystalline polypropylenes. Adhesive failure is also known to occur when the components have low compatibility[25], suggesting that the tackifier and HEPC are not compatible. The inclusion of 10% wax in the formulation formed HMAs which were insufficiently tacky and too rigid. The HEPC/wax blend HMAs mostly resulted in substrate failure under tensile stress but the change in the dominant failure mechanism suggested that

the wax increased compatibility between the tackifier and the HEPC since both surfaces were strongly bound and the adhesive remained intact. With the addition of more wax some instances of cohesive failure were observed for the linear waxes in Figure 4.17 in addition to substrate failure. Cohesive failure also implies lower compatibility since this essentially means the adhesive is falling apart from the inside. The enhanced mobility within the crystalline domains observed for the linear wax blends seemed to decrease toughness of the HMA. The branched paraffin HMA was the only sample to display adhesive failure at 30%, implying that compatibility also decreased for high contents of branched paraffin. In addition, this HMA also had the lowest bond strength overall showing that increased amorphous regions has a more damaging effect than increased mobility within crystalline domains.

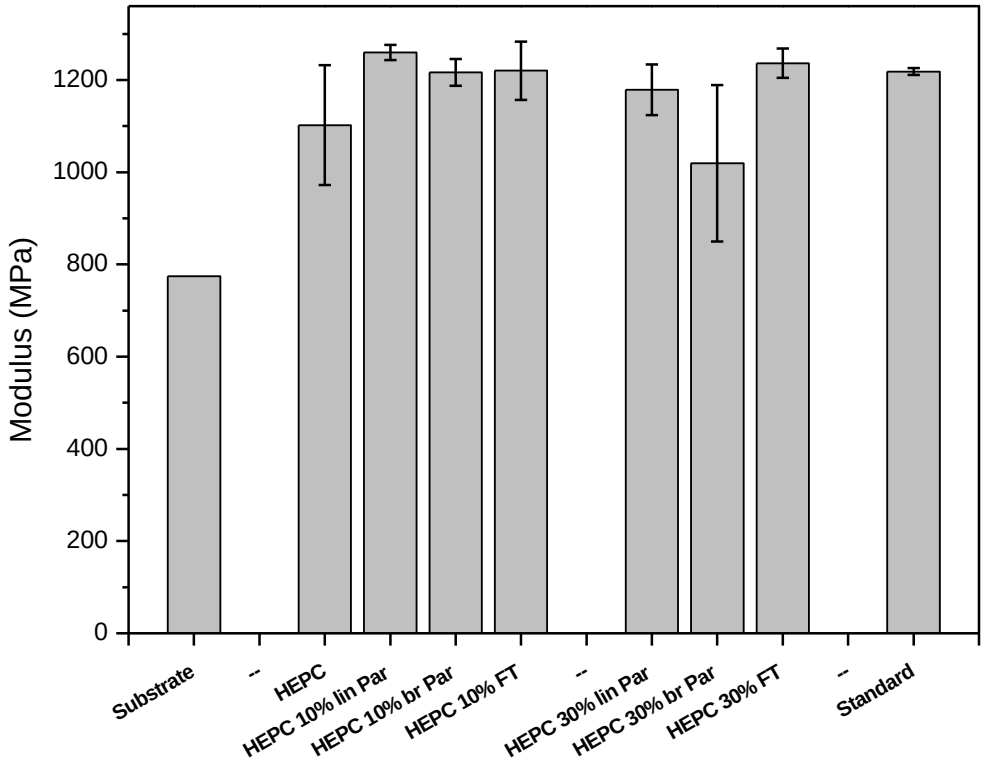

Figure 4. 15: Tensile moduli of HEPC HMAs

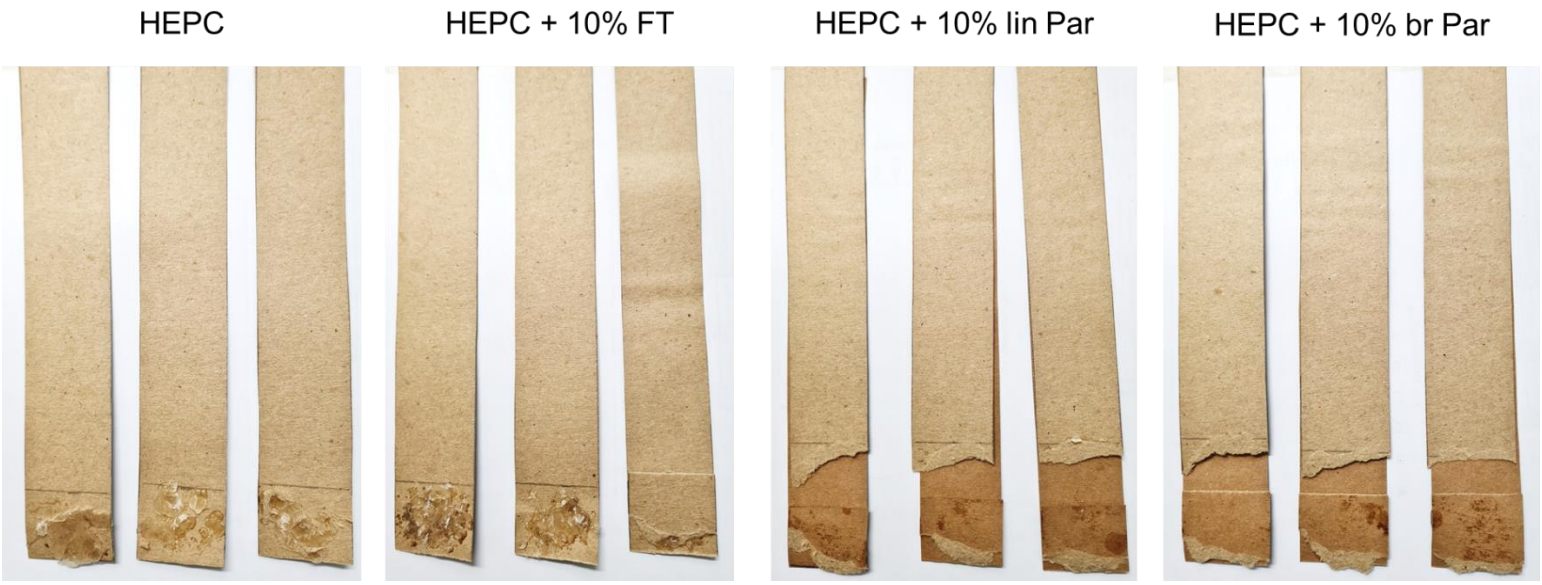

Figure 4. 16: Images of bond failure mechanisms of HEPC 10% wax HMA tensile samples

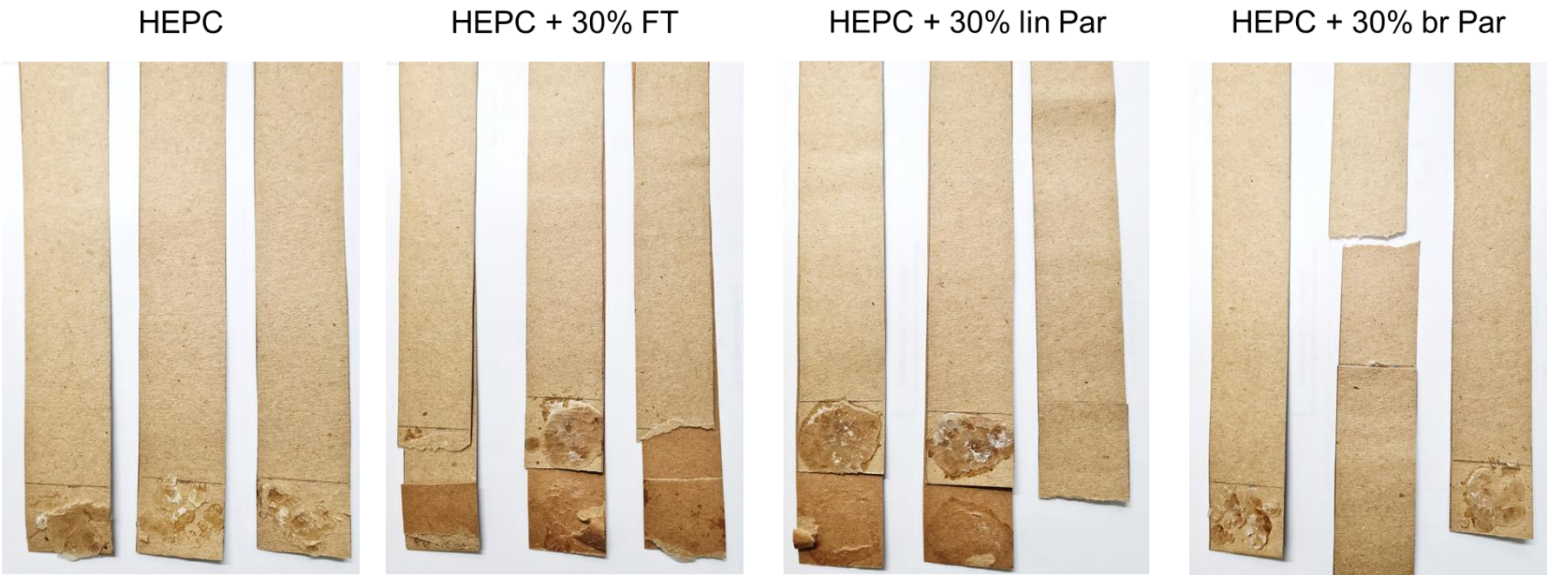

Figure 4. 17: Images of bond failure mechanisms of HEPC 30% wax HMA tensile samples

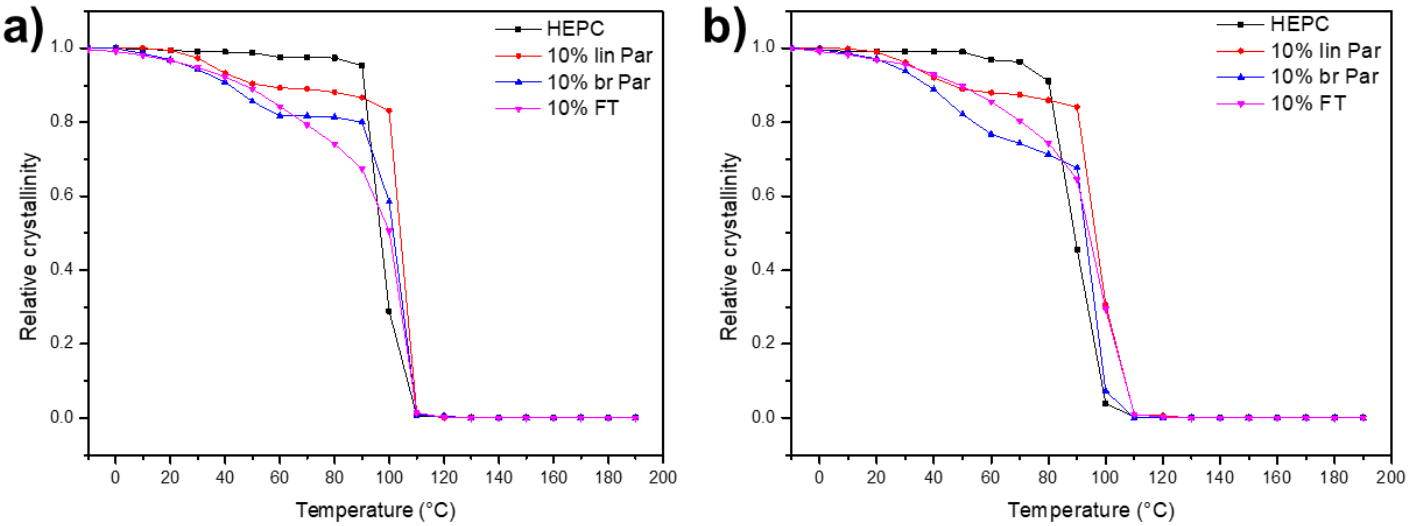

Figure 4. 18: Crystallisation rates of HEPC 10% wax HMAs at a) 10 °C/min and b) 20 °C/min

In all cases the wax promoted more rapid crystallisation of the HEPC but delayed achievement of full crystallinity at the later stages of crystallisation. The duration between crystallisation onset and achievement of full crystallisation of an HMA is known as the open time. Either long or short open times can be desirable depending on the application, but typically shorter open times are favoured for faster production rates but too rapid setting can result in problems during application of the adhesive to the substrate. Similarly to the trends observed in the VCT NMR spectra, the two linear waxes promoted the crystallisation rate the most. There was also a slight rate dependence of the crystallisation as the differences between the rates became more noticeable at faster crystallisation rates (Figure 4.18b). Increasing the wax concentration delayed the onset of crystallisation relative to the 10% HMAs but the extent of the delay was still not below that of the HEPC (Figure 4.19). At 30% wax the kinetics profiles agree with the conventional DSC thermograms in that the paraffin HMAs display two-step crystallisation for the HEPC and the wax separately while the FT displays a single gradual transition. Comparing Figure 4.19 to Figure 4.18, it can be seen that the open time is increased by the addition of 30% wax as the achievement of full crystallisation occurs at an even slower rate in Figure 4. 19. Additionally, the rate dependence of the HMA crystallisation appeared to lessen with increased wax concentration.

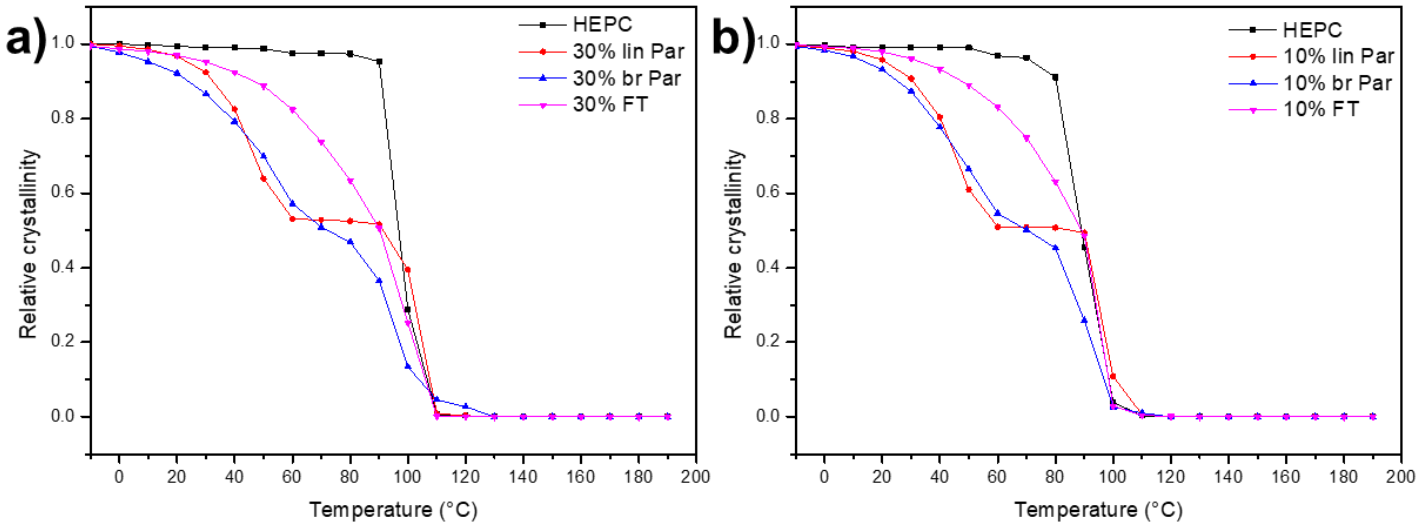

Figure 4. 19: Crystallisation rates of HEPC 30% wax HMAs at a) 10 °C/min and b) 20 °C/min

4.4 Conclusions

Understanding the interactions between various types of waxes with a high-ethylene content HEPC was not a simple task. The complexity of the HEPC already has significant effects on the isotactic polypropylene regions within the HEPC itself and the addition of wax adds to this complex range of interactions. From the analyses presented in this chapter we can conclude that the ethylene-rich regions on the HEPC have strong interactions with the wax and that the extent of this interaction depends on the wax type.

The NMR spectroscopy and DSC results show that the wax and the ethylene in the HEPC seem to associate while in the instance of the iPP the wax acts as an impurity which disrupts the iPP crystallisation. In the HEPC the high mobility of the wax in the melt may cause the compatible ethylene regions of the HEPC to move with it. Since the iPP in the HEPC would want to separate from the wax, the ethylene-rich regions and the iPP matrix would want to move in opposing directions which could result in overall decreased compatibility of the HEPC and therefore lower crystallinity and cohesive failure of the corresponding HMAs.

The kinetic graphs suggested that at low wax concentrations, the promotion of crystallisation rate plays a larger role and increased crystallisation is the major effect. At high wax concentrations, however, crystallisation disruption dominates and the crystallisation rate slows down. The paraffin waxes appear to behave independently of the polypropylene while the FT displayed enhanced interference. This was corroborated by the CP/MAS spectra which showed that in both 10% and 30% wax blends the FT wax displayed the least extent of peak

splitting of the methyl peak and therefore had the greatest quantity of disordered α-phase within the polypropylene crystal structure.

References

[1] R.D. Adams, ed., Adhesive Bonding, Woodhead Publishing Limited, Cambridge, 2005. http://app.knovel.com/web/view/swf/show.v/rcid:kpABSTA002/cid:kt00C5Y765/viewerType:pdf/root_slug:adhesive-bonding-science?cid=kt00C5Y765&page=25&q=flip chip&b-q=flip chip&sort_on=default&b-subscription=TRUE&b-group-by=true&b-sort-on=default (accessed September 15, 2021).

[2] I. Skeist, ed., Handbook of adhesives, Third edit, Springer US, 1990. https://doi.org/10.1007/978-1-4613-0671-9.

[3] K. Raheem, J. Cassidy, A. Betts, B. Ryan, Use of confocal Raman microscopy to characterise ethyl cyanoacrylate adhesive depth curing, Phys. Chem. Chem. Phys. 22 (2020) 23899–23907. https://doi.org/10.1039/d0cp04053c.

[4] F. Stojcevski, O. Siddique, G. Meric, J.D. Randall, N.S. Emonson, L.C. Henderson, Using in situ polymerisation to enhance adhesion of dissimilar materials, Int. J. Adhes. Adhes. 104 (2021) 102740. https://doi.org/10.1016/j.ijadhadh.2020.102740.

[5] W. Li, L. Bouzidi, S.S. Narine, Current research and development status and prospect of hot-melt adhesives: A review, Ind. Eng. Chem. Res. 47 (2008) 7524–7532. https://doi.org/10.1021/ie800189b.

[6] H.H. Shih, G.R. Hamed, Peel adhesion and viscoelasticity of poly(ethylene-co-vinyl acetate)-based hot melt adhesives. II. The influence of wax, J. Appl. Polym. Sci. 63 (1997) 333–342. https://doi.org/10.1002/(SICI)1097-4628(19970118)63:3<323::AID-APP7>3.0.CO;2-P.

[7] N.M. Ghasem, J. Heiderian, W.W. Daud, Effect of reaction temperature on conversion and thermal properties of polyamide hot-melt adhesives, Asia-Pacific J. Chem. Eng. 2 (2007) 599–608. https://doi.org/10.1002/apj.61.

[8] X. Chen, H. Zhong, L. Jia, J. Ling, R. Tang, J. Qiao, Z. Zhang, Polyesteramides Used for Hot Melt Adhesives : Synthesis and Effect of Inherent Viscosity on Properties, J. Appl. Polym. Sci. 81 (2001) 2696–2701.

[9] M. Lommatzsch, M. Biedermann, K. Grob, T.J. Simat, Analysis of saturated and aromatic hydrocarbons migrating from a polyolefin-based hot-melt adhesive into food, Food Addit. Contam. - Part A Chem. Anal. Control. Expo. Risk Assess. 33 (2016) 473–488. https://doi.org/10.1080/19440049.2015.1130863.

[10] J. Karger-Kocsis, Amorphous or atactic polypropylene, in: J. Karger-Kocsis (Ed.), Polypropyl. An A-Z Ref., Springer Netherlands, Dordrecht, 1999: pp. 7–12. https://doi.org/10.1007/978-94-011-4421-6_2.

[11] C. Zhang, Y. Bai, B. Cheng, W. Liu, Adhesion properties of atactic polypropylene/acrylate blend copolymer and its adhesion mechanism for untreated polypropylene materials, Int. J. Adhes. Adhes. 80 (2018) 7–15. https://doi.org/10.1016/j.ijadhadh.2017.09.007.

[12] H.H. Shih, G.R. Hamed, Peel adhesion and viscoelasticity of poly(ethylene-co-vinyl acetate)-based hot melt adhesives. I. The effect of tackifier compatibility, J. Appl. Polym. Sci. 63 (1997) 323–331. https://doi.org/10.1002/(SICI)1097-4628(19970118)63:3<323::AID-APP7>3.0.CO;2-P.

[13] M. Gahleitner, C. Tranninger, P. Doshev, Heterophasic copolymers of polypropylene: Development, design principles, and future challenges, J. Appl. Polym. Sci. 130 (2013) 3028–

3037. https://doi.org/10.1002/app.39626.

[14] G. Estan-Cerezo, J.M. Martín-Martínez, Thermal, viscoelastic and adhesion properties of EVA (ethylene-co-vinyl acetate) hot melts containing polypropylene waxes of different nature, J. Adhes. Sci. Technol. 29 (2015) 875–889. https://doi.org/10.1080/01694243.2015.1006302.

[15] I. Krupa, A.S. Luyt, Thermal properties of polypropylene/wax blends, Thermochim. Acta. 372 (2001) 137–141. https://doi.org/10.1016/S0040-6031(01)00450-6.

[16] A. Turner-Jones, Development of the γ-crystal form in random copolymers of propylene and their analysis by DSC and X-ray methods, Polymer (Guildf). 12 (1971) 487–508. https://doi.org/10.1016/0032-3861(71)90031-0.

[17] L. Botha, P. Sinha, S. Joubert, H. Duveskog, A.J. Van Reenen, Solution and solid-state NMR characterization of heterophasic propylene-ethylene copolymers (HEPC) with increasing ethylene content, Eur. Polym. J. 59 (2014) 94–104. https://doi.org/10.1016/j.eurpolymj.2014.07.010.

[18] L. Botha, P. Sinha, H. Duveskog, A.J. Van Reenen, The use of solid-state NMR to investigate the development of segmental mobility in commercial heterophasic ethylene propylene copolymers (HEPCs), Macromol. React. Eng. 9 (2015) 313–324. https://doi.org/10.1002/mren.201400043.

[19] H.S. Mpanza, A.S. Luyt, Influence of different waxes on the physical properties of linear low-density polyethylene, South African J. Chem. 59 (2006) 48–54.

[20] M.J. Hato, A.S. Luyt, Thermal fractionation and properties of different polyethylene/wax blends, J. Appl. Polym. Sci. 104 (2010) 2225–2236. https://doi.org/10.1002/app.

[21] M.A. AlMaadeed, S. Labidi, I. Krupa, M. Ouederni, Effect of waste wax and chain structure on the mechanical and physical properties of polyethylene, Arab. J. Chem. 8 (2015) 388–399. https://doi.org/10.1016/j.arabjc.2014.01.006.

[22] R.G. Alamo, D.L. VanderHart, M.R. Nyden, L. Mandelkern, Morphological partitioning of ethylene defects in random propylene-ethylene copolymers, Macromolecules. 33 (2000) 6094–6105. https://doi.org/10.1021/ma000267i.

[23] I. Novák, I. Krupa, A.S. Luyt, Modification of the polarity of isotactic polypropylene through blending with oxidized paraffin wax, J. Appl. Polym. Sci. 94 (2004) 529–533. https://doi.org/10.1002/app.20935.

[24] L.W.J. Hall, J.S. Boyer, R.E. Ware, Hot melt adhesive containing atactic polypropylene and polyethylene, US3370106A1, 1968.

[25] Š. Florián, I. Novák, Adhesive properties of some pressure-sensitive adhesive agents containing oligomer additives, Die Angew. Makromol. Chemie Appl. Macromol. Chem. Phys. 239 (1996) 55–62. https://doi.org/10.1002/apmc.1996.052390106.

Chapter 5
The Mechanism of Oil Entrapment in Waxes: An Investigation into The Applicability of Wideline NMR spectroscopy for the Determination of Oil Contents

5.1 Introduction

Waxes are important raw materials in the manufacture of a number of commercial goods, including candles, cosmetics, coatings and adhesives. Initially a waste by-product of oil refining, the unique physical and mechanical properties of waxes have made them vital to modern industry. As a result, the wax market has grown and include Fischer-Tropsch (FT) waxes, crude-oil derived paraffin waxes, olefinic waxes and wax blends. In each wax category a number of key properties determine its functionality in various applications. These are hardness, congealing point, molecular weight, crystallinity and the oil content.[1]

Two classes of waxes dominate the market; these are crude-oil derived paraffin waxes and FT waxes. FT waxes are produced by the Fischer-Tropsch process in which syngas (a mixture of hydrogen gas and carbon monoxide) is catalytically converted to linear paraffins with chain lengths typically in the range of a hundred carbons.[2] Minimal branching is observed in FT waxes and the oil component is mostly short-chain hydrocarbons. In contrast, crude oil comprises a variety of hydrocarbons such as paraffins, resins and aromatics.[3] The wax present in crude oil is principally composed of n-paraffins, branched paraffins, cyclo-paraffins, and low level aromatics.[4] Consequently, the oil component found in crude derived waxes predominantly contains branched and cyclic material.[5]

ASTM D-721 is the standard test method for determination of oil content in waxes. This method involves the dissolution of the wax in methyl ether ketone (MEK), cooling the solution to -32 °C to precipitate the wax and subsequently filtering the wax from the solution. The MEK is then evaporated to leave the oil residue which is weighed and compared to the starting mass of the wax.[6] This test method poses a number of challenges namely the extensive time needed to perform the test, difficulties in repeatability and reproducibility as well as the use of hazardous solvents.[7]

For these reasons an NMR spectroscopic method is desirable. Solid-state NMR spectroscopy offers a fast, solvent-free and reliable alternative to the ASTM D-721 method. The basis for the solid-state NMR spectroscopic method is the proton (^{1}H) Wideline experiment. The Wideline is a static experiment in which broad signals are acquired as a result of the anisotropic interactions between dipolar nuclei such as ^{1}H and ^{19}F.[8] Large amplitude molecular motions typically display narrow linewidths while more rigid segments containing

molecular motions within the range of proton coupling exhibit broad linewidths.[9] This allows the signals of the more mobile oil component to be separated from the signals of the rigid wax matrix and therefore the quantification of the oil. Commercial bench-top NMR technologies claim to give accurate oil contents based upon a calibration with various waxes of known oil content determined by ASTM D-721. These methods were originally developed for the agricultural industry and optimised for observation of oils within seeds providing the benefit of high-throughput without the need for crushing the seeds.[10] The NMR spectroscopic methods produced highly accurate results except in seeds with high moisture retention[11],[12] leading to increasing popularity of the Wideline NMR spectroscopic method for oil contents in general.

Researchers in the oil industry, in contrast, have applied NMR spectroscopy for the determination of the wax content of crude oils. Crude oils contain a multiple distributions of carbon chain lengths. The heavier fractions often precipitate out of the liquid as wax during oil extraction or transport. The deposition of wax from crude oil is undesirable as it tends to cause blockages of pipelines or equipment. Attempts have been made to characterise the composition of crude oils in order to predict their behaviour and prevent the operational costs involved with unwanted wax precipitation.[13] Characterisation of crude oils from Libya's Bouri oilfields by GC and DSC revealed that the wax appearance temperature (WAT), the temperature at which the heavy fraction begins to crystallise[14], depends both on the quantity of the heavy fraction and its ratio to the rest of the distribution.[15] Empirical relationships between viscosity and temperature of Malaysian crude oils have also been modelled.[16] These reports have all focused on using physicochemical properties to predict behaviour of waxes and oils. Pedersen et al. have also used the pulsed NMR spectroscopic method for wax content of crude oils by comparing the initial and final amplitudes of the FID and relating them to the proton quantity of the solid and liquid phases respectively.[17]

Despite the benchtop solid-state NMR method's popularity, companies have reported discrepancies between the values yielded by these technologies and the ASTM D-721 method. Since the ASTM method is the industrially recognised standard, any alternative procedures must comply with this test method to be meaningful to a wax manufacturer. The discrepancies between gravimetric and spectroscopic methods has been addressed by Kané et al.[18] The signal intensities acquired in a Wideline experiment are proportional to the proton density of the sample, not the mass. The ASTM method is a gravimetric method and can therefore not be directly compared with the signals in the NMR spectrum. Kané et al. propose correction factors for this discrepancy which will be described in detail later in this work. Another reason for the differences between the results is the scale of the analysis. NMR spectroscopic methods typically analyse a small representative sample, while the original

methods have been proposed for large scale quality assurance within plants and are usually more accurate for waxes of generally high oil contents.[19],[20]

In this chapter the mechanism of oil entrapment by waxes is investigated in order to understand the discrepancies between various oil content determination methods. FT waxes comprise the focus of the research as FT waxes have not been discussed in this context in detail. A brief comparison with a paraffin wax is also performed to test how the results compare to that of the available oil content literature which deals almost exclusively with paraffin waxes.

5.2 Materials and Methods

5.2.1 Sample preparation

The oil used in this study was obtained by sweating from a high oil content commercial FT wax for use in cosmetics applications. The peak melting temperature of the unsweated wax was approximately 40 °C and sweating was performed at 34 °C. As the original sweated oil contained a significant quantity of wax, the oil was further purified by reheating and slow cooling to 25 °C. The fraction which remained liquid at 25 °C was used as the oil in this research. This oil was melt-blended into a variety of waxes by heating the components to 150 °C under agitation. FT waxes of different melting ranges were used to prepare the blends; a medium melting, high melting and hard wax. Oil contents as determined commercially by ASTM D-721 and densities of the waxes are presented in Table 5. 1. The blends were slow cooled before analysis.

Table 5. 1: Attributes of waxes used for preparation of oil/wax standards†

Wax	Oil Content (%)*	Density (g/mL)
Hard wax	0.0	0.80
High melting wax	0.5	0.78
Medium melting wax	2.5	0.71
Paraffin wax	0.7	0.78

†Obtained from supplier data sheets *According to ASTM D-721

5.2.2 Solid state NMR spectroscopy

Solid state NMR spectroscopic analysis was performed on a Varian VNMRS 500 MHz NMR spectrometer equipped with two channels and a 4 mm Chemagnetics T3 HX MAS probe. Samples were prepared by packing finely cut samples into 4 mm zirconia rotors. Static ^{1}H experiments were performed at room temperature (25°C) using a ^{1}H 90° pulse of 2.25 µs. Spin-spin relaxation times, T_2, were measured with a Hahn echo pulse sequence, 90°–τ–180°–τ-acquire.

Data processing was done using the OriginPro® 8.5 software. Widelines were fitted using the Peak Analyzer with combinations of Gaussian and Lorentzian fitting functions. T_2 exponential decays were fitted using both two component exponential decay functions as well as linear combinations of exponential decay functions and compared for the best fitting.

5.2.3 DSC

Thermal analysis was performed on a Netzsch DSC Polyma 214 calorimeter. Sample preparation involved melting of the bulk blend and weighing a liquid sample in order to obtain a representative sample for DSC analysis. All samples were heated to a maximum temperature of between 150 °C and maintained isothermally for 5 minutes. Subsequently the samples were cooled to -40 °C and heated and cooled again. The heating and cooling rates were kept constant at 10 K/min. Melting points and enthalpies were determined from the second heating thermogram. All sample masses were between 5 – 6 mg. Temperature calibration was performed with indium standards.

5.2.4 GC-MS

GC-MS sample preparation was performed by dissolving the wax in xylene to a concentration of 10 mg/mL. Separation was performed on a gas chromatograph (6890N, Agilent technologies network) coupled to an Agilent technologies inert XL EI/CI Mass Selective Detector (MSD) (5975B, Agilent technologies Inc., Palo Alto, CA). The system was coupled to a CTC Analytics PAL auto-sampler. Separation was performed using a non-polar ZB-Semi volatile (30 m, 0.25 mm ID, 0.25 µm film thickness) Zebron 7HG-G027-11-GGA capillary column. Helium was used as the carrier gas at a flow rate of 1 ml/min. The injector temperature was set to 250 °C. 1µl of the sample was injected in a split ratio was set at 100:1 split ratio. The oven temperature was programmed as follows: 35 °C for 10 minutes then ramped up to 320 °C at a rate of 8 °C/min and held for 2 minutes. The MSD was operated in full scan mode and the source and quad temperatures were maintained at 230 °C and 150 °C respectively. The transfer line temperature was maintained at 250 °C. The mass spectrometer was operated under electron impact mode at ionization energy of 70 eV, scanning from 35 to 500 m/z.

5.2.5 HT-GC

The carbon distribution and the degree of branching were determined on a Hewlett-Packard 5890 Gas Chromatograph fitted with a split-splitless inlet system with constant pressure control, operated at 75 kPa throughout the analysis. A Flame Ionization Detector (FID) was used for detection. The injector and detector were both operated at 400 °C. The instrument was fitted with a Restek MXT-1 capillary column (15m x 0.28 mm, 0.1 µm) and helium was used as carrier gas. The programmable oven was programmed from a starting temperature of 60 °C, held for 2 minutes, raised by 10 °C/min to a final temperature of 430 °C, held for 2

minutes. The samples were dissolved in cyclohexane before injection of 1 µL in splitless mode. For hard waxes, the oven was programmed from a starting temperature of 60 °C, held for 2 minutes, raised by 10 °C/min to a final temperature of 430 °C, held for 15 minutes to separate and elute the heavy components.

5.2.6 CLSM

Micrographs were obtained using a LSM780 confocal microscope (Zeiss, Germany) using ZEN 2012 software. Images were collected using the EC Plan-Neofluar 10x/ 0.3 M27 and LD Plan-Neofluar 40x/ 0.6 Corr M27 objectives. Excitation was performed with a 514 nm Argon multi-line laser and emission was detected in the range 539 – 753 nm. Laser power, gain and pinhole size were optimised for the most suitable signal intensity.

5.3 Results and Discussion

5.3.1 Characterisation of standards

The oil used was found to have a fairly broad carbon number distribution within the range C13 – C32, as shown by the GC-MS chromatograms in Figure 5. 1. The oil also contains a higher carbon number fraction which is evidence of a wider distribution than would typically be expected for an oil. This relatively heavy fraction is also evident in the DSC thermogram of the oil in Figure 5. 3 by the high crystallinity of the oil at low temperatures. Waxes were chosen with varying degrees of overlap in the carbon number distributions. In Figure 5. 1 the GC-MS chromatograms of the oil were overlayed with the HT-GC results for the waxes used in this study. The hard wax displayed the least overlap in carbon number distribution (C13 – C108) followed by the high melting wax (C13 – C80) and the medium melting wax (C13 – C40) with the greatest overlap in distribution. It is expected that the greater the extent of overlap, the greater the interactions between the wax and the oil.

The HT-GC chromatograms of the blends in Figure 5. 2 confirm the predictions from the simulated overlays of the neat components. From hard wax to medium melting wax the extent of overlap increases to such an extent that for the medium melting wax it is almost impossible to distinguish the oil from the wax. The oil seems to normalise the distribution of the medium melting wax by increasing the concentration of the lower carbon numbers. The effect of these interactions on the accurate measurement of oil contents plays a role in all methods, including gravimetric methods such as ASTM D-721. The stronger the association between the wax and the oil, the less likely the wax is to release the oil for quantification. Whether by extraction or spectroscopic methods, the oil signal must be separated from the wax signals for accurate oil content determination. This concept forms the basis of all the approaches followed in this chapter.

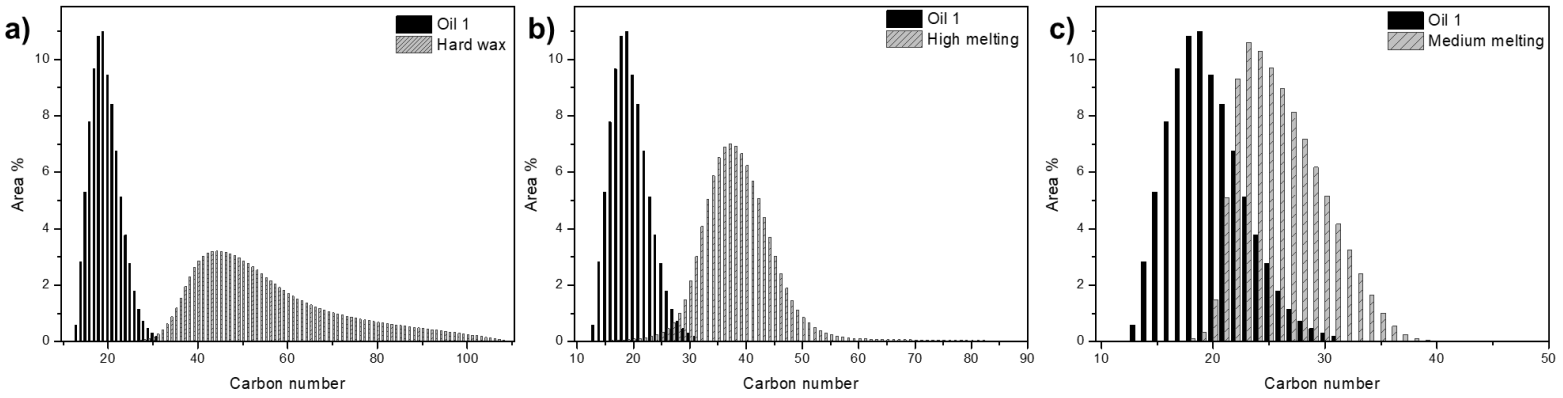

Figure 5. 1: Carbon number distributions of oil compared to a) hard wax b) high-melting wax and c) medium melting wax

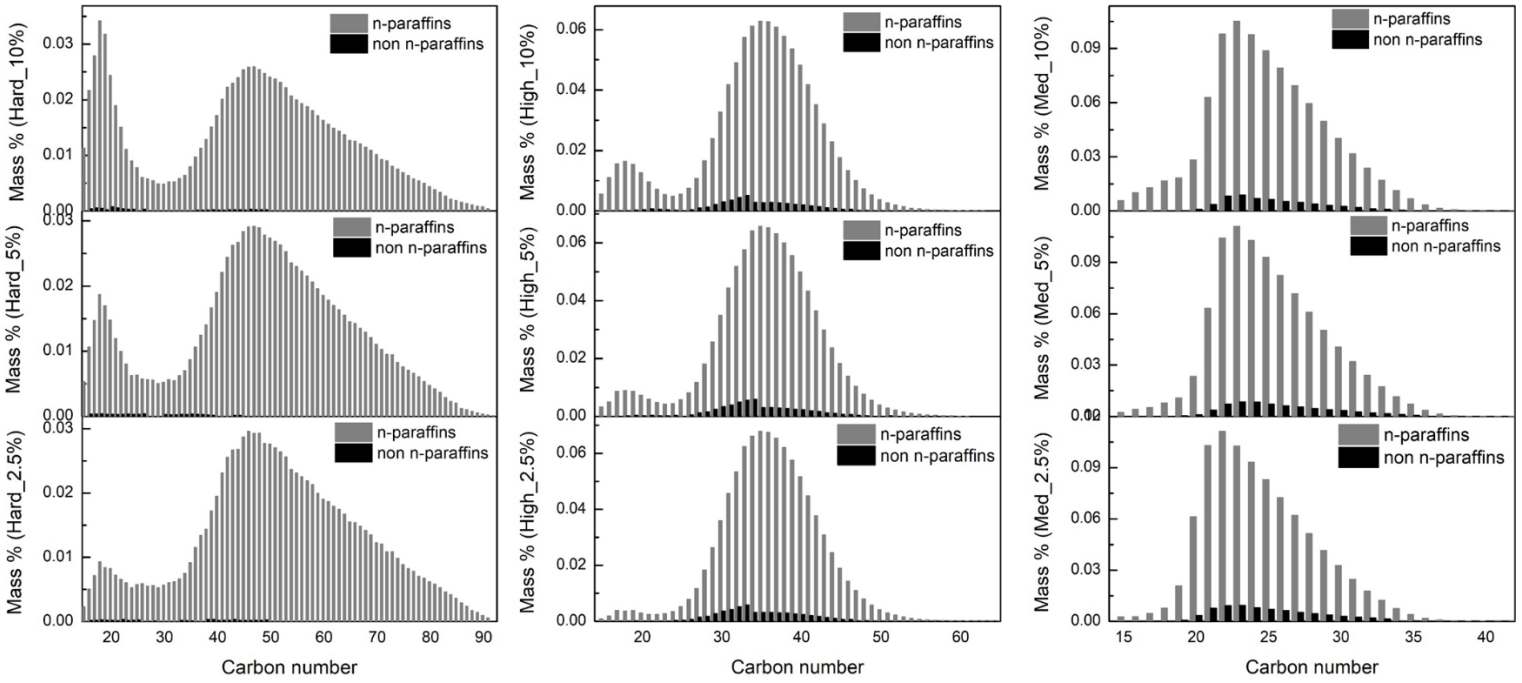

Figure 5. 2: Carbon number distributions of oil/ wax blends

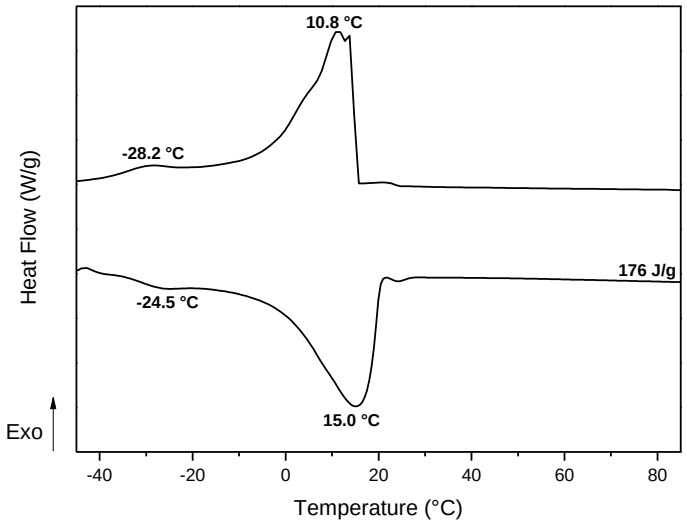

Figure 5. 3: DSC profile of FT sweated oil used in standard preparation

The peak melting and crystallisation temperatures of the hard wax remain practically unchanged with the addition of the oil, as can be seen in Figure 5. 4. In all cases the blends have been labelled according to the quantity of oil added irrespective of the initial oil content in Table 5. 1. The hard wax displays a typical profile for higher FT waxes containing a bimodal melting and crystallisation profile indicative of two types of crystal distributions. The addition of 0.5 % oil appeared to decrease melting enthalpy significantly, suggesting that the oil acted as an impurity and disrupted the crystallisation of the wax. This decrease was consistently observed after repeated analysis. Above this oil content, the melting enthalpy increases once again and stabilises. Separate crystallisation of the oil was not observed until 10 % oil was added. This suggested that the oil was dispersed within the wax matrix with lower molecular weight chains interfering with wax crystallisation and heavier chains co-crystallising with the wax. From Figure 5. 3 the oil is expected to melt and crystallise between 10 and 15 °C but this was not observed for blends below 10 %. At 10 % oil the wax appeared to be saturated and could no longer accommodate oil within its structure. At 10 % oil content the DSC profile suggests that the oil has become sufficient to form its own domains and crystallise independently. This additional crystallisation contributed to the increase in enthalpy observed for this sample in Figure 5. 4. While it is clear that the oil disrupts the crystallinity of the wax, the converse is also true as the presence of the wax prevents the oil from achieving the relatively high crystallinity which it would in isolation as seen in Figure 5. 3.

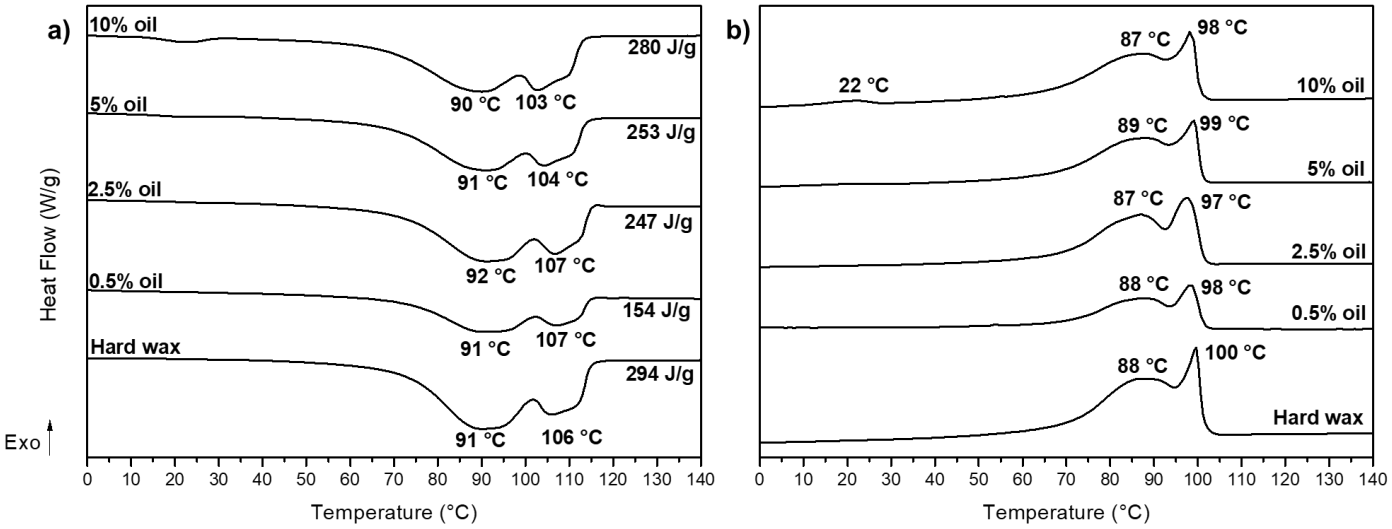

Figure 5. 4: DSC thermograms of a) melting and b) crystallisation of hard wax standards

As expected, due to the increasing overlap in carbon number distributions, the DSC profiles of the high melting wax in Figure 5. 5 displayed significant changes upon the addition of increasing quantities of the oil. While peak temperatures remain similar, the shape of the profiles coalesces from a split peak into a single crystalline distribution. Considering the two crystalline distributions within the high melting wax to have different crystal sizes (the higher melting being the larger and better developed crystals), the presence of the oil increases the quantity of crystallisable material promoting further crystal growth of the less perfect crystalline distribution. In Figure 5. 5 the thermogram tends towards the higher melting peak with increasing oil content. The increase in the quantity of oil in the blend implies an increase in the amount of chains in the overlap region of the GC chromatograms and therefore a greater effect on the lower carbon number chains within the high melting wax. This also explains why no independent oil crystallisation was observed. Once again, the 0.5 % oil content caused a considerable decrease in enthalpy after which the interaction becomes so great that the disruption of crystalline domains of both the wax and the oil overcomes the effect of greater quantities of crystallisable material at high oil contents. This leads to the lower melt enthalpy observed for the 10 % oil sample in Figure 5. 5.

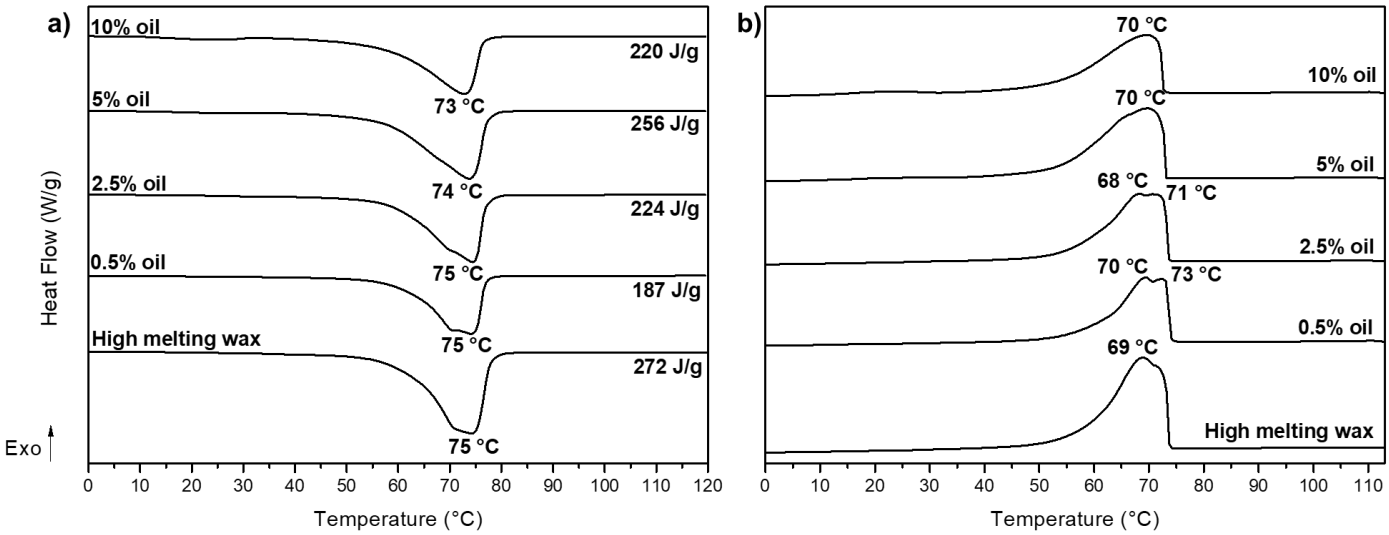

Figure 5. 5: DSC thermograms of a) melting and b) crystallisation of high melting wax standards

The medium melting wax with the greatest overlap in carbon number distribution was expected to show the greatest change in DSC profiles upon addition of the oil. From Figure 5. 6 this is only partially true. The neat wax contains a high melting peak which displayed no observable change. The lower melting peak appeared to interact with the oil to a greater extent, shifting to slightly lower peak temperatures. In this case the effect of the oil on melting enthalpy appeared more gradual. The initial decrease in enthalpy at 0.5 % oil and subsequent enthalpy stabilisation was observed similarly to the hard wax and high melting wax above. It is likely that co-crystallisation of the oil with the lower melting component of the wax caused the shift of the lower melting peak to lower peak temperatures. Similarly to the high melting wax, there appeared to be a limit to the increase in enthalpy due to the addition of more crystallisable material in the 10 % oil sample.

The manner in which the oil interacts with the wax appeared to be different for each class of wax. Due to the existence of a significant “oil” component already present within the medium melting wax it appeared to be the least dramatically affected by the inclusion of the added oil. Interestingly, the hard wax with the highest oil content was the only thermogram to display independent crystallisation of the oil despite the addition of fairly large quantities to all the waxes. Compositionally, the increase in melting temperature of the waxes is related to the linearity of the wax chains. The hard wax therefore has the lowest quantity of amorphous material while the medium melting wax contains the greatest. It is expected that where the amorphous content is high the oil will associate with the amorphous domain and mobility enhancement is as a result of the increase in overall amorphous regions. In the case of the higher melting waxes where the amorphous material is very low, the oil simply fills the

interstitial spaces between crystals. Enhanced mobility in these cases occurs due to increased mobility of the crystalline domain. Therefore all the FT waxes, even the hard wax, have a certain degree of interaction with the oil which complicates the accurate determination of oil content values.

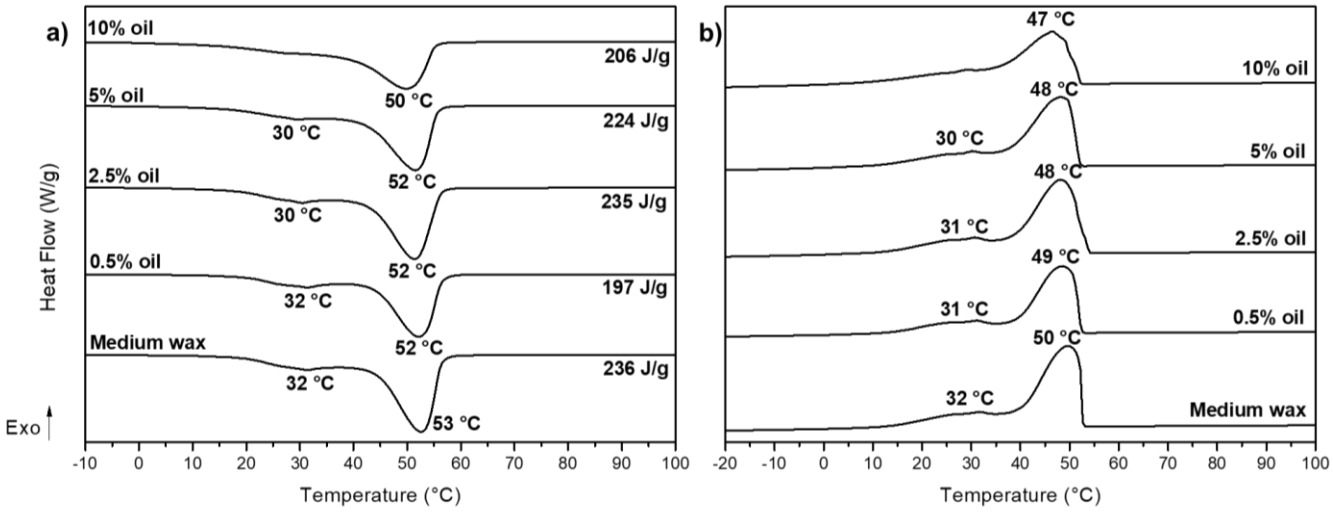

Figure 5. 6: DSC thermograms of a) melting and b) crystallisation of medium melting wax standards

5.3.2 Approaches to oil content determination by solid state NMR spectroscopy

5.3.2.1 Direct approach

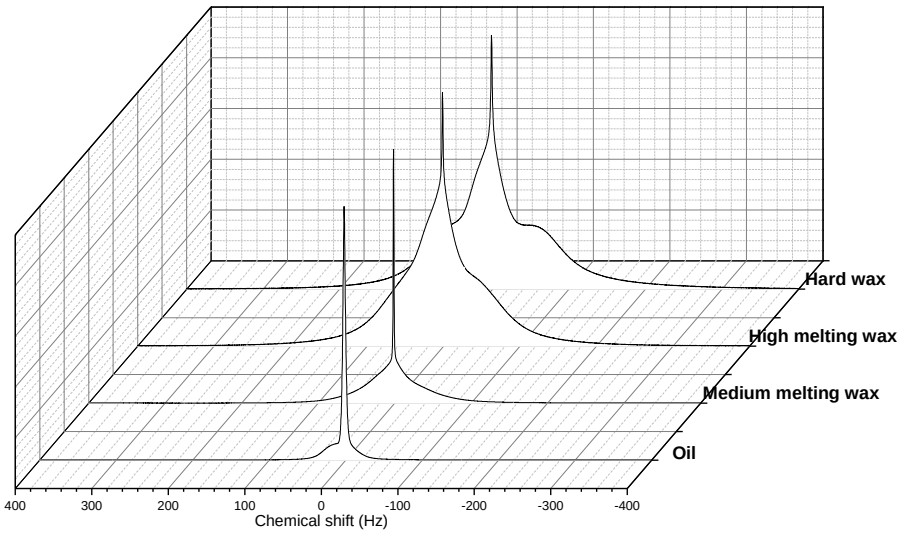

Figure 5. 7: ^{1}H Wideline spectra of neat oil and waxes

In this approach the aim was to deconvolute the total wideline spectrum into its constituents – the signals arising due to the mobile and rigid components of the sample. The area percentage

of mobile fraction within the oil sample was 79.6 % by deconvolution and integration of the Wideline spectrum. This demonstrates the complexity of the oil which contains wax components that are able to crystallise and form relatively rigid domains. According to ASTM D721 the true oil content of the oil used is approximately 12%, referring solely to the lightest fractions of the carbon number distribution. This also highlights the disparity between mobility as calculated by gravimetric methods and spectroscopic methods. The shape of the spectra in Figure 5. 7 also emphasises the increasing quantity of amorphous regions which is visible by the decrease in the broad base of the Wideline from hard wax to oil. Note that while the high melting wax and the hard wax have similar overall melt enthalpies the amount of long-range order is less for the high melting wax. The greater amorphous content may seem insignificant but plays an important role in the interaction of the wax and the oil.

Table 5. 2: Integrated area percentages of oil components by deconvolution of Wideline spectra

Added oil (mass %)	Hard wax (%)	High melting wax (%)	Medium melting wax (%)
0	0	0	3.7
0.5	0	0	5.7
2.5	0	2.6	8.8
5	5.5	4.1	9.9
10	6.5	5.4	13.6

The integrated areas in Table 5. 2 suggest that for higher melting waxes the method cannot detect an oil signal below a minimum of approximately 2.5 wt%. This minimum value is higher for more rigid waxes and can be correlated to the rapid crystallisation of the FT hard waxes which facilitates trapping of oil between crystallites. This is especially likely if the oil is broken up into small pools (as a result of rapid stirring during the preparation process) before trapping. The smaller the pools of oil the greater the effect of the surrounding rigidity on the interfacial region, effectively “freezing” the oil and making it indistinguishable from the wax.

The medium melting FT wax was the only sample to display a gradual increase in oil content as was expected. The increase is, however, not proportional to the predetermined oil contents of the standards even factoring in the inherent oil present in the wax. The results in the table above are summarised in Figure 5. 8 which correlates the calculated oil content with the predicted oil content to approximate a calibration curve. These observations all suggest an interaction between the oil and the wax, facilitated by the complexity of the oil. There is no distinct boundary between components, which complicates the determination of a definitive number for oil content. While this direct approach showed promise and yielded valuable information on the oil/wax systems, it did not provide the expected oil percentage. The

deconvolution clearly displays a narrow peak with a similar line shape to that of the oil sample in Figure 5. 7 which implies that the oil signal can be isolated. Without any further filters being applied, however, the mobility of the oil signal appeared to be heavily influenced by the wax matrix leading to skewed area percentages. It is important to distinguish that these calculated numbers may not be incorrect, they are possibly true representations of the sample as a whole. A lower oil content than expected suggests some of the oil (perhaps at the interface between wax and oil) acquiring some of the mobility features of the nearby wax while a higher oil content implies a disruption of wax crystallinity by the oil to form mobile crystalline domains. Clearly these interactions make determination of oil content in waxes a grey area when using simple Wideline experiments.

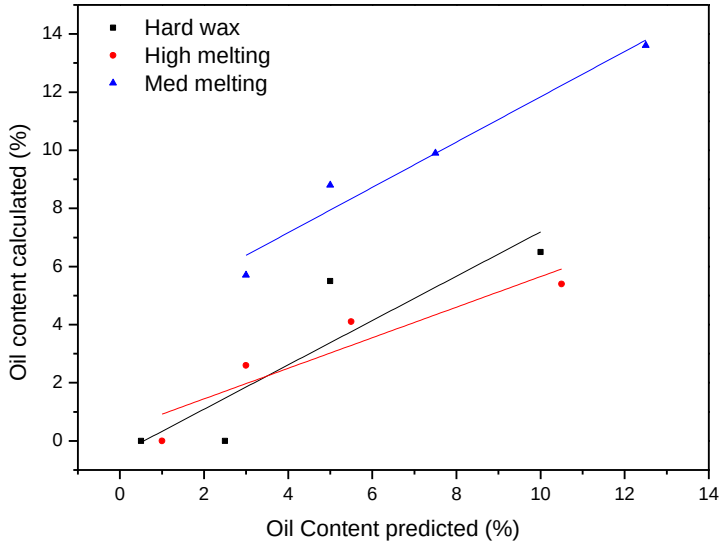

Figure 5. 8 Correlation between predicted oil content and calculated oil content by Wideline NMR spectroscopy

5.3.2.2 Spin-spin relaxation approach

The use of relaxation times to separate components is not a new idea. Various relaxation methods have been employed to separate amorphous from crystalline components in semi-crystalline polymers[21], to separate branched material of different lengths[22] and to determine domain sizes in block copolymers[23]. Spin-spin relaxation or T_2 relaxation measures mobility at the microsecond to millisecond scale. Longer T_2 relaxation times imply more mobile regions while shorter T_2 relaxation times correlate to rigid regions. In this way we aimed to separate the wax from the oil by determining the contribution of the slower relaxing oil as opposed to the contribution of the faster relaxing wax. Figures 5.10 – 5.12 display the T_2 relaxation curves of oil/wax standards of hard wax, high melting wax and medium melting wax respectively.

Similarly to the Wideline results above, the curves for hard wax and high melting wax standards do not change significantly for low oil contents and the effect of the oil only becomes visible above 5 %.

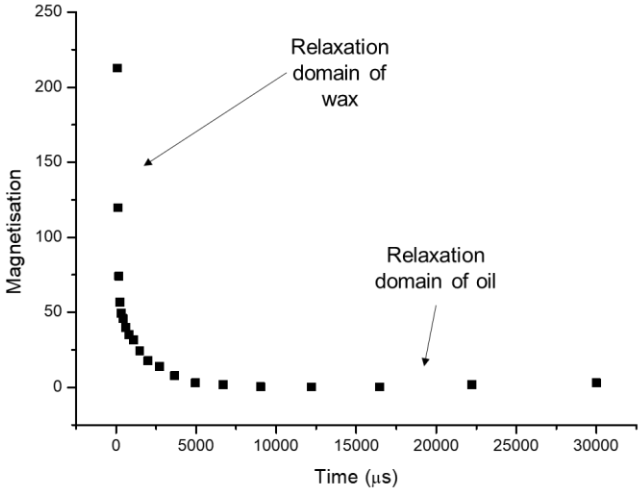

Figure 5. 9 Diagram illustrating the early and later stages of the relaxation profile of a typical sample

A ratio was then taken of the area under the spectrum at an early stage in the decay and a later stage in the decay, as these times represent the magnetisation of the wax at the early stages of the array and the oil remaining at the later stages of the array respectively (Figure 5. 9). This ratio was compared to the predicted oil contents, including the inherent oil of the wax. As can be seen from Figure 5. 13 no obvious trends were observable. Some correlation was expected between magnetisation and oil content which would aid in the production of a calibration curve, however, the response was too erratic. The increase in the relative amorphous content from hard wax to high melting wax irrespective of similarity in melt enthalpy, means that a greater range of values is to be expected due to the presence of both molecular and morphological variety. The mobility of the trapped oil and the mobility of the free oil create opposing effects in the higher melting wax, which contains both states of oil.

Tables S51 and S52 in the supplementary information also provides insight into the relaxation of the rigid domains. The values of the relaxation times of the rigid and mobile domains being of similar orders of magnitude for the medium wax suggests that the mobilities are similar and essentially coalesces into one domain as seen by the NMR experiment. The higher melting waxes display greater differences between the relaxation times of their mobile and rigid components, however, this difference decreases with increasing oil content as the disruption in crystallinity is enhanced. Since the direct use of T_2 relaxation was ineffective this led us to alternative approaches in data processing in an endeavour to optimise the results of the T_2 experiment.

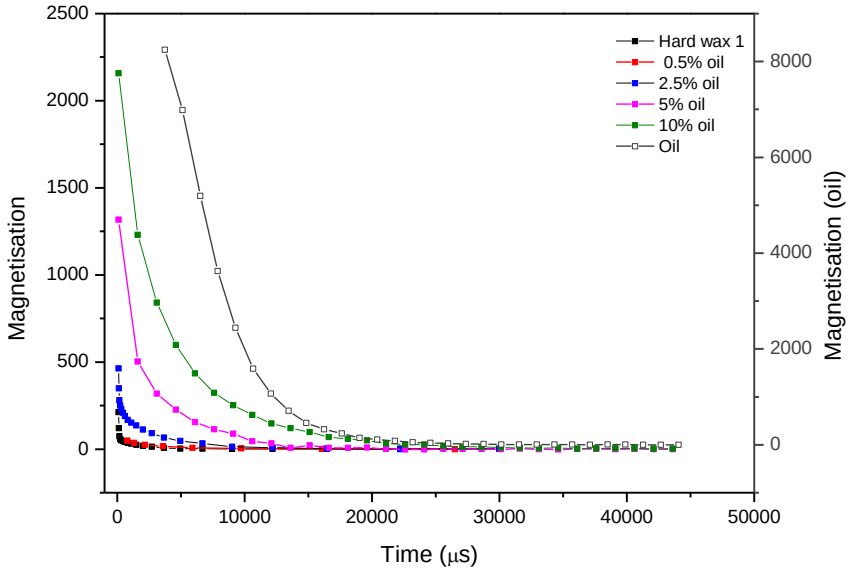

Figure 5. 10: T_2 relaxation curves of hard wax standards

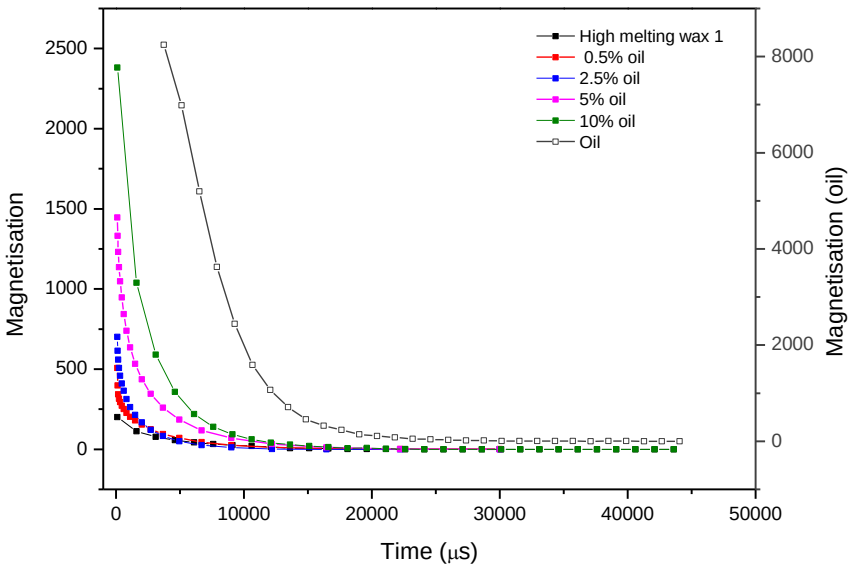

Figure 5. 11: T_2 relaxation curves of high melting wax standards

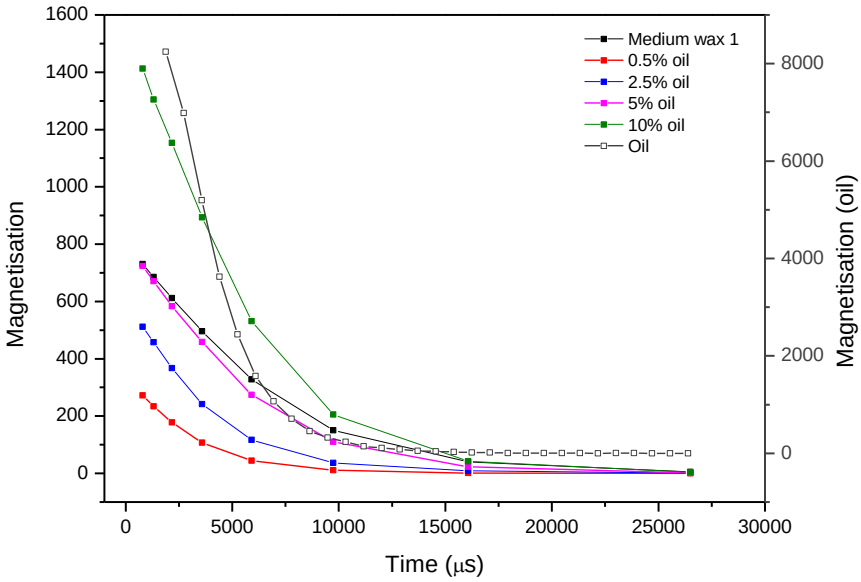

Figure 5. 12: T_2 relaxation curves of medium melting wax standards

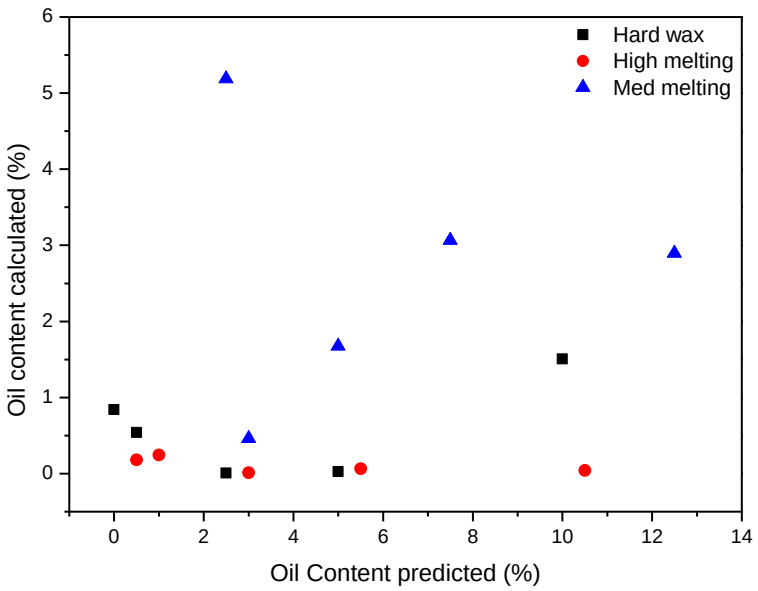

Figure 5. 13: Calibration curves of area under the T_2 relaxation curves

Kané et al. proposed a correction to the bias of NMR results for determination of the solid content of crude oils[18]. They make use of a method commonly applied in the agricultural and food industries to perform quality control on seed oils called the solid-fat index. By using a similar concept as applied above for T_2 measurements they defined the solid content (SC)

using Equation 5.1 where M_s and M_l refer to the magnetisation of the solid (short relaxation time) and liquid (long relaxation time) components respectively.

$$SC = \frac{M_s}{M_s + M_l} \quad \text{Eq 5.1}$$

Kané and colleagues found that NMR spectroscopic methods, which are based on proton density, could not be directly compared with other methods based on mass density, such as DSC and the ASTM D-721 method. Equation 5.1 was then adjusted using the densities of the individual solid phases and liquid phases to yield Equation 5.2. In Equation 5.2 d_s and d_l refer to the mass density (mass per unit volume) of the solid and liquid phases, ρ_s and ρ_l refer to the proton density (number of protons per unit volume) of the solid and liquid phases and m_s and m_l refer to the mass of the solid and liquid phases respectively.

$$SC = \frac{(\rho_s/d_s)m_s}{(\rho_s/d_s)m_s + (\rho_l/d_l)m_l} \quad \text{Eq 5.2}$$

Equation 5.2 was applied to the oil/wax standards using experimentally determined densities by calculating the oil content as *1 – SC*. The oil contents in Table 5. 3 are significantly lower than those calculated by Wideline deconvolution. Only at the highest oil contents are values greater than zero obtained. This, once again, shows the tendency of FT waxes to trap oil between crystallites. The use of solid-state NMR spectroscopy to distinguish between wax and oil is based on mobility differences. Therefore the lower apparent oil content implies that within the wax matrix the oil has become more rigid. For this to occur at such high oil content values suggests that the oil is well dispersed within the wax matrix. As illustrated in Figure 5. 14a, large pools of oil which are phase-separated from the matrix contains a transitional layer where mobility gradually increases from the outer edge which is surrounded by crystalline wax to the centre of the oil domain. When the oil is dispersed, as in Figure 5. 14b, very little oil remains after the gradual decrease from the crystalline boundary. This could explain why the oil content calculated according to NMR spectroscopy showed less oil present in the FT waxes than was known to be present. This model is validated by similar theories proposed by Le Roux and Loubser[24] for FT waxes. The theory of dispersion within the wax matrix is only valid assuming an affinity between the wax and the oil enabled by the composition of the oil.

Table 5. 3: Solid and oil contents determined by Equation 5.2

Oil content$_{prepared}$ (%)	Hard wax		High melting wax		Medium melting wax	
	Solid content (%)	Oil content (%)	Solid content (%)	Oil content (%)	Solid content (%)	Oil content (%)
0.0	100.0	0.0	100.0	0.0	100.0	0.0
2.5	100.0	0.0	100.0	0.0	100.0	0.0
5.0	100.0	0.0	100.0	0.0	99.9	0.1
10.0	99.8	0.2	100.0	0.0	99.7	0.3

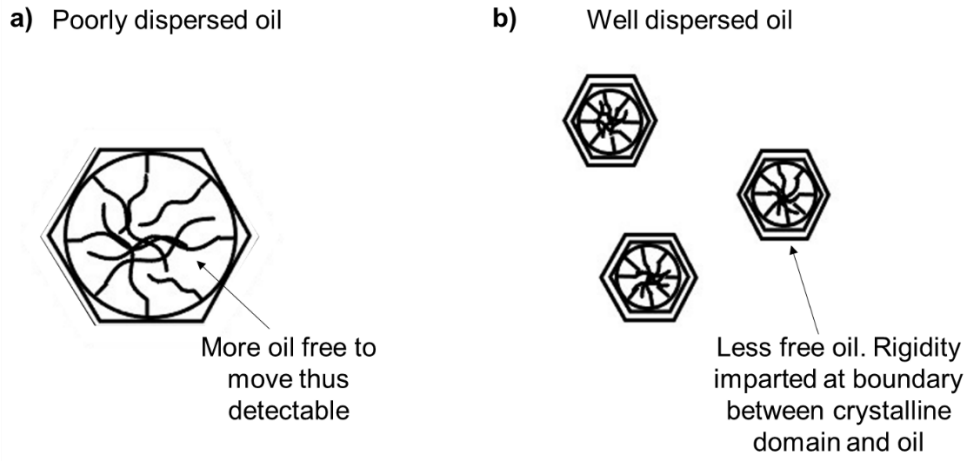

Figure 5. 14: Illustration of the origins of mobility differences of poorly dispersed oil pools after slower crystallisation (a) in contrast to well dispersed oil (b) after rapid crystallisation. Dispersion is facilitated by rapid stirring during preparation. Slower crystallisation allows movement of oil to form oil pools once stirring has ceased.

5.3.2.3 Variable Temperature Approach

The Wideline experiment showed that the oil contains both mobile and more rigid components therefore the true oil signal has a temperature dependency. This means that the oil was sufficiently complex to contain some crystalline material at lower temperatures. In order to determine the true oil content T_2 experiments were also performed at decreasing temperature increments from the melt to -32 °C, which is the recommended analysis temperature for ASTM D-721. The premise behind this approach is that at low temperatures the relaxation of the rigid domains will be so rapid that only the mobile component will be observable by the experiment.

The temperature would then be gradually lowered until the T_2 exponential decay can only be fitted by a single component – the oil.

The variable temperature relaxation curves of the hard wax in Figure S51 (supplementary information) shows that as oil content increases the effect of the oil on the T_2 relaxation of the wax below the crystallisation temperature also increases. The rigidity of the wax and the low quantity of added oil allows the wax to dominate the relaxation, however above 5% oil the domination of the wax decreases. As the oil content increases the change in slope of the relaxation curve suggests the detection of two components – both wax and oil. It is clear that below 90 °C the majority of the wax has crystallised at oil content of 5 % and below. The remaining component still mobile between 0 °C and -32 °C is therefore the true oil. Additionally, the T_2 relaxation times of the mobile component in the hard wax standards in Figure 5. 15 show a three-step relaxation with temperature, also implying initial relaxation of the rigid domains, the interfacial region and the oil respectively. The interaction between the wax and oil remained visible in the high melting wax when observing the earlier decrease in wax dominated relaxation at 50 °C (Figure S52 and Figure 5. 15) but did not follow the same gradual trend with increasing oil content as the hard wax. It appeared that even at high oil contents the oil remained trapped within wax matrix and relaxed rapidly with the wax. This is likely due to greater affinity between the oil and the high melting wax which contains more amorphous regions than the hard wax.

Figure 5. 15 and Figure S53 display the variable temperature relaxation of the medium melting wax which follows a similar trend to that of the high melting wax. The majority of the wax has crystallised by 30 °C and a considerable mobile component remains below 30 °C. This is due to the presence of approximately 2.5 % oil before the addition of the standard oil which causes the medium melting wax to display different trends to the hard wax and high melting wax.

A similar approach to the T_2 method was applied by determining the ratio of the areas under the spectra. In this case the area of the total sample was taken as the maximum signal in the molten state and a correlation was determined using the maximum signal at various temperatures which displayed an order of magnitude difference in mobility as measured by T_2. The results in Figure 5. 16 proved the most promising for the formulation of a calibration curve. The hard wax and high melting wax display almost linear trends in areas. A correlation line is drawn in the figures to indicate the position of the theoretical 100% correlation as well as a dashed line indicating the optimal temperature for measurement for each of the waxes. For all waxes, this temperature is 30 °C, however, the linear range occurs at lower oil contents for higher melting waxes and at higher oil contents for the medium melting wax. It may appear to simplify the process if the best correlation is obtained at slightly above room temperature

since working at -32 °C was proven to be unnecessary, but it is important to note that each of these samples was heated to above the melt and underwent controlled cooling in order to obtain the result seen in Figure 5. 16. As proposed by the relaxation times in Figure 5. 15, the medium melting wax demonstrates different correlation trends to that of the two higher waxes. A more linear trend was observed at 30 °C, however, this temperature was too close to the melting temperature of 50 °C and would result in constantly changing results due to thermal annealing. In addition, the minimum temperature of -32 °C also yielded a more linear curve, especially for the lower oil contents compared to the other temperatures. This suggested that the interaction between the oil and wax is less for higher melting waxes since a linear trend could be obtained despite the values not correlating exactly. The medium melting wax, which contained greater extent of interaction with the oil, displayed irregular trends. This is expected for some FT waxes which are known to not retain oils as well as microcrystalline waxes but merely freeze them between crystallites,[25] leading to the common phenomenon of oil bleed in FT wax formulations. While this method has the most promise, it is clear that a number of data points at each correlation value would be required to achieve the most accurate trendline before the calibration curve could be used predictively.

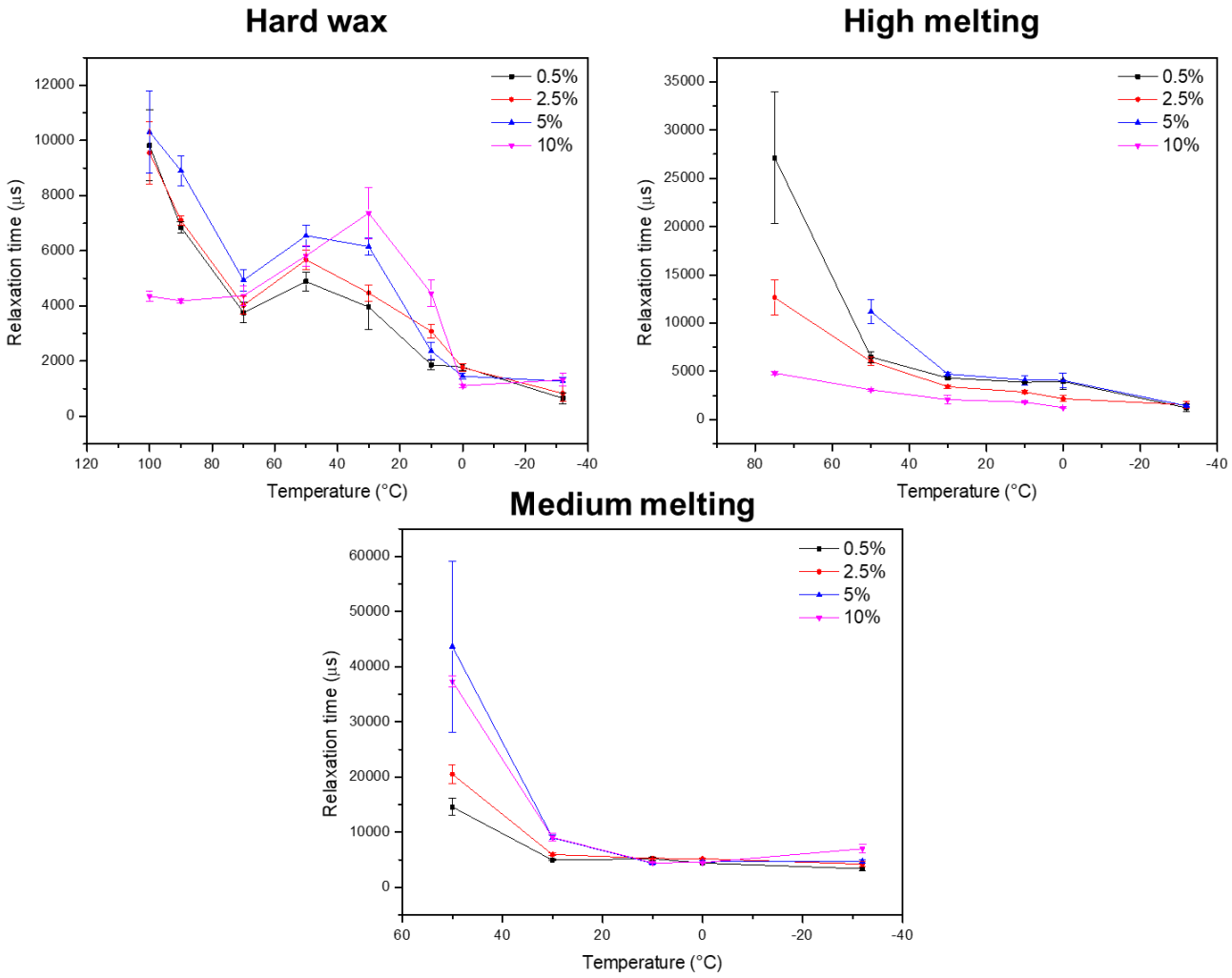

Figure 5. 15: Variable temperature T_2 relaxation of wax standards

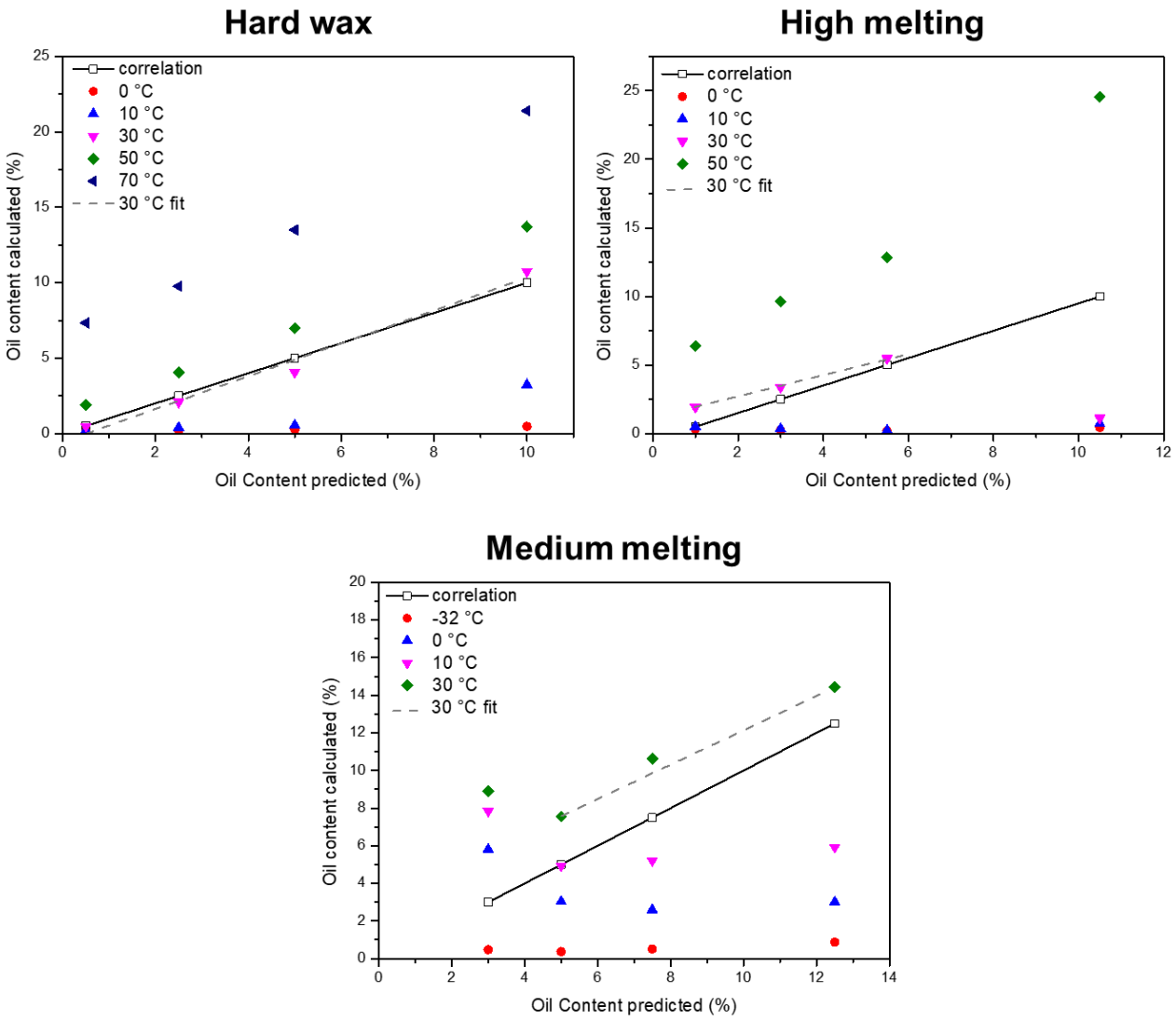

Figure 5. 16: Correlation of predicted and calculated oil content at different temperatures by VT T_2 relaxation areas showing the 100% correlation line as well as the best fit with a linear range for each set of standards

5.3.3 The nature of the oil

It became clear that the behaviour of the oil within the wax matrix was not easily predictable by any of the previously applied approaches. One of the reasons for this, as formerly stated, was the complexity of the oil used. Figure 5. 1 shows that the oil contains a wide carbon number distribution as well as a slightly heavy tail for an oil. This prompted the question whether the oil content of the oil/ wax blends would be simpler to determine using a more homogeneous oil for a fundamental study. The same waxes were blended with heptadecane, the highest alkane which is liquid at room temperature, and re-analysed using the T_2 relaxation approach.

The relaxation curves of the heptadecane/wax standards in Figure 5. 17 show similar trends to the previous standards containing the oil. The hard wax and high melting wax display a gradual decrease in relaxation rate. These standards also confirm that the limit of detection for this method is approximately 0.5 wt%, as these relaxation curves show great similarity to the neat wax curves. The medium melting wax in Figure 5. 17c shows an increase in relaxation rate with the addition of heptadecane, however, the quantity of heptadecane added to the medium melting wax does not seem to dramatically affect the rate of relaxation. These trends are confirmed in Figure 5. 18 which correlates the predicted oil content values with the calculated values using the same area ratio method as for the T_2's above. The trends appear much more linear than those of the oil standards for the higher waxes which do not pass through the origin, proving that a more accurate calibration curve can be obtained provided the oil is homogeneous. A homogeneous oil effectively acts as a diluent and the quantity of oil added directly correlates to increased "solvation" and mobility of the wax chains. Therefore signals due to oil and wax become easy to separate when the compositional differences are so vast that no interaction exists between the wax and the oil molecules. In reality, this is never the case as it is nearly impossible to find an oil-free wax or conversely, a wax-free oil at all temperatures. Additionally, this method only appeared to be effective for higher melting waxes, as the medium melting wax did not follow the trends in Figure 5. 18. This is most likely due to the aversion of the inherent oil in the medium melting wax to the heptadecane, and generally the oil contents of these waxes range from 0 – 0.5 wt% which is below the limit of detection for the NMR spectroscopic methods discussed.

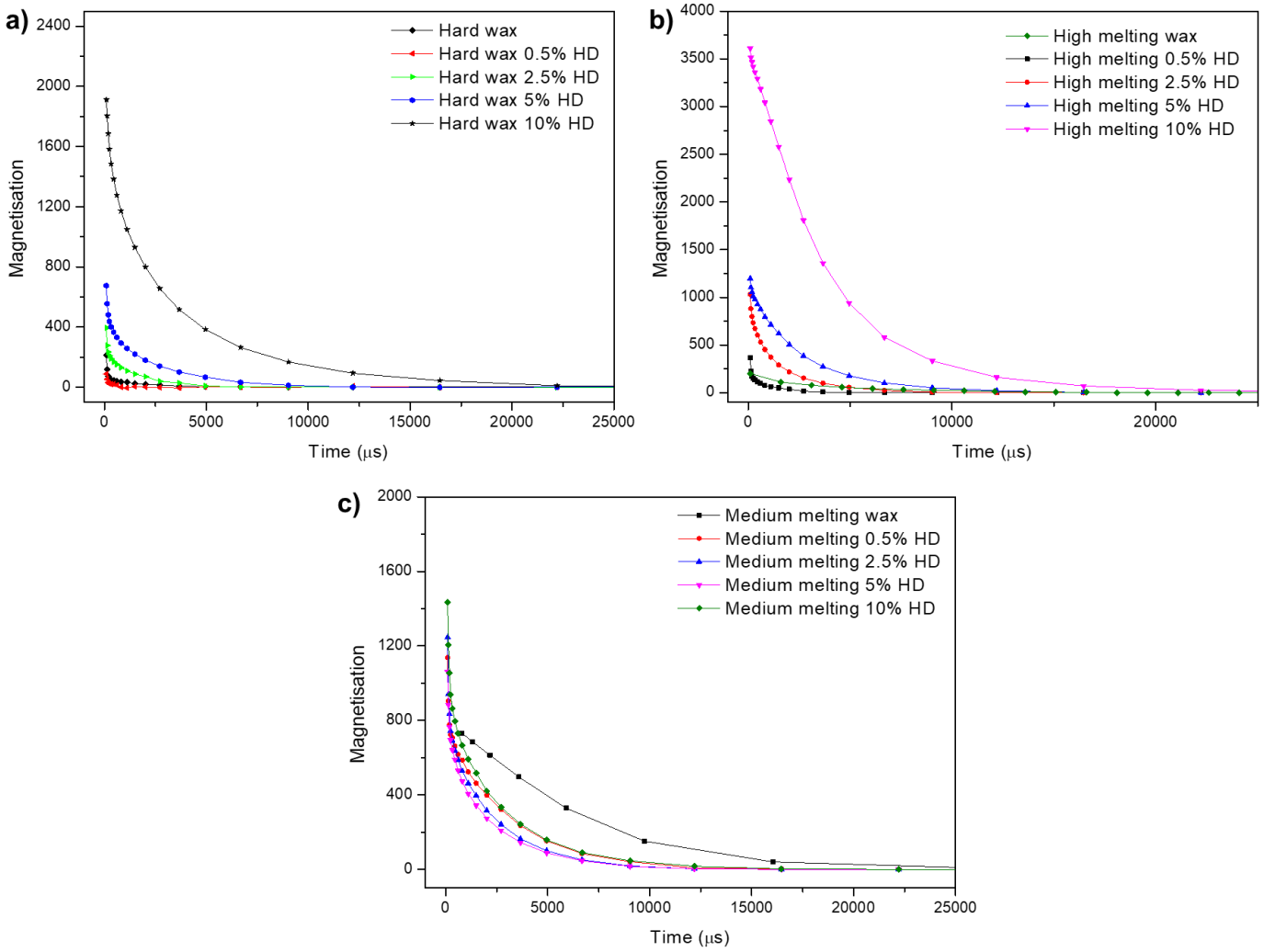

Figure 5. 17: T_2 relaxation curves of a) hard wax/heptadecane standards b) high melting wax/heptadecane standards and c) medium melting wax/heptadecane standards

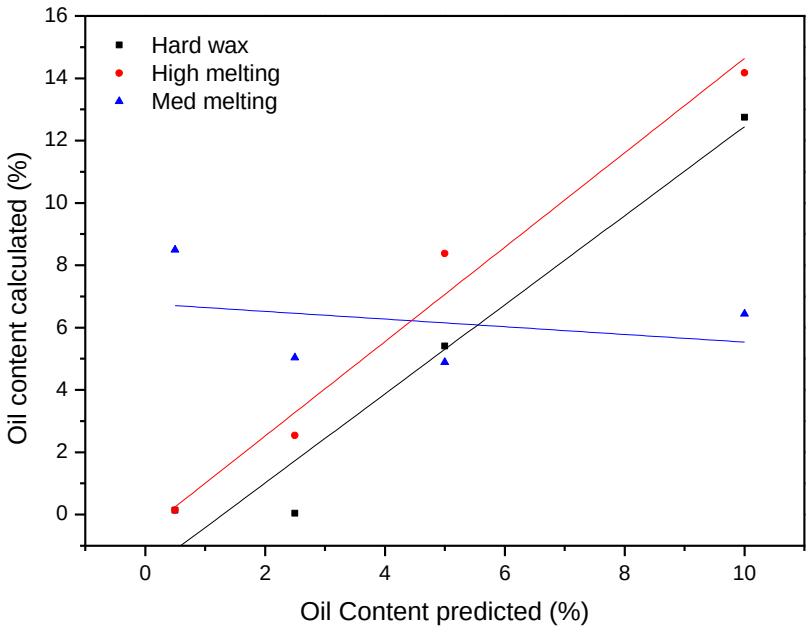

Figure 5. 18: Correlation of predicted and calculated oil content by T_2 relaxation areas of heptadecane/wax standards

5.3.4 Application to paraffin waxes

Until this point all standards have been prepared using FT waxes as a matrix. These waxes were considered ideal for fundamental studies as they are generally cleaner and more crystalline, providing the required variance in carbon number between wax and oil. Since the methods used above have been shown to be ineffective for oil content determination of FT waxes and considering that these methods were originally developed for paraffin waxes,[24] it was necessary to test the same method on paraffin wax standards. Heptadecane standards were prepared using a paraffin wax of low oil content. The 0.5 wt% standard was not prepared since this blend previously showed no significant difference to that of the neat wax and instead a 7 wt% was added. Figure 5. 19 displays the DSC thermograms of these blends. The paraffin wax also showed a similar disruption of wax crystallinity as the FT waxes which can once again be attributed to diluent effects of the heptadecane. The 7 wt% appeared to increase in crystallinity despite the other blends displaying a gradual decrease in crystallinity relative to the paraffin wax. This concentration is also the point where individual thermal events due to the heptadecane can be identified. The 7 wt% seemed to be the new threshold concentration although this does not appear to mean the same thing for FT and paraffin waxes. The FT waxes rapidly decreased in crystallinity after the addition of 2.5 wt% oil or greater and the oil could not be detected below this point, meaning the oil was retained. In contrast, the paraffin

wax immediately displayed significant decreases in crystallinity upon addition of oil with the oil being released at 7 wt%.

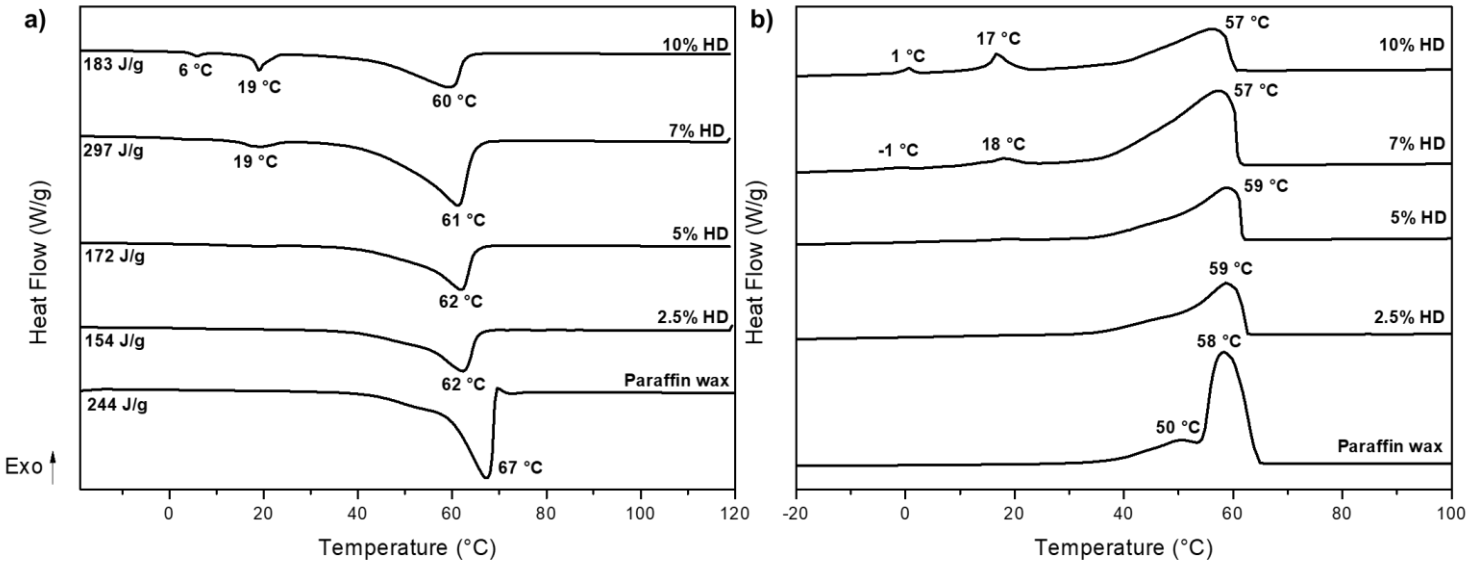

Figure 5. 19: DSC thermograms of a) melting and b) crystallisation of paraffin wax standards

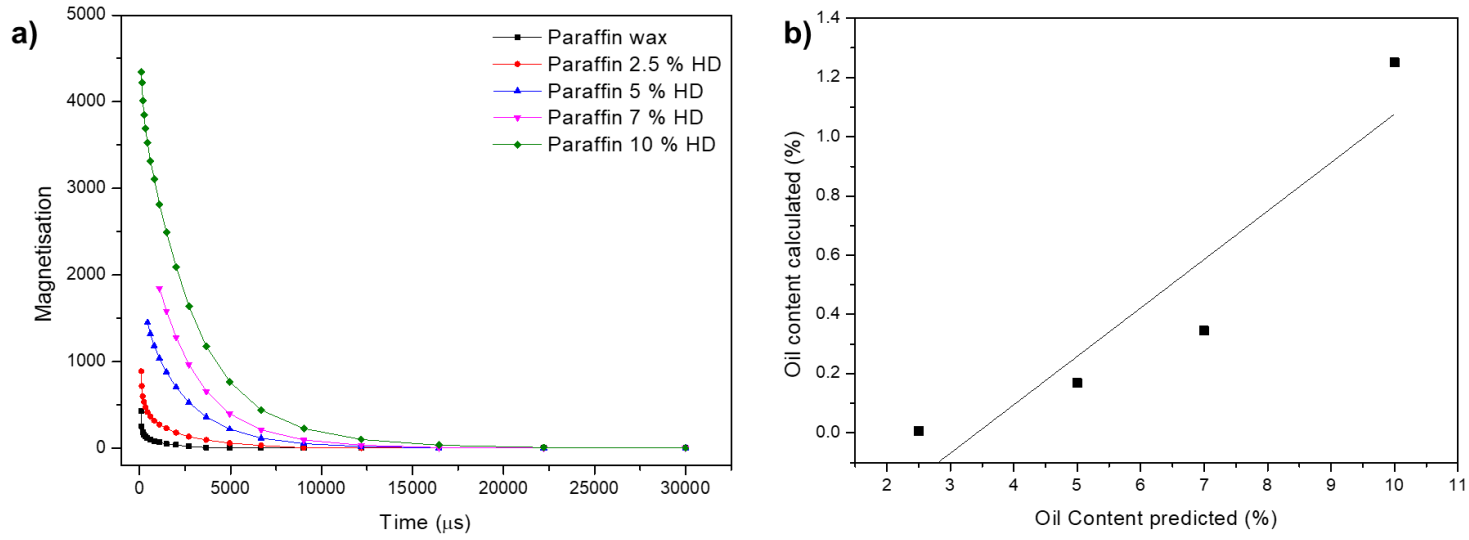

Figure 5. 20: a) T_2 relaxation curves and b) correlation of predicted and calculated oil content of paraffin/heptadecane standards

The T_2 relaxation curves of paraffin/heptadecane standards ca show a gradual decrease in relaxation rate with increasing heptadecane content. The correlation between the calculated and predicted oil contents appeared more linear in this case (Figure 5. 20b), with a change in the gradient occurring after 7% oil. This was in agreement with the threshold oil content of

7 wt% observed by DSC. The linear increase in heptadecane content appeared to be a similar trend to the effect of heptadecane on FT where the heptadecane acted as a solvent to cause increased chain mobility. While this proves that it is possible to obtain almost linear trends using a homogeneous oil, this cannot be directly related to an oil content calibration curve as the real samples would exhibit some kind of interaction between wax and oil which would prevent it from following this trend.

The difference in the way the FT waxes and the paraffin wax hold oil was confirmed by the CLSM images in Figure 5. 21 and Figure 5. 22. The FT waxes are comprised of a considerably more dense structure which forms rapidly upon cooling. This rapid crystallisation would trap the oil in the interstitial spaces between crystalline domains to form a scenario shown in the diagram Figure 5. 14b. The paraffin wax contains significantly greater amorphous content due to increased branching of the wax. The paraffin wax would still crystallise rapidly due to its short-chain nature, but comparatively slower than the FT waxes since smaller crystallites with more defects do not stack as effectively. The slower crystallisation rate and the inherent mobility of the paraffin wax[26] would disperse the oil in the amorphous areas between crystals.[4] The complexity of the nature of the relationship between oil and wax, governed by both relaxation and diffusion processes[27] make the accurate determination of oil contents by NMR spectroscopy a challenging experiment.

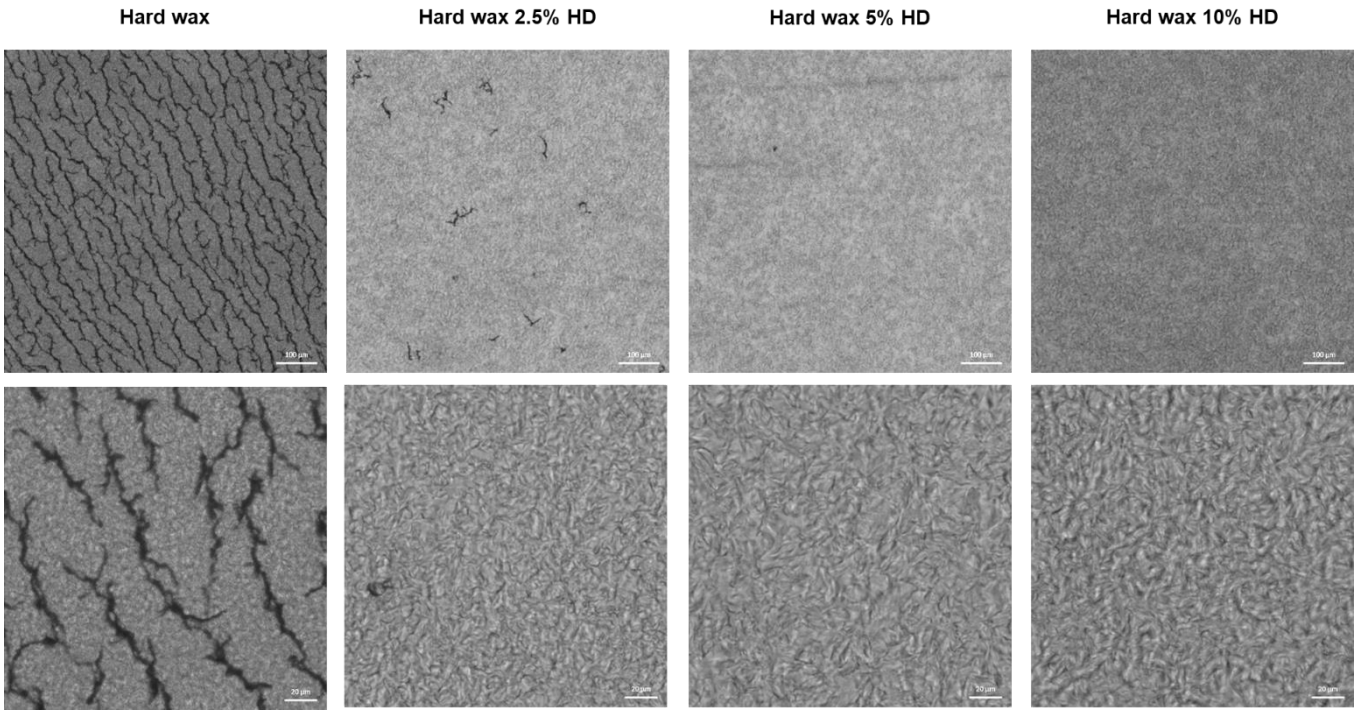

Figure 5. 21: CLSM images of hard wax/heptadecane standards

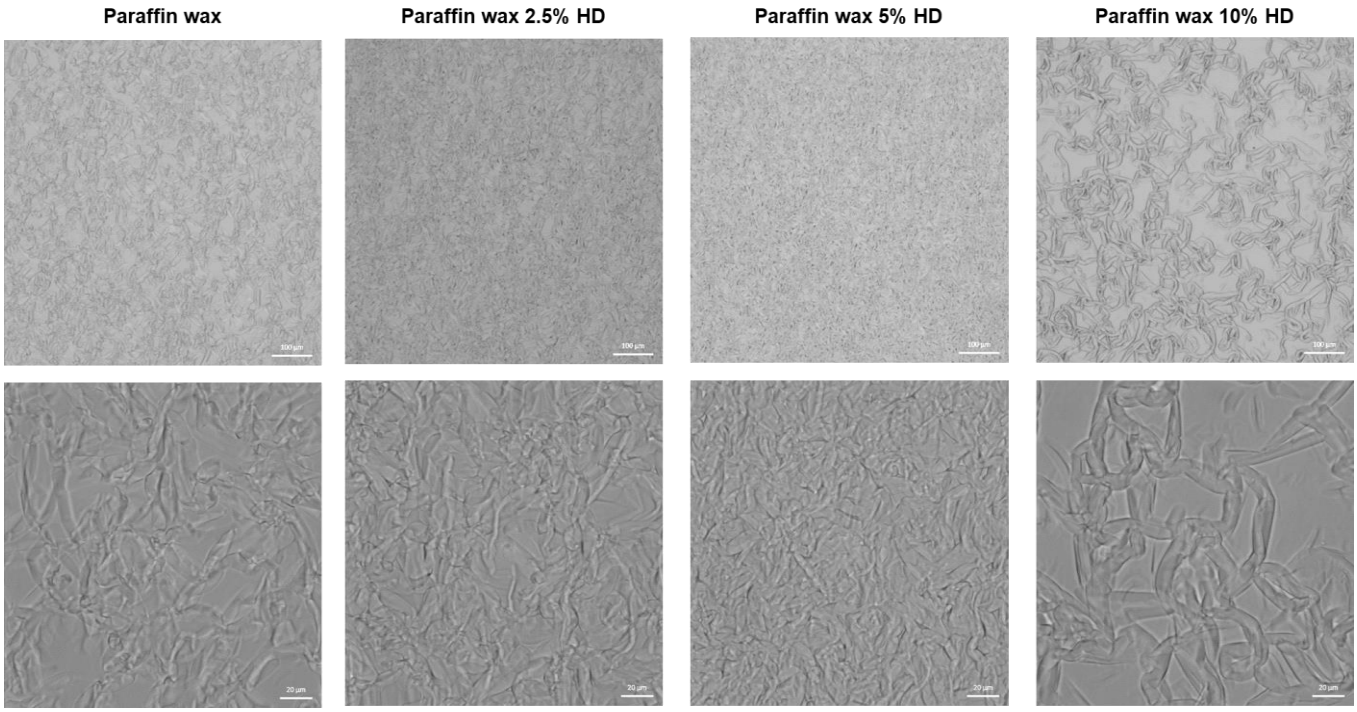

Figure 5. 22: CLSM images of paraffin wax/heptadecane standards

5.4 Conclusion

The results of this research show that FT waxes retain oil in different ways depending on the crystallinity and carbon number distribution of the wax. More crystalline waxes with low inherent oil contents form cracks between rigid domains. The oil pools in these cracks and is loosely bound due to low levels of molecular interactions. Less crystalline FT waxes were proven to have greater extents of interaction with the oil. The wax attempted to accommodate the oil within its crystalline domains as the oil and original wax were indistinguishable from each other, resulting in an overall disruption in crystallinity at lower oil contents until the saturation point of the wax was reached.

A variety of NMR spectroscopy analysis approaches and data processing methods were used in an attempt to correlate oil content as determined by ASTM D-721 with signals obtained by NMR spectroscopy. A simple deconvolution and comparison of Wideline areas in higher melting waxes showed that oil could not be detected below 2.5 wt%. The rigidity of the surrounding wax matrix appeared to limit the mobility of the oil at the interfaces, leading to an underestimation of oil content. The use of T_2 relaxation experiments proved insufficient as no clear relationship between the area under the relaxation spectra and oil content was observed. The correction method for the discrepancies occurring due to differences between mass densities and proton densities yielded by NMR spectroscopy was also applied. This method also underestimated the oil content and was not effective. Isolation of the true oil by controlled heating and recrystallisation provided further clarity on the nature of the interaction between

the wax and the oil. A calibration curve produced by this method displayed almost linear trends at 30 °C with varying optimal oil contents yielding linear ranges but was still inadequate for accurate oil content determinations as the linear fit did not pass through the origin of the calibration curve. Simplifying the composition of the oil to heptadecane for a model study proved more effective at first. The calibration curve produced by this method showed almost linear correlations between predicted oil content and calculated oil content, however, this was more likely due to solvation effects by the homogeneous oil and in reality oils can be highly complex. While the method works fundamentally, the actual application yields inaccurate results since there will always be some degree of interaction between the wax and the oil. More extensive calibration would be required to make this method effective, with multiple data points needed at each oil content value. Due to the observation of changes in behaviour beyond certain threshold oil contents it is likely that separate calibration curves are required for low and high oil contents of similar wax types.

The application to paraffin waxes verified the results of the FT counterparts. The heptadecane yielded linear correlations but again only due to enhanced mobility due to diluent effects. Comparison between FT and paraffin blends showed that NMR spectroscopy and ASTM have similar minima for oil signal observation. Additionally, the mechanism of oil retention differs due to differences in crystallisation rate and the nature of the spaces between crystalline domains as a result of molecular and morphological variations between linear and branched waxes. This difference in the manner in which the oil is dispersed, affects whether the oil can be detected by NMR experiments as an isolated signal, as oil dispersed in amorphous regions have similar mobilities to wax components as opposed to oil trapped in the voids between stacked crystals. This study has proved that linear correlations between NMR signals and oil contents in waxes cannot be consistently reproduced or expected even where melting behaviour appears linear. The combination of two distributions of molecules and their extent of overlap produces a new material which does not simply behave as a summation of properties of the individual components. Extensive calibration of each data point in the calibration curve is necessary for every sample as interactions between the wax and the oil may vary depending on the composition and morphology of both components.

References

[1] I. Basson, E.C. Reynhardt, The structure and melting of paraffinic Fischer-Tropsch waxes, Chem. Phys. Lett. 198 (1992) 367–372. https://doi.org/10.1016/0009-2614(92)85066-J.

[2] R.J. Speight, J.P. Rourke, A. Wong, N.S. Barrow, P.R. Ellis, P.T. Bishop, M.E. Smith, 1H and 13C solution-and solid-state NMR investigation into wax products from the Fischer-Tropsch process, Solid State Nucl. Magn. Reson. 39 (2011) 58–64.

https://doi.org/10.1016/j.ssnmr.2011.03.008.

[3] M. Bekker, N.R. Louw, V.J. Jansen Van Rensburg, J. Potgieter, The benefits of Fischer-Tropsch waxes in synthetic petroleum jelly, Int. J. Cosmet. Sci. 35 (2013) 99–104. https://doi.org/10.1111/ics.12011.

[4] M.I. Zougari, T. Sopkow, Introduction to crude oil wax crystallization kinetics: Process modeling, Ind. Eng. Chem. Res. 46 (2007) 1360–1368. https://doi.org/10.1021/ie061002g.

[5] E.K. Park, K.W. Song, Rheological evaluation of petroleum jelly as a base material in ointment and cream formulations: Steady shear flow behavior, Arch. Pharm. Res. 33 (2010) 141–150. https://doi.org/10.1007/s12272-010-2236-4.

[6] A. Drews, Standard test method for oil content of petroleum waxes, Man. Hydrocarb. Anal. 6th Ed. 69 (2008) 166-166–6. https://doi.org/10.1520/mnl10849m.

[7] M. Mafi, F. Yazdani, F. Farhadi, Determine oil content in petroleum waxes, Hydrocarb. Process. 85 (2006) 95–97.

[8] A.W. MacGregor, L.A. O'Dell, R.W. Schurko, New methods for the acquisition of ultra-wideline solid-state NMR spectra of spin-1/2 nuclides, J. Magn. Reson. 208 (2011) 103–113. https://doi.org/10.1016/j.jmr.2010.10.011.

[9] K.R. Schmidt-Rohr, J. Clause, H.W. Spiess, Correlation of structure, mobility, and morphological information in heterogeneous polymer materials by two-dimensional Wideline-Separation NMR spectroscopy, Macromolecules. 25 (1992) 3273–3277. https://doi.org/10.1021/ma00038a037.

[10] L.A. Colnago, M. Engelsberg, A.A. Souza, L.L. Barbosa, High-throughput, non-destructive determination of oil content in intact seeds by continuous wave-free precession NMR, Anal. Chem. 79 (2007) 1271–1274. https://doi.org/10.1021/ac062091+.

[11] D.E. Alexander, L.S. S., F.I. Collins, R.C. Rodgers, Analysis of oil content of maize by wide-line NMR, J. Am. Oil Chem. Soc. 44 (1967) 555–558. https://doi.org/10.1007/BF02901248.

[12] N. Marigheto, S. Duarte, B.P. Hills, NMR relaxation study of avocado quality, Appl. Magn. Reson. 29 (2005) 687–701. https://doi.org/10.1007/BF03166344.

[13] H. Saxena, A. Majhi, B. Behera, Prediction of wax content in crude oil and petroleum fraction by proton NMR, Pet. Sci. Technol. 37 (2018) 226–233. https://doi.org/10.1080/10916466.2018.1536713.

[14] M.V. Kök, M.A. Varfolomeev, D.K. Nurgaliev, Wax appearance temperature (WAT) determinations of different origin crude oils by differential scanning calorimetry, J. Pet. Sci. Eng. 168 (2018) 542–545. https://doi.org/10.1016/j.petrol.2018.05.045.

[15] L.M. Alghanduri, M.M. Elgarni, J.L. Daridon, J.A.P. Coutinho, Characterization of Libyan waxy crude oils, Energy and Fuels. 24 (2010) 3101–3107. https://doi.org/10.1021/ef1001937.

[16] E.M. Kelechukwu, Prediction of wax deposition risk of Malaysian crude from viscosity-temperature correlation for dead crude, Int. J. Sci. Adv. Technol. 1 (2011) 89–100.

[17] W.B. Pedersen, A.B. Hansen, E. Larsen, A.B. Nielsen, H.P. Rønningsen, Wax precipitation from North Sea crude oils. 2. Solid-phase content as function of temperature determined by pulsed NMR, Energy and Fuels. 5 (1991) 908–913. https://doi.org/10.1021/ef00030a020.

[18] M. Kané, M. Djabourov, J.L. Volle, D.N. Rutledge, Correction of biased time domain NMR estimates of the solid content of partially crystallized systems, Appl. Magn. Reson. 22 (2002) 335–346. https://doi.org/10.1007/BF03166115.

[19] R. Lee, V.A. Kalichevsky, Determining oil content of paraffin waxes, Ind. Eng. Chem. - Anal. Ed. 14 (1942) 767–769. https://doi.org/10.1021/i560110a001.

[20] S. Kumar, K.M. Agrawal, The deep deoiling of microcrystalline waxes by solvent percolation, Pet. Sci. Technol. 32 (2014) 261–266. https://doi.org/10.1080/10916466.2011.574175.

[21] R.G. Alamo, J.A. Blanco, I. Carrilero, R. Fu, Measurement of the 13C spin-lattice relaxation time of the non-crystalline regions of semicrystalline polymers by a cp MAS-based method, Polymer (Guildf). 43 (2002) 1857–1865. https://doi.org/10.1016/S0032-3861(01)00761-3.

[22] M. Pollard, K. Klimke, R. Graf, H.W. Spiess, M. Wilhelm, O. Sperber, C. Piel, W. Kaminsky, Observation of chain branching in polyethylene in the solid state and melt via 13 C NMR spectroscopy and melt NMR relaxation time measurements, Macromolecules. 37 (2004) 813–825. https://doi.org/10.1021/ma0349130.

[23] J. Clauss, K. Schmidt-Rohr, H.W. Spiess, Determination of domain sizes in heterogeneous polymers by solid-state NMR, Acta Polym. 44 (1993) 1–17. https://doi.org/10.1002/actp.1993.010440101.

[24] J.H. Le Roux, N.H. Loubser, Nuclear Magnetic-Resonance investigation of the mobile phase in paraffinic Fischer-Tropsch waxes, S. Afr. J. Sci. 76 (1980) 157–161.

[25] A. Blake, The microstructure and physical properties of plant-based waxes and their relationship to the oil binding capacity of wax oleogels, University of Guelph, 2015.

[26] A. Palou, J. Cruz, M. Blanco, R. Larraz, J. Frontela, C.M. Bengoechea, J.M. González, M. Alcalà, Characterization of the composition of paraffin waxes on industrial applications, Energy and Fuels. 28 (2014) 956–963. https://doi.org/10.1021/ef4021813.

[27] G.J. Hirasaki, S.W. Lo, Y. Zhang, NMR properties of petroleum reservoir fluids, Magn. Reson. Imaging. 21 (2003) 269–277. https://doi.org/10.1016/S0730-725X(03)00135-8.

Chapter 5

Supplementary Information

Relaxation Approach

Table S5 1 T_2 relaxation times for mobile and rigid components of wax standards by conventional two component exponential decay

Oil content (%)	T_2 relaxation time (µs)					
	Hard wax		High melting wax		Medium melting wax	
	Mobile	Rigid	Mobile	Rigid	Mobile	Rigid*
0.5	3956	730	2878	60	2984	-
2.5	3282	94	1913	140	3632	-
5.0	4198	556	2947	298	5477	-
10.0	5495	1226	3301	824	5460	-

*Two component fit did not converge

Table S5 2 T_2 relaxation times for mobile and rigid components of wax standards by linear combination of two component exponential decay

Oil content (%)	T_2 relaxation time (µs)					
	Hard wax		High melting wax		Medium melting wax	
	Mobile	Rigid	Mobile	Rigid	Mobile	Rigid
0.5	2923	2255	3503	126	3404	3088
2.5	3018	90	3094	323	3883	3834
5.0	3362	2534	4757	532	6050	5313
10.0	5033	3856	7219	1350	5895	5391

Variable Temperature Approach

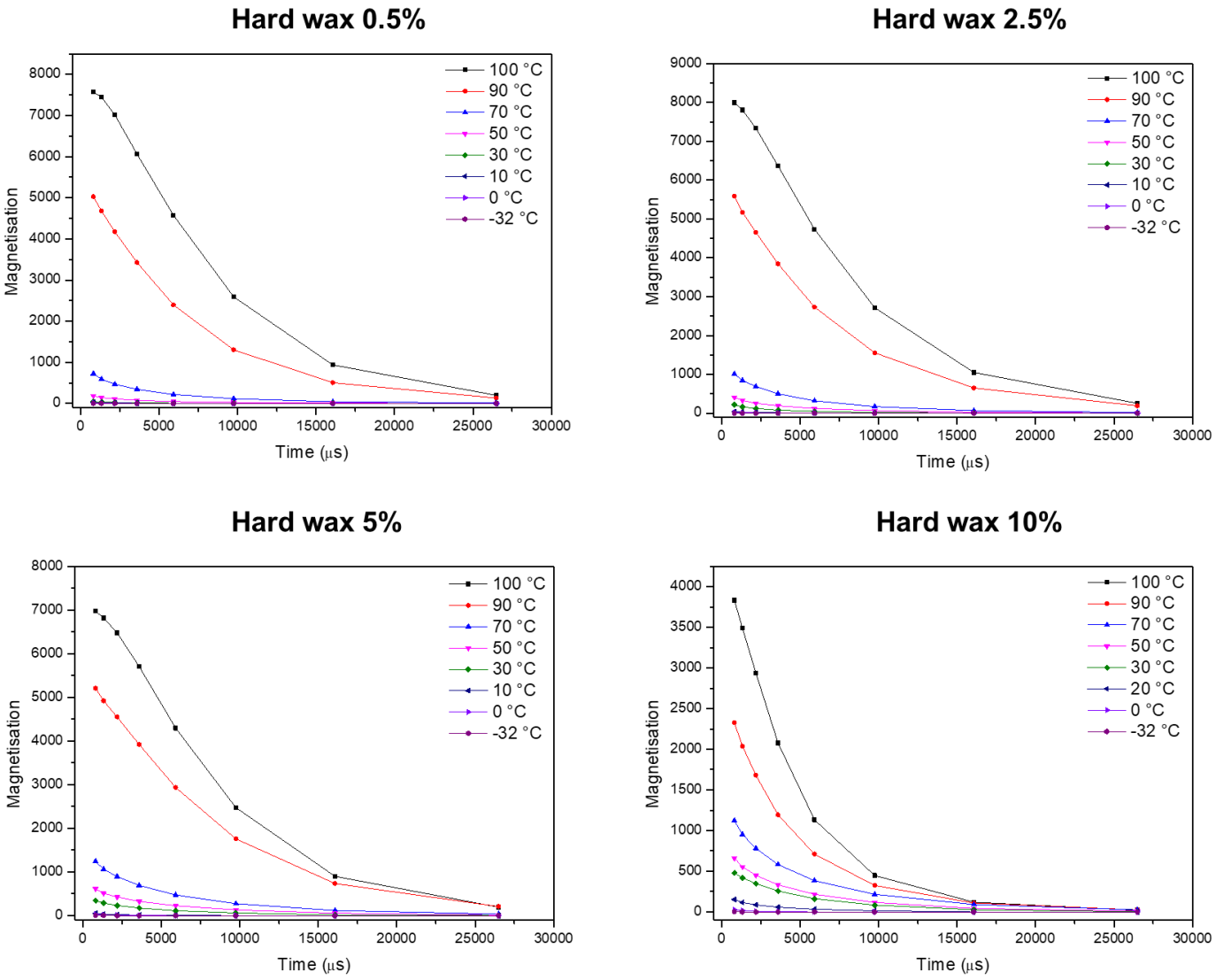

Figure S5 1: Variable temperature T_2 relaxation of hard wax standards

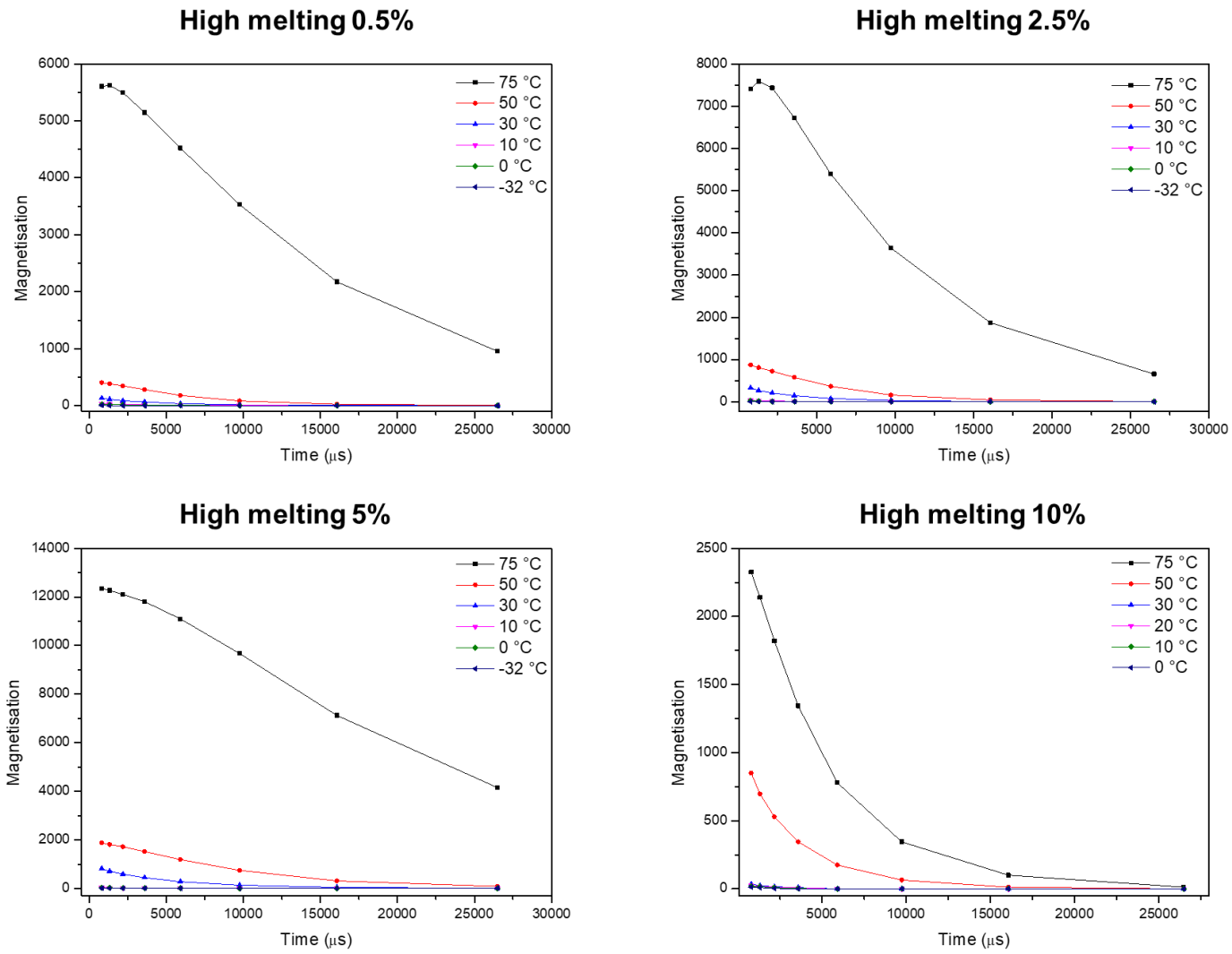

Figure S5 2 Variable temperature T_2 relaxation of high melting wax standards

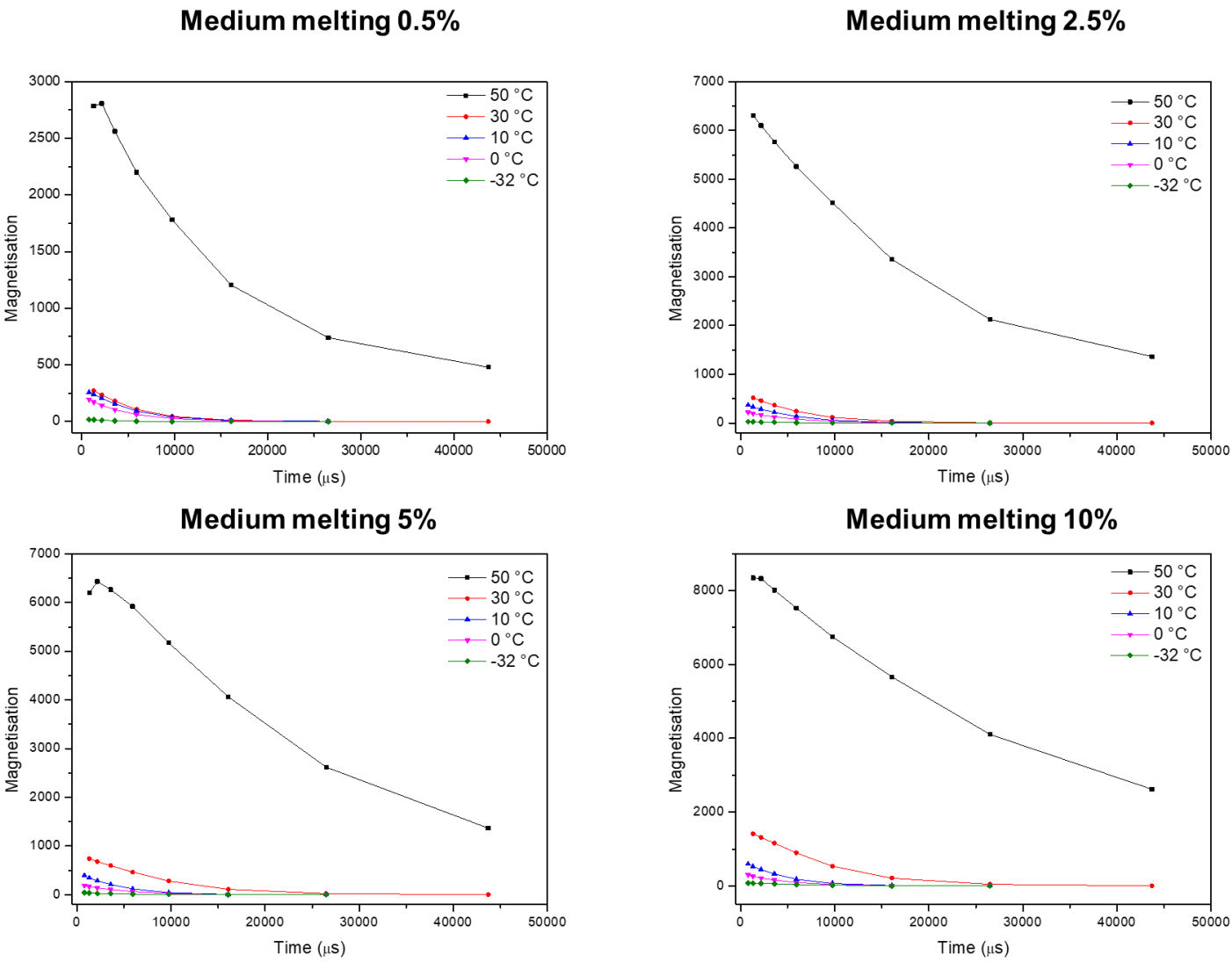

Figure S5 3 Variable temperature T_2 relaxation of medium melting wax standards

Chapter 6
Summary

This thesis is divided into three main chapters each detailing a different problem which was solved by solid-state NMR spectroscopy and other solid-state analytical methods.

Chapter three focused on the development of an *in-situ* vis-breaking method to study the changes taking place in a heterophasic ethylene-propylene copolymer under the influence of peroxide treatment. Both solution ^{13}C NMR and solid-state NMR spectroscopy were used to determine the effect of the peroxide on the structure and morphology of the HEPCs. In the study the copolymers used contained increasing quantities of ethylene and were compared to pure isotactic polypropylene. The vis-breaking of HEPCs was found to be influenced by the homogeneity of the chain sequences. The *in-situ* vis-breaking method revealed significant changes in the mobility of the crystalline domains. The formation of a disordered crystal phase within the α structure was also observed after peroxide treatment. Both solution and solid-state NMR experiments confirmed the enhanced sensitivity of copolymers containing short ethylene sequences to degradation due to the peroxide. It was suggested that longer chain ethylene sequences had a greater capacity to resist chemical changes and could provide a certain degree of protection from degradation due to of the low reactivity of the ethylene units.

Chapter four discusses the feasibility of using high ethylene-content impact polypropylene copolymers as the polymer component in a hot-melt adhesive formulation. An impact copolymer containing 12% ethylene was blended with three waxes: a linear paraffin, a branched paraffin and a FT wax and these blends were characterised by DSC, XRD and solid-state NMR spectroscopy. The complexity of the composition of the impact copolymer leads to a range of complex interactions with the various types of waxes. Overall the trend was that the ethylene-rich regions on the copolymer have strong interactions with the wax and that the extent of this interaction depends on the type of wax. The adhesive bond strength results of the HMAs formulated with these blends was found to be comparable to that of an industry standard HMA but the failure mechanism was dependent on the wax type and concentration. The mechanism of failure could be directly related to the compatibility of the components within the HMA. Lower wax contents lead to tougher HMAs while higher wax concentrations slightly decreased the toughness due to lower compatibility. Crystallisation kinetics revealed that the HMAs with low wax concentrations have long open times compared to the HMA without wax and that increasing the wax concentration further increases the open time.

In chapter five the complex relationship between a wax and its oil component is investigated. In the past, the quantification of oil content by solid-state NMR spectroscopy has been

promoted as a beneficial technique due to the rapid results and solvent-free nature of the tests, however, some users have reported discrepancies between the NMR result and that obtained by the standard ASTM D-721 method. This chapter details the use of various NMR experimental and data processing approaches to attempt to predict oil contents in FT waxes. NMR spectroscopy was found to underestimate the value of the oil content in FT waxes due to the ability of the wax to trap small domains of oil within the matrix during rapid crystallisation. Perfect linear correlations between calculated and predicted oil contents could not be obtained, even after applying corrections due to disparities between mass density and proton density. Near linear calibration curves could be obtained by isolating a true oil signal at 0/-32 °C during variable temperature solid-state NMR experiments. The use of heptadecane in a model study as a simpler oil analogue proved that, by removing oil/wax interactions and only using the oil as a diluent, near linear calibration curves could be attained. Insight into the mechanism of oil retention in FT of different crystallinities as well as paraffin waxes was obtained, showing differences due to both molecular and morphological variation. The results in this chapter show that linear calibration curves cannot be expected even when melting behaviour varies linearly due to molecular interactions and that an extensive calibration would be required to apply Wideline NMR spectroscopic methods for oil content analysis in wax applications.